The Dissertation Committee for Ryan Scott Smith Certifies that this is the approved version of the following dissertation:

The Effect of Ultra-violet Light Curing on the Molecular Structure and Fracture Properties of an Ultra Low-k Material

Committee:

Paul S. Ho, Supervisor

Rui Huang

Kenneth Liechti

Llewellyn K. Rabenberg

Eric Taleff

The Effect of Ultra-violet Light Curing on the Molecular Structure and Fracture Properties of an Ultra Low-k Material

by

Ryan Scott Smith, B.A.; M.S.

Dissertation

Presented to the Faculty of the Graduate School of
The University of Texas at Austin
in Partial Fulfillment
of the Requirements
for the Degree of

Doctor of Philosophy

The University of Texas at Austin
August, 2007

Dedication

To my parents

Acknowledgements

I would like to acknowledge my research advisor Prof. Paul S. Ho. Prof. Ho has supported me and my research even when times were difficult and uncertain. I thank him very much.

I would also like to thank Profs. Rui Huang, Kenneth Liechti, Llewellyn Rabenberg, and Eric Taleff for serving on my dissertation committee. I would like to especially thank Prof. Liechti for many useful conversations. Also, I thank Dr. Jay Im for reading my thesis.

I am deeply indebted to Ting Tsui formerly at Texas Instruments and now at IMEC. He prepared all of my samples and provided useful guidance during my research.

No research is done alone. I must acknowledge my colleagues in the Interconnect and Packaging Group. The group has been very generous to me and I would like to thank you all. I must especially thank Junjing Bao, Hualiang Shi, Gary Lu and Junjun Liu for helping me make measurements and many useful discussions. Also, I thank Jo Ann Smith for all her help and kindness.

I want to acknowledge my friends. Meike Hauschildt, Martin Gall, Swarnal Borthakur, Matthias Kraatz, and Soo Young Choi are excellent colleagues and friends. I don't think that I would have enjoyed my years in Austin as much without you. To my good friends, Roger Myers, Vance Ely and Jaffa Kintigh, I am very grateful to have you as my friends.

Finally, I thank my parents for all their encouragement and support.

The Effect of Ultra-violet Light Curing on the Molecular Structure and Fracture Properties of an Ultra Low-k Material

Publication No._____________

Ryan Scott Smith, Ph.D.
The University of Texas at Austin, 2007

Supervisor: Paul S. Ho

As the gate density increases in microelectronic devices, the interconnect delay or RC response also increases and has become the limiting delay to faster devices. In order to decrease the RC time delay, a new metallization scheme has been chosen by the semiconductor industry. Copper has replaced aluminum as the metal lines and new low-k dielectric materials are being developed to replace silicon dioxide. A promising low-k material is porous organosilicate glass or p-OSG. The p-OSG film is a hybrid material where the silicon dioxide backbone is terminated with methyl or hydrogen, reducing the dielectric constant and creating mechanically weak films that are prone to fracture. A few methods of improving the mechanical properties of p-OSG films have been attempted-- exposing the film to hydrogen plasma, electron beam curing, and ultra-violet light curing. Hydrogen plasma and electron-beam curing suffer from a lack of specificity and can cause charging damage to the gates. Therefore, ultra-violet light curing (UV curing) is preferable. The effect of UV curing on an ultra-low-k, k~2.5, p-OSG film is studied in this dissertation. Changes in the molecular structure were measured with Fourier Transform Infrared Spectroscopy and X-ray Photoelectron Spectroscopy. The evolution of the molecular structure with UV curing was correlated with material and fracture properties. The material properties were film shrinkage, densification, and an increase in dielectric constant. From the changes in molecular structure and material properties, a set of condensation reactions with UV light are predicted. The connectivity of the film increases with the condensation reactions and, therefore, the fracture toughness should also increase. The effect of UV curing on the critical and sub-critical fracture toughness was also studied. The critical fracture toughness was measured at four different mode-mixes-- zero, 15°, 32°, and 42°. It was found that the critical fracture toughness increases with UV exposure for all mode mixes. The sub-critical fracture toughness was measured in Mode I and found to be insensitive to UV cure. A simple reaction rate model is used to explain the difference in critical and sub-critical fracture toughness.

Table of Contents

List of Tables

List of Figures

Chapter 1 Introduction

The gate density and operating frequencies of microelectronic chips are increasing. As the gate length shortens, the interconnect wire density also increases, reducing the wire cross-section and distance between lines. The resistance increases due to the decrease in cross-sectional area and the capacitance between wires increases as the inter-line distance shrinks. The product of a larger resistance and capacitance is an increase in the RC time delay for propagating signals, Fig. 1.1. A lower resistivity metal and a lower permittivity dielectric must be substituted for the traditional Al(Cu) interconnects and the silicon dioxide interlayer dielectric. The semiconductor industry has already chosen copper as the new metal; but, new dielectrics are still being investigated. A promising class of low-k and ultra low-k dielectrics is porous organosilicate glass (p-OSG). While p-OSG can be engineered to possess the necessary dielectric constant, the materials are

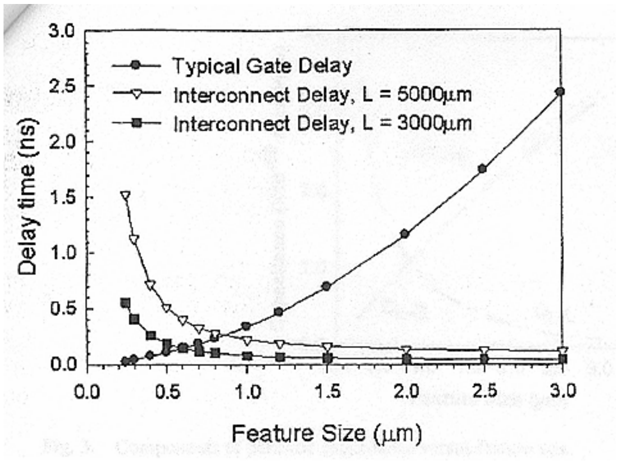

Figure 1.1 Time delay from gates and interconnect structures [1].

weak and prone to fracture in the inter-layer dielectric stack during chemical mechanical polishing (CMP) or during chip packaging. New techniques to improve the mechanical properties of p-OSG are hydrogen plasma treatments, electron beam curing (e-beam), and ultra-violet light (UV) curing. These methods will be discussed further in section 1.3. The effect of UV curing on p-OSG will be investigated in this dissertation including changes in the molecular structure, the dielectric constant, and the fracture properties.

Chapter one will discuss the RC time delay, causes of fracture in the low-k films and low-k interfaces, objectives and a literature survey of UV curing of low-k dielectrics, and an overview of the dissertation.

1.1 The RC time delay

The contribution of the interconnect time delay was shown in Fig. 1.1. The time delay is due to the RC response time of the interconnect structure. The interline capacitance and ground capacitance are shown in Fig. 1.2. As the line to line distance

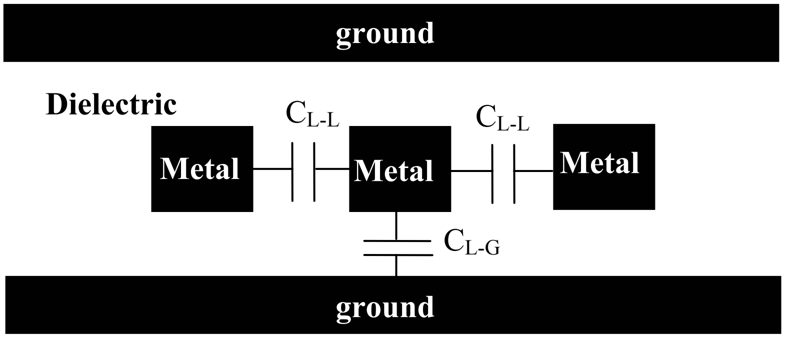

Figure 1.2 Diagram of interline capacitance, C_{L-L}, and line to ground capacitance, C_{L-G}.

decreases, the inter-line capacitance increases. In Fig. 1.3, the inter-line, line to ground, and the total capacitances are charted as a function of the metal line feature size (the distance from line to line) [1]. As the feature size shrinks, the line to line capacitance dominates the total capacitance.

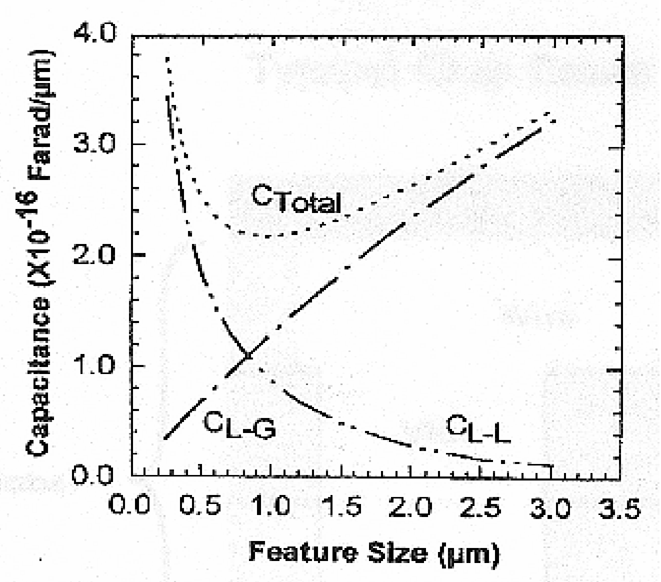

Figure 1.3 The line to ground, inter-line, and total capacitance vs. feature size [1].

Subtleties aside, the line to line capacitance is directly proportional to the dielectric constant, *k*, of the interlayer dielectric and inversely proportional to the distance between lines, *d*.

$$C_{L-L} \sim \frac{k}{d} \tag{1.1}$$

Hence, there are two methods of lowering the inter-line capacitance. One is to lower the dielectric constant of the material between the lines. The other is to increase the distance between metal lines; but this option is anathema to the industry, which wants higher densities and faster response times. Therefore, new low-k dielectrics are needed with a dielectric constant that is significantly lower than silicon dioxide (k=4.2). The International Technology Roadmap for Semiconductors (or ITRS) 2006 Update requires dielectric constants of k= 2.3 – 2.7 [2]. By the year 2010, the ITRS projects a reduction of dielectric constant to k= 2.1 – 2.4.

The RC time delay can also be engineered by decreasing the resistivity of the metal lines. The traditional metal line is Al(Cu) and it has a resistivity of ~3.3 μΩ-cm. It has been replaced by Cu, which has a resistivity of ~1.8 μΩ-cm. The benefit to the total resistance is hindered by the increase in metallization density. The total resistance is inversely proportional to the cross-sectional area of the metal line, which decreases with feature size. Hence, the need for a low-k material and copper is emphasized. A cross-section of the on chip interconnect structure is shown in Fig. 1.4. Copper interconnect lines are displayed with the surrounding low-k dielectric.

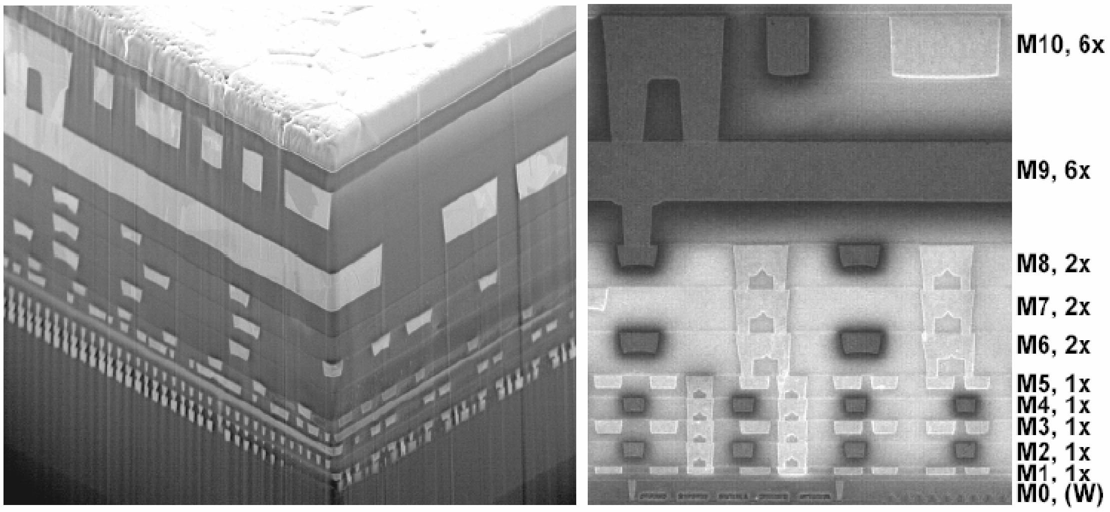

Figure 1.4 Interconnect structure for 90 nm CMOS Microprocessor. (Courtesy of IBM)

1.2 Fracture of low-k dielectrics and low-k interfaces

Fracture of the low-k dielectric and delamination at the low-k interfaces are significant reliability challenges. There are two principal driving forces for fracture in low-k dielectrics. The first is chemical mechanical polishing (CMP) during the damascene process. CMP applies a shear force on the top layer and causes damage to the layers below it [3, 4]. The other driving force is flip-chip packaging. In flip-chip packaging, CTE mismatch at the packaging level produces significant peel stresses on the interconnect structure often cracking the low-k.

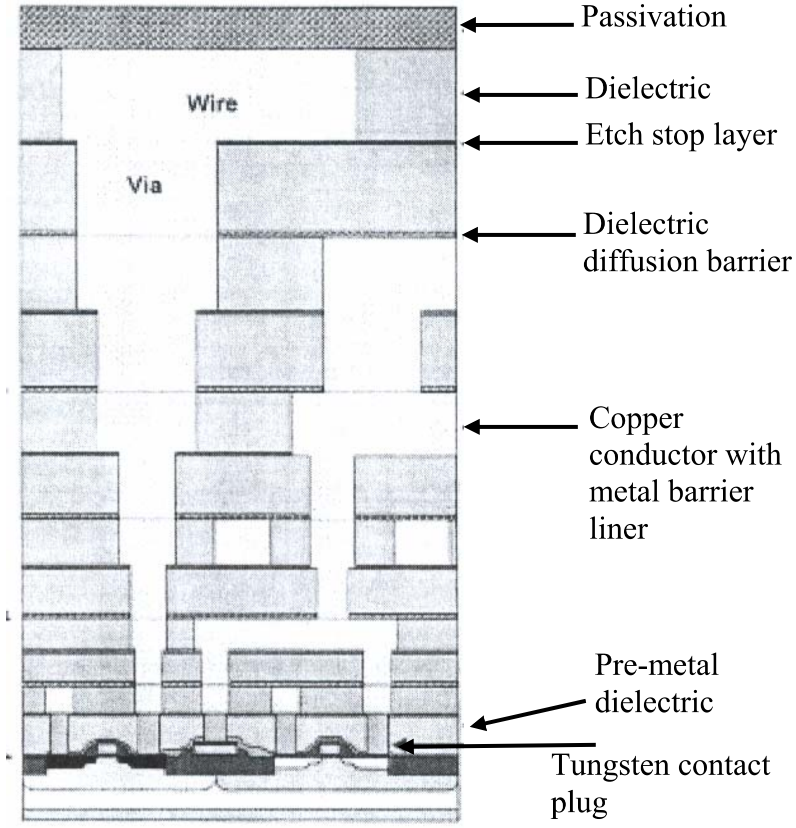

Figure 1.5 Cross section of the interconnect structure indicating the hierarchical scaling and passivation, etch stop, and diffusion barriers [1].

1.2.1 Chemical mechanical polishing and the damascene process

Copper interconnects are produced by a method known as the dual damascene process. The dual damascene process begins with the formation of a trench for the conductor line and a via, see Fig. 1.6. Then, the barrier layer and Cu metal seeds are deposited. Next, the Cu metal is deposited by electrochemical deposition (ECD), chemical vapor deposition (CVD), or physical vapor deposition (PVD). Finally, the excess copper is removed by chemical mechanical polishing.

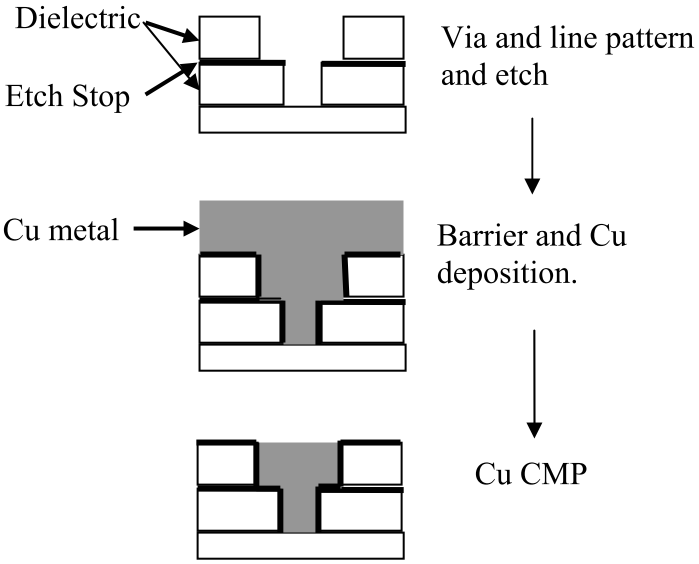

Figure 1.6 Illustration of the dual damascene process

Chemical mechanical polishing (CMP) uses a slurry with a pH of ~10. One to three pound/inch^2 of pressure is applied to the polishing pad, which rotates at variable speeds [4]. As each metal line is deposited, a shear stress is applied to the top film. Iacopi *et al.* used a 100 MPa shear stress in their finite element model of the CMP process [5]. Iacopi *et al*. have shown that the fracture toughness necessary to survive CMP depends on the location of the crack. Cracks near the top etch stop layer must have a fracture toughness of about 4.5 J/m^2, while the bottom interface of low-k/etch stop only requires a fracture toughness of 1.2 J/m^2 [5]. Despite the more detailed analysis of Iacopi, a fracture toughness of 5 J/m^2 is generally quoted for CMP survival [3]. However, Maitrejean *et al*. have shown that an adhesion of 2.7 J/m^2 can survive CMP [6].

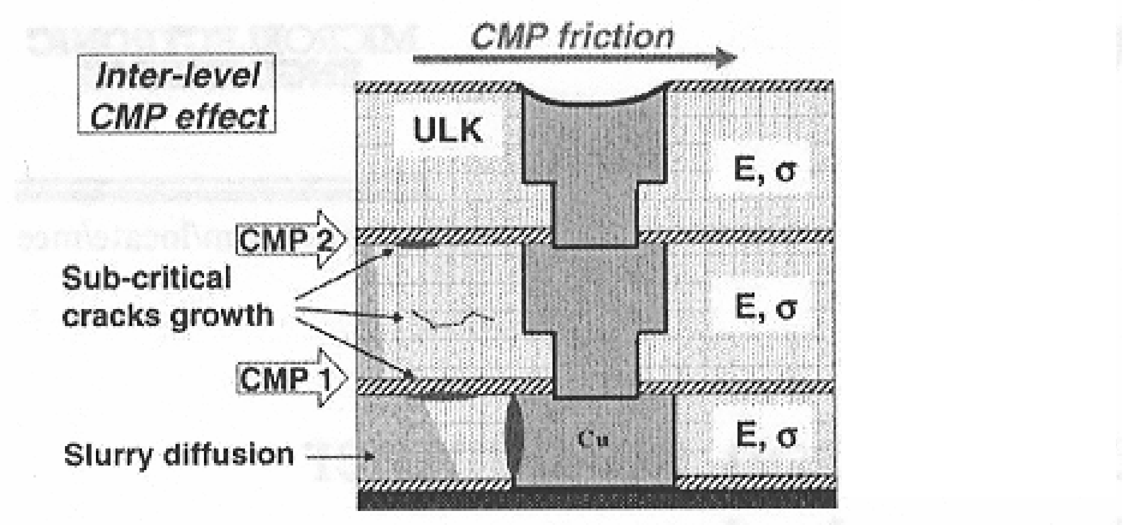

Figure 1.7 Schematic view of the interconnect structure after each CMP. Cracks can be seen in the ultra-low-k dielectric and at the interfaces. The modulus, *E*, and residual stress, *σ*, are indicated for each layer. Slurry diffusion is also indicated [4].

1.2.2 Flip-chip packaging

In flip-chip packaging, the active side of a microelectronic chip is connected, face down, to a substrate through a solder bump array. The substrate is typically made from organic polymeric materials and the coefficient of thermal expansion (CTE) is almost a factor of 10 larger than the silicon die. The CTE mismatch leads to significant shear stress on the outer solder bumps. The shear stress increases with distance from the neutral point or center of the die. In order to support the solder bumps, underfill is filled into the gap between the silicon die and the substrate, see Fig. 1.8 [7]. The underfill is an epoxy that has been filled with silica particles to increase its modulus and decrease its CTE. The cure temperature of a typical underfill is ~165°C. When the underfill cures, the silicon die and substrate are mechanically bound together and during cooling the entire package warps due to the mismatch in CTE. The package warping creates peel stresses on the low-k dielectric stack. Wang *et al*. have shown that, for cracks parallel to the underfill/die interface, the crack driving force can be as high as 16 J/m^2 [8].

When coupled with cracks created in the CMP process, the chip package interaction is a strong driving force for fracture and delamination.

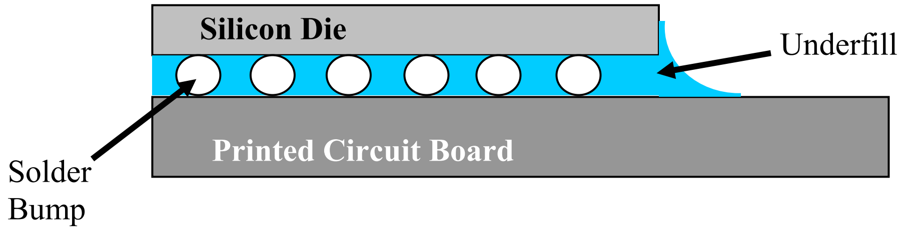

Figure 1.8 Diagram of half a flip-chip package at the underfill cure temperature.

1.3 Objectives and literature survey

The principal objective of low-k dielectric design is a decrease in the dielectric constant. However, engineering the k-value affects other material parameters such as the modulus, adhesion, and cohesive strength. The modulus of silicon dioxide is 72 GPa; yet, most silica based low-k moduli lie between 3 and 16 GPa, depending on the connectivity and porosity [9]. The decrease in adhesion with methyl content for an OSG low-k material is shown in Fig. 1.9 [10]. The dielectric constant decreases proportionally with the methyl content and, accordingly, the adhesion values in Fig. 1.9 decrease with dielectric constant. Low-k dielectrics will be discussed in detail in Chapter 2.

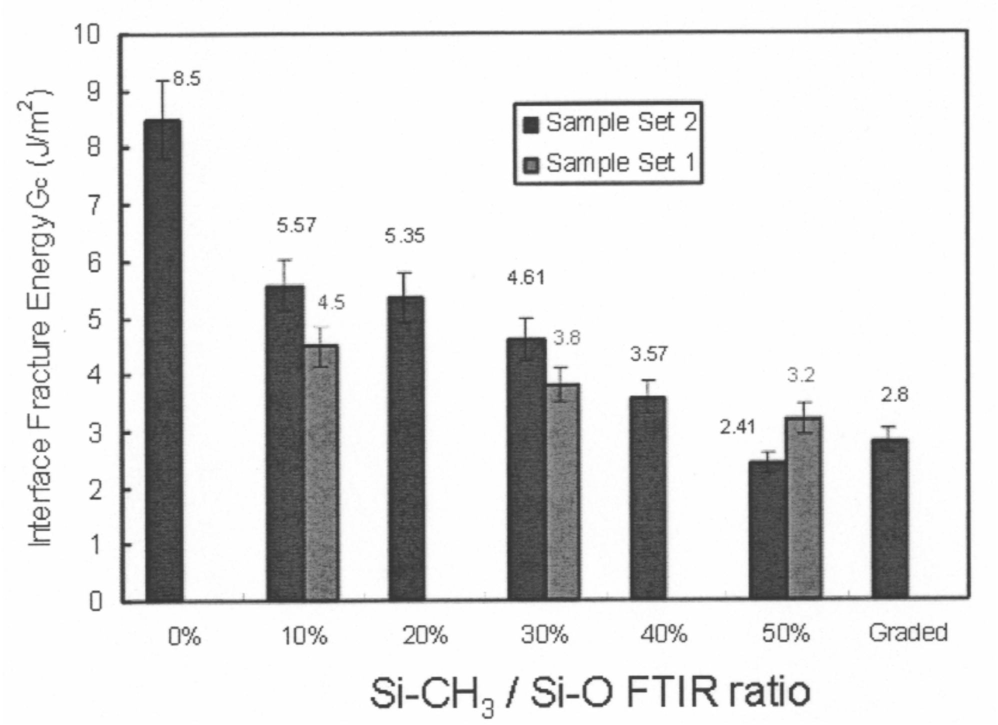

Figure 1.9 Adhesive fracture toughness of a OSG film vs. methyl content [10].

Porous OSG is the material studied in this dissertation. OSG is a hybrid material where methyl and hydrogen groups terminate the silicon dioxide network. A sacrificial porogen is added to OSG during deposition. During the cure step, the porogen is removed from the film leaving a porous OSG film. The incorporation of organic groups and porosity lower the dielectric constant. The mechanical and fracture properties are deleteriously affected.

Post deposition techniques, such as hydrogen plasma treatments, electron beam curing (e-beam), and ultra-violet light (UV) curing, have been used to improve the mechanical properties of p-OSG films with only a small change in dielectric constant

[11-16]. These methods accelerate the cure process without an increase in temperature. The energetic species scatter off (plasma and e-beam) or are absorbed (UV cure) by the low-k molecules, causing a short range rearrangement of molecular structure. Plasma treatment and e-beam curing suffered from a lack of specificity, being unable to target a specific molecule, and damaged p-FET devices with thick oxides [11, 12]. The damage was due to charging of the oxide and was specific to p-FET devices. n-FET devices were not affected as much. Consequently, UV curing was favored. Several authors have investigated the effect of UV curing on the dielectric constant, film modulus, density, and film shrinkage [12-16]. In general, the modulus and density increase after UV cure. The dielectric constant has been shown to increase as much as 11%, depending on the UV source used in the experiment. The density increases only a few percent; but the modulus increases from 55% to as much as 110% [12-14]. Other than this study, the published research on the fracture toughness of UV cured low-k is by Iacopi *et al*. [17] and Gage *et al*. [18]. Gage *et al*. [18] showed that UV curing increased the Four-point Bend Flexure (4pt bend) fracture toughness, but had no effect on Mode I or sub-critical crack growth (also Mode I). These results were attributed to the crack location and inhomogeneous structure modification in the bulk of the film.

In this dissertation, the effect of UV curing on the molecular structure and fracture properties of a porous OSG material with k ~2.5 is investigated. By following the UV exposure time, the modification of the molecular structure and its affect on material properties were examined. The results show, that unlike the results of Gage *et al*., UV curing increased the OSG fracture toughness for multiple Mode-mixes, including Mode I. These results were attributed to a uniform depth profile of the film. Yet, UV curing has no effect on sub-critical fracture. We propose that, unlike critical fracture, sub-critical crack propagation occurs by void nucleation and coalescence.

1.4 Overview

The purpose of this dissertation is to understand the effect of UV curing on the molecular structure and fracture toughness of an ultra low-k dielectric, k~2.5. The results of the study will be presented in Chapters 7 and 8. However, before discussing the results, some background and exposition are presented. The body of this dissertation is separated into 7 chapters.

In Chapter 2, the physical origin and engineering of dielectric materials are discussed. The magnitude of the dielectric constant in an insulator is dependent on the frequency of the driving electric field. The origin of the electronic and ionic contributions will be explained and their characteristic resonance frequencies given. The role of porosity will also be discussed. The Claussius-Mossotti equation is introduced to connect the microscopic polarizability to the macroscopic dielectric constant. Finally, a review of specific low-k dielectrics will be presented.

A review of the physics needed to understand the interaction of light with matter and the method of ultra-violet light curing are presented in Chapter 3. In simple terms, a two atom system must absorb a photon with energy equal to or greater than the cohesive energy. After the photon is absorbed, a chemical rearrangement is made to a more stable compound. The details of this process will be discussed. The photon absorption rate will be calculated in terms of Fermi's Golden Rule. In order to calculate Fermi's Golden

Rule, the electron states in the molecule must be examined. The electron molecular states will be presented and estimates made using tight binding theory. Finally, the method of UV curing is presented.

Chapter 4 presents the mechanics theory needed to analyze a crack at a bi-material interface. The chapter begins with an overview of solid mechanics, introducing the theory of elasticity for plane strain and the symmetry principles at an interface. The majority of this chapter will be dedicated to fracture mechanics. The topics in fracture that will be discussed are cohesive failure, failure at an interface, and inelastic processes at the crack tip. Finally, the theory of stress corrosion, as applied to sub-critical fracture, is presented.

A few analytical techniques will be reviewed in Chapter 5. These techniques include X-ray Reflectivity (XRR), X-Ray Photoelectron Spectroscopy (XPS), Spectroscopic Ellipsometry, and Fourier Transform Infrared Spectroscopy (FTIR). XRR was used to measure the density, while XPS was used to measure the atomic composition. Spectroscopic Ellipsometry was used to measure uniformity of the refractive index and film thickness. Finally, FTIR was employed to determine the molecular structure. The majority of this chapter will be devoted to a discussion of FTIR.

Chapter 6 will discuss the different techniques in fracture that were used to obtain the fracture toughness of UV cured OSG. The chapter begins with a discussion of sample preparation, followed by a presentation of the Four-point Bend Flexure Technique (4pt-bend). The Mixed-Mode Double Cantilever Beam (MMDCB) will be discussed next and, finally, the chapter will conclude with a discussion on sub-critical fracture measurements.

In Chapters 7 and 8, an investigation of the effect of UV curing on the molecular structure and fracture properties of a porous OSG material with k ~2.5 is presented. By following the UV exposure time, the modification of the molecular structure and its effect on material properties are examined. These results are divided in two parts. Chapter 7, Part I, discusses the influence of UV curing on the material properties and molecular structure of the ULK film. The material data presented will include changes in density, mass, and k-value. Fourier Transform IR (FTIR) and X-ray Photo-emission Spectroscopy (XPS) studies will be used to investigate the molecular structure. The changes in molecular structure will be correlated to condensation reactions with UV light that directly affect material properties. In Chapter 8, the second part of the results section, the effect of UV curing on the fracture properties of the low-k film are investigated. It is shown that UV curing increases the critical fracture energy for all mode-mixes and the crack location was found to be cohesive (in the bulk, close to the interface) for all cracks. However, the sub-critical fracture toughness was insensitive to UV curing. This difference is explained by void nucleation and coalescence during sub-critical crack growth.

Chapter 2 Low dielectric constant materials

In Chapter 2, the physical origin and engineering of dielectric materials are discussed. The magnitude of the dielectric constant in an insulator is dependent on the frequency of the driving electric field. The electronic and ionic contributions will be explained and their characteristic resonance frequencies given. The role of porosity is discussed. The Claussius-Mossotti equation will be introduced to connect the microscopic polarizability to the macroscopic dielectric constant. Finally, a review of specific low-k dielectrics will be presented.

2.1 The dielectric constant

In 1837, Michael Faraday charged two geometrically identical capacitors to the same electro-static potential [1]. The first capacitor was filled with air and the second with a dielectric material. He found that the capacitor that was filled with a dielectric material maintained more charge than the capacitor filled with air. However, if a fixed charge is placed on the capacitor, the electro-static potential, *V*, for a capacitor filled with a dielectric is *1/k* smaller than a capacitor filled with air.

$$V_{dielectric} = \frac{V_{air}}{k} \tag{2.1}$$

where *k* is the dielectric constant. A simple model of a dielectric response is shown in Fig. 2.1. A charge σ is placed on the capacitor plates and the resulting electric field, *E*, is

$$E = \frac{4\pi\sigma}{k} \tag{2.2}$$

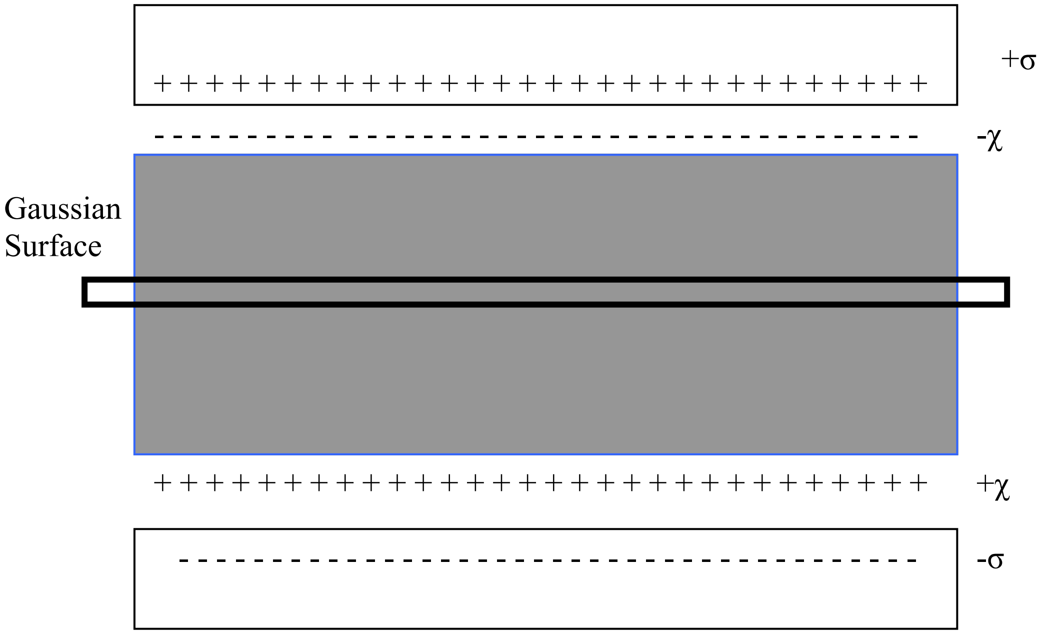

Figure 2.1 A capacitor filled with a dielectric material. The dielectric is polarized and the electric field in the dielectric is reduced. The surface charge denstiy on the capacitor is σ and the polarization charge on the surface of the dielectric is χ.

The electric field can also be explicitly constructed from the surface charges on the capacitor and the dielectric. The polarization of the dielectric leads to a surface charge density of χ.

$$E = 4\pi(\sigma - \chi) \tag{2.3}$$

Using Eqs. 2.3 and 2.2, the polarization charge density can be written

$$\chi = (k-1)E \tag{2.4}$$

The polarization density, χ, is the same on any Gaussian surface within the dielectric in Fig. 2.1. The charge density is due to the alignment of atomic and molecular dipoles with the applied external field, $\underline{E}$. The atomic and molecular dipoles are defined to be a net charge, q, displaced by a distance, s.

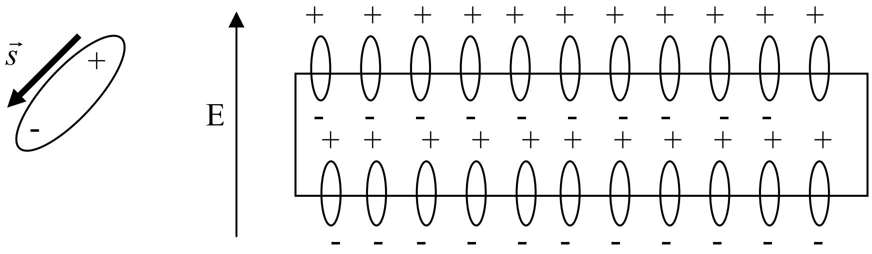

Figure 2.2 An atomic dipole and the polarization along a Gaussian surface.

$$\vec{p}_i = q_i \vec{s}_i \tag{2.5}$$

If N_i is the number of dipoles of type i within a small volume V, the polarization vector field can be defined as

$$\vec{\boldsymbol{P}}(\vec{\boldsymbol{r}}) = \sum_{\boldsymbol{i}} N_{\boldsymbol{i}} \langle \vec{\boldsymbol{p}}_{\boldsymbol{i}} \rangle \tag{2.6}$$

where the average <p> is taken over the dipole-moments within volume V centered at position r.

In order to relate the macroscopic dielectric properties, k, to the microscopic properties, the polarizability, a distinction must be made between the local and global electric field [2]. It is customary to consider the local electric field as the sum of three parts.

$$E_{local} = E_0 + E_1 + E_2 \tag{2.7}$$

where

E_0 is the electric field from the external charges on the capacitor plates.

E_1 is the electric field from the induced polarization charges on the dielectric material.

E_2 is the electric field inside a dielectric cavity.

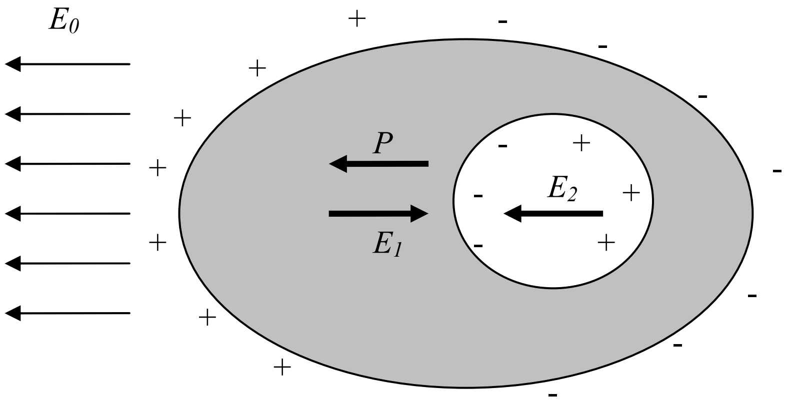

Figure 2.3 Diagram of the constituent fields in a dielectric. The sum of all fields is taken at the center of the cavity. The cavity is not shown to scale.

A diagram of the constituent electric fields in a dielectric is shown in Fig. 2.3. A small cavity, not shown to scale, is removed. The sum of the fields is taken at the center of this cavity. The sum of the E_0 and E_1 has already been given in Eq. 2.3 for a parallel plate capacitor.

$$E_0 + E_1 = 4\pi(\sigma - \chi) \tag{2.8}$$

To calculate the final field, E_2, the effect of polarization on the spherical cavity is calculated. The surface charge density on the small cavity is $-P\cos(\theta)$, where P is the polarization vector from Eq. 2.6. With the knowledge of the surface charge density, the electric field at the center of the cavity is

$$E_2 = \frac{4\pi \cdot P}{3} \tag{2.9}$$

When calculating the total field, the field due to the dielectric material, that was removed to make the cavity, was not included. This field is trivially zero, see Kittel [2].

Therefore, the local electric field for any point inside the dielectric material in a parallel plate capacitor is

$$E_{local} = 4\pi \cdot (\sigma - \chi) + \frac{4\pi \cdot P}{3} \tag{2.10}$$

The local and global properties of a dielectric are related through the polarization vector field, P(r). Returning to Eq. 2.6, the dipole moment of an atom or molecule is proportional to the applied local field. The proportionality constant is called the polarizability. In general, the polarizability is a second-rank tensor; but, only the isotropic value will be consider here.

$$\vec{\boldsymbol{p}}_i(\vec{\boldsymbol{r}}) = \alpha_i \cdot \vec{\boldsymbol{E}}_{local} \tag{2.11}$$

where α is the polarizability. Therefore, the Claussius-Mossotti equation can be derived from the ratio of the magnitude of *P/E* [2].

$$\frac{k-1}{k+2} = \frac{4\pi}{3}\sum_i N_i \alpha_i \tag{2.12}$$

The Claussius-Mossotti equation connects the macroscopic characterization of a dielectric material, the dielectric constant, to the microscopic characterization, the polarizability.

2.2 The polarizability

In the previous section, the idealized dipole moment was introduced in Eq. 2.5 and later the dipole moment was shown to be proportional to the local electric field. The constant of proportionality is called the polarizability, α. The total polarizability can be separated into three parts—electronic, ionic, and dipolar, Fig. 2.4 [2]. The electronic polarizability is due to the displacement of the atomic nucleus and its surrounding electron shell from its equilibrium position. The ionic polarizability arises from the displacement of positive and negative ions in a molecule. Finally, the dipolar contribution is due to the alignment of permanent dipoles with the applied electric field. The dipolar contribution is relevant to gases and liquids, but is mostly suppressed in solids. Each component of the polarizability has a characteristic resonance frequency [3]. Later, the polarizability will be measured at different frequencies in order to separate the components of the total polarizability.

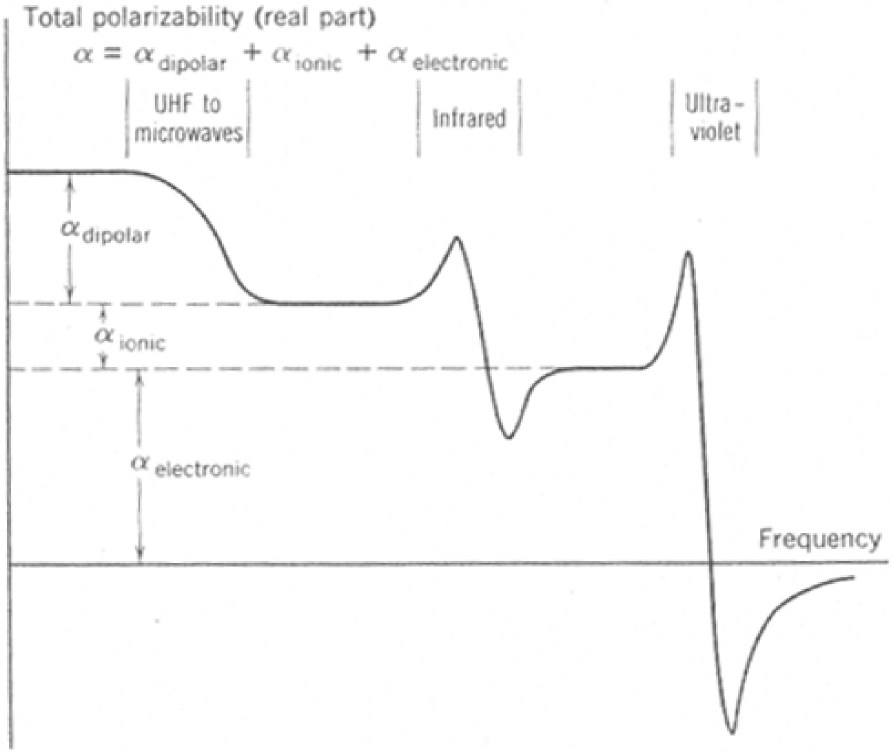

Figure 2.4 The total polarizability as a function of frequency [2].

2.2.1 The electronic polarizability

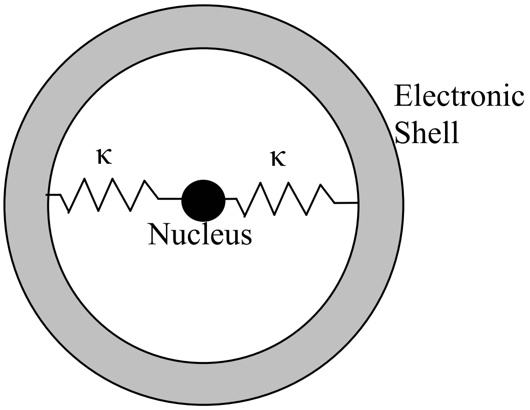

Figure 2.5 Simple model of an atomic nucleus bound to the electron shell with a harmonic force, κ.

A simple model of an atom is shown in Fig. 2.5. The nucleus is bound harmonically to the surrounding electron shell with force constant, κ. The nucleus is considerably more massive than the electron shell, and its displacement is fixed at zero. The electron shell is free to vibrate. Consider an applied electric field of $E(t) = E_{local} \sin(\omega \cdot t)$. The balance of forces is

$$m\frac{d^2x}{dt^2} + m\omega_0^2 x = -eE_{local} \sin(\omega \cdot t) \tag{2.13}$$

If the displacement is taken to be the harmonic function, $x(t) = x_0 \sin(\omega \cdot t)$, the solution for the polarizability, for the dipole moment $p = -ex_0$, is

$$\alpha_e = \frac{e^2/m}{\omega_0^2 - \omega^2} \tag{2.14}$$

where m is the mass of an electron, e is the electron charge, and ω_0 is the resonance frequency $\sqrt{\frac{\kappa}{m}}$. The characteristic frequency for electronic polarization is ~10^{15} Hz [2, 3], which is the ultra-violet region of the electro-magnetic spectrum.

Table 2.1 Polarizability of different atoms [4]

Atom	**Polarizability**
H	0.667
C	1.76
O	0.802
F	0.557
Si	5.38

2.2.2 The ionic polarizability

A linear chain of ions is presented in Fig 2.6. Each positive and negative ion is bound by an interatomic harmonic potential. The harmonic potential is characterized by a spring constant κ. Let the positive ions be displaced a distance δ and the negative ions

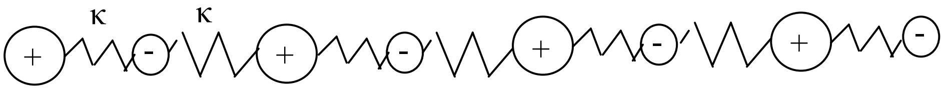

Figure 2.6 A linear chain of bonded ions. The ions are connected by a harmonic force with force constant, κ.

displaced a distance ζ. The charge on each ion is $+q$ and $-q$. Therefore, the dipole moment can be expressed as $p = q(\delta - \varsigma)$. Like the case of electronic polarizability, the balance of forces leads to an expression for the polarizability

$$\alpha_i = \frac{q^2}{\omega_T^2 - \omega^2}\left(\frac{1}{M_+} + \frac{1}{M_-}\right) \tag{2.15}$$

where ω_T is the angular frequency of the transverse optical phonon, M_+ and M_- are the masses of the positive and negative ions, and q is the magnitude of the charge on each ion. The characteristic frequency, $\omega_{T,}$, is approximately 10^{13} Hz, which is in the infrared region of the electro-magnetic spectrum [2, 3].

The evaluation of Eq. 2.15 is simple for an ionic crystal such as sodium chloride; but, even largely covalent crystals, such as silicon dioxide, have some ionic character. The degree of ionic character is determined by the difference in electronegativity, first introduced by Pauling [5]. Since the bond lengths are taken to be fixed, the electronegativity indicates the amount of charge distributed on either atom in the molecule. The atom with the highest electronegativity is the negatively charged ion. By determining the ionic character, the charge q in Eq. 2.15 can be estimated.

Eqs. 2.14 and 2.15 are resonance equations. It is evident from Fig. 2.4 that, while peaks occur at the resonance frequency, the dielectric constant does not diverge. Consequently, a dissipation mechanism must exist at resonance. The dissipation is most likely the emission of photon or phonon radiation.

Table 2.2 Electronegativity values for different atoms [5].

Atom	**Electronegativity**
H	2.1
C	2.5
O	3.5
F	4.0
Si	1.8

Table 2.3 Bond length, Electronegativity difference, and partial charge *q* for important bonds.

Bond	**Bond Length (Å)**	**Electronegativity Difference**	**q (e)**	**p (e* Å)**
Si-C	1.87	0.7	0.12	0.224
Si-O	1.63	1.7	0.51	0.831
Si-H	1.48	0.3	0.025	0.037
Si-F	1.58	2.2	0.70	1.106

In summary of section 2.2, the polarizability for a solid has two major components— electronic and ionic. The polarizabilities have been shown to be frequency dependent and proportional to the electronic and ionic charge. The electronegativity was used to calculate the partial ionic character of covalent bonds. The Claussius-Mossotti equation can now be written as

$$\frac{k-1}{k+2}=\frac{4\pi}{3}\left(N_e\alpha_e+N_i\alpha_i\right) \tag{2.16}$$

where N_e and N_i are the number of electronic and ionic dipoles per unit volume. Often, the density of dipoles is approximated to be the number of molecules per unit volume.

2.3 Adding porosity

The principle method of lowering the dielectric constant is to lower the polarizability per unit volume. This can be accomplished by two methods. The first method is to decrease the molecular dipole moment of the material. Using Table 2.3, a substitution of silicon-oxygen bonds with silicon-carbon bonds will lead to a lower dipole moment and consequently lower the dielectric constant; but, a substitution of fluorine will also lower the dielectric constant. The substitution of fluorine increases the dipole moment; yet, the increase in free volume is sufficient to lower the dielectric constant. This effectively decreases the number of molecules per unit volume in Eq. 2.16. The example of Si-F illustrates that an increase in free volume can be very effective in reducing the dielectric constant [6]. A more significant method of introducing free volume is the addition of pores into the dielectric material. There are principally two methods of introducing pores—constitutive and subtractive [3]. Constitutive porosity occurs when, during cure, the material cross-links in a manner that leaves nano-sized pores. Nanoclustering silica is an example of constitutive porosity. Subtractive porosity disperses a volatile material into the dielectric. During annealing of the dielectric, the volatile material burns out of the dielectric, leaving nano-scale pores [7]. The dielectric constant for a two component system is [3]

$$\begin{aligned}\frac{k-1}{k+2} &= \eta\frac{k_1-1}{k_1+2}+(1-\eta)\frac{k_2-1}{k_2+2} \\ &= (1-\eta)\frac{k_2-1}{k_2+2}\end{aligned} \tag{2.17}$$

where k_i is dielectric constant of component *i* and η is the porosity. The first term in Eq. 2.17 vanishes, since the dielectric constant of air is 1.

2.4 An overview of low-k materials

A low-k material is generally any dielectric with a k-value less than or equal to 3. An ultra-low-k material has a k-value of 2.5 or less. In this section, a review of low-k materials is presented. The section begins with a review of traditional silicon dioxide and describes how this basic material has been engineered to form low-k dielectrics. The deposition technique, plasma enhanced chemical vapor deposition (PECVD), is discussed. Finally, a review of the different types of silica based low-k dielectrics is presented.

2.4.1. Engineering silicon dioxide

The traditional interlayer dielectric is silicon dioxide, SiO_2. Silicon dioxide has a dielectric constant of ~4.2, a modulus of ~73 GPa, a density of ~2.2. g/cm^3, and a fracture toughness of ~10 J/m^2. It is a mechanically robust dielectric. Unfortunately, the desired dielectric constant in the new design rule is below 2.5. In order to achieve this goal, traditional SiO_2 has been engineered, by the incorporation of terminating organic molecules, to create materials with low intrinsic dielectric constants, as low as 2.8. With the introduction of porosity, an ultra-low k value of 2.1 has been achieved [7].

The sacrifice for achieving low k-values is a mechanically weak material. The modulus of many low-k materials is ~3-16 GPa, while the fracture toughness is ~6 J/m^2 and below [3, 8]. In this thesis, only low-k structures based on silicon dioxide will be discussed. The low-k materials incorporate organic groups into their structure, particularly hydrogen and methyl groups. The exact values of the material constants, such as modulus and fracture toughness, are dependent on the porosity and the extent of organic group incorporation.

Organic groups are incorporated by the use of precursor materials that can be deposited by spin-on or plasma enhanced chemical vapor deposition (PECVD) [7]. The precursors can either thermally decompose (spin-on) or decompose above the substrate in the plasma (PECVD). The decomposed precursors form a dielectric material with a silicon dioxide back bone and terminating organic groups. The terminating groups are either hydrogen or methyl groups.

Common low-k materials are hydrogen silsesquioxane (HSQ), methyl silsesquioxane (MSQ), carbon-doped silica (SiCOH), and organosilicate glass (OSG). Technically, OSG is a carbon-doped oxide like SiCOH. In this thesis, the material under investigation is OSG. The precursor used in this thesis was diethoxymethylsilane (DEMS), but the exact deposition technique is proprietary. A common OSG precursor is tetramethylcyclotetrasiloxane (TMCTS) [9]. During the deposition of DEMS and TMCTS, a volatile organic species is mixed with the precursor, creating a dual phase material. The organic species or porogen is removed by either annealing the film for four hours at 400°C or annealing it with energetic species such as electrons or photons. When annealing with energetic species, the deposition surface is maintained at 350-400°C.

2.4.2 Plasma enhanced chemical vapor deposition (PECVD)

Our low-k organosilicate films were deposited by plasma enhanced chemical vapor deposition (PECVD), using a DEMS precursor and aromatic-organic porogen. PECVD deposition typically occurs in a parallel plate reactor using RF power at 13.56 MHz. The precursor and porogen are vaporized and carried into the reactor by an inert gas, e.g. helium or argon. The silicon substrate is maintained at a negative voltage with respect to the plasma. The precursor decomposes at the lower levels of the plasma and is accelerated to the negative electrode where it forms the OSG film. The RF power must be sufficiently low to produce an OSG film; yet, high enough to dissociate the organic porogen and incorporate the fragments into the film [7].

2.4.3 Hydrogensilsesquioxane (HSQ) and methylsilsesquioxane (MSQ)

Hydrogensilsesquioxane (HSQ) and methylsilsesquioxane (MSQ) are two low-k materials with essentially the same structure [10]. Before curing, the molecular structure of both materials consists of both cage and network structures. The cage structure is shown in Fig. 2.7, where the terminating molecule is either hydrogen or methyl. The network structure is the base silicon dioxide structure. The bond angle is the easiest way to differentiate between cage and network. The network structure has a silicon-oxygen-silicon bond angle of ~144°, while the average bond angle for cage structures is ~150° [9]. The cage structure creates a void in the material, contributing a pore with a diameter of ~0.5 nm and volume of 0.065 nm^3, which is an example of constitutive porosity.

During thermal annealing at 400°C, portions of the cage structure transform to network [10].

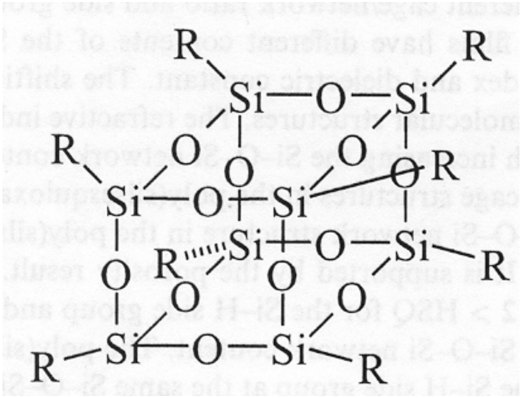

Figure 2.7 The molecular structure of HSQ, R=H and MSQ, R=CH_3 [10].

2.4.4 Organosilicate glass

Organosilicate glass or OSG is a hybrid material. It contains both hydrogen and methyl terminating groups. It also contains a new sub-structure—sub-oxide. The sub-oxide structure has a silicon-oxygen-silicon bond angle of less than ~140°. The structure of a typical OSG material is shown in Fig. 2.8 [9].

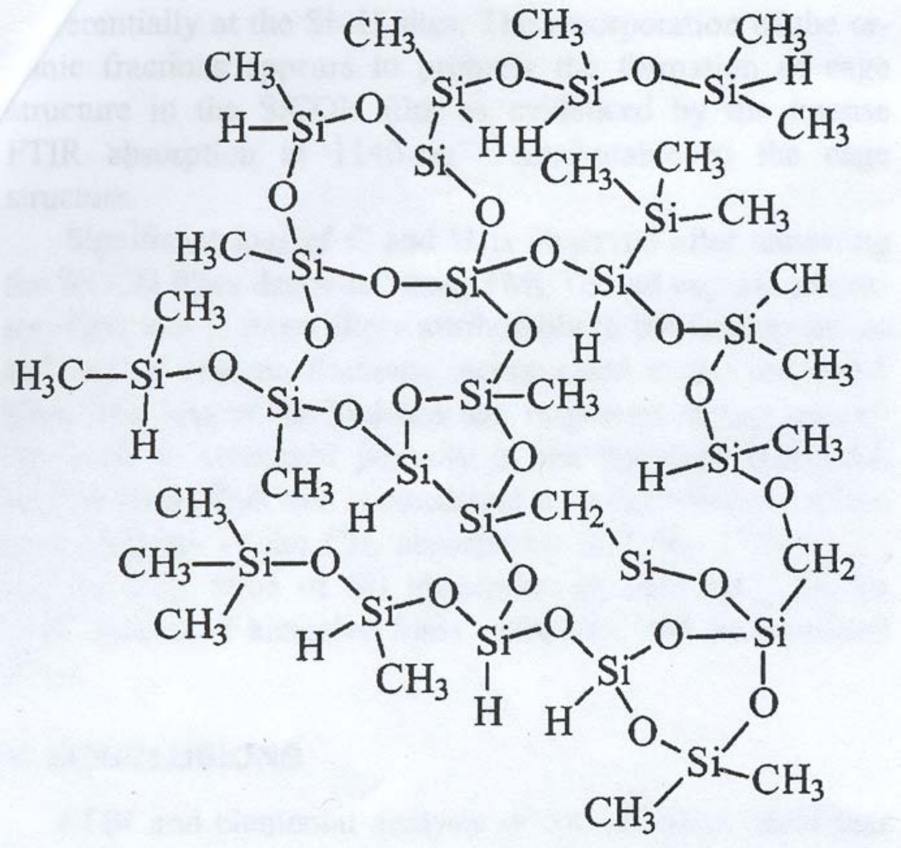

Figure 2.8 Structure of a typical OSG material. This structure reflects the annealed OSG film deposited from the precursor only [9].

When pores are added to the OSG, the silicon-oxygen-silicon bond angle increases to accommodate the pores. The increased bond angle is attributed to the cage structure. Therefore, a quantitative account of the cage structure will be proportional to the number of pores in the material. Later, FTIR analysis will show a decrease in cage structures with UV curing. This decrease will be attributed to pore collapse. A diagram of the cage structures surrounding a pore is shown in Fig. 2.9 [9].

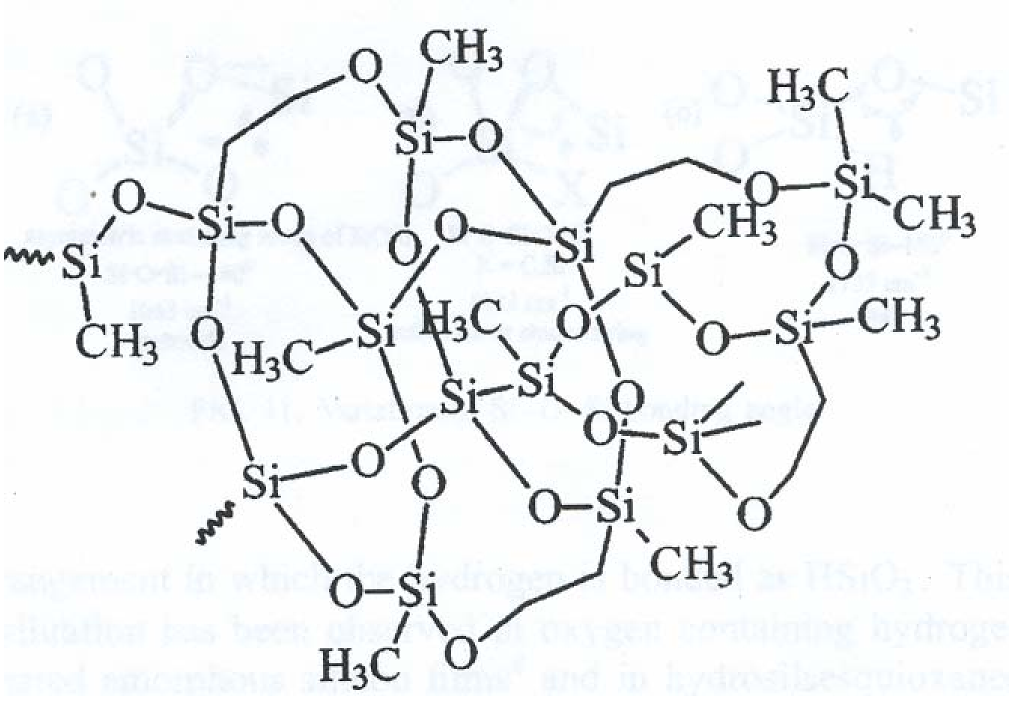

Figure 2.9 Diagram of porous cage structure of annealed OSG with organic porogen [9].

The basic molecular units of OSG are combinations of silicon, oxygen, and methyl groups. The connectivity of the molecular units is labeled according to the number of oxygen atoms. Silicon surrounded by four oxygen atoms (k=4.2) is labeled Q; silicon with three oxygen atoms and one methyl group (k=3.09) is labeled T; silicon with two oxygen atoms and two methyl groups (k=2.71) is D; silicon with one oxygen and three methyl groups (k=2.53) is labeled M [11]. These results are summarized in Table 2.4.

Table 2.4 shows that a decrease in connectivity leads to a lower dielectric constant; yet, it is not known how the decrease affects the strength of the material. Furthermore, it is not known if it is better to increase porosity or decrease connectivity.

In Fig. 2.10, two plots of the normalized modulus are shown for an OSG material from Applied Materials [11]. The dense version is called Black Diamond I. The porous version is called Black Diamond II. It is evident that decreasing the dielectric constant, k, through porosity is preferable.

Table 2.4 Connectivity and Molecular Structure [11]

Structure	**Connectivity**	**Dielectric Constant**
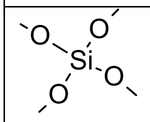	Q	4.2
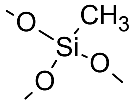	T	3.09
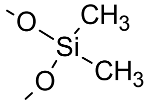	D	2.71
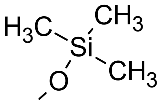	M	2.53

2.5 Summary

In Chapter 2, low-k dielectric materials and the physical origin of the dielectric constant were discussed. The polarization vector and the microscopic polarizability were introduced. The Clausius-Mossotti equation was used to relate the macroscopic dielectric constant to the microscopic polarizability. Separate contributions to the polarizability, electronic and ionic, were shown to be frequency dependent. Also, the ionic contribution

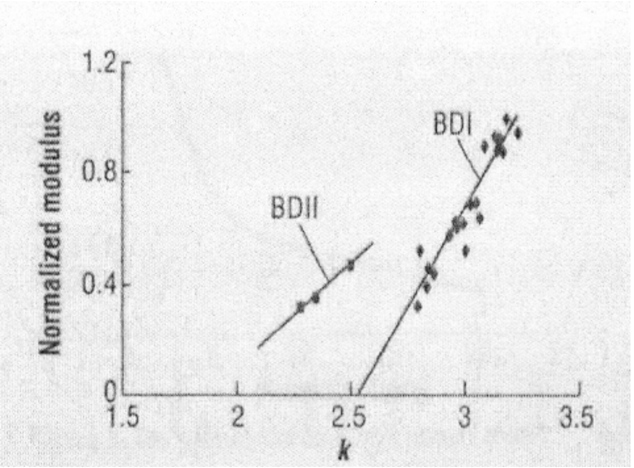

Figure 2.10 Normalized modulus vs. dielectric constant for Black Diamond I and II [11].

was directly related to the charge on the ions. The electronegativity was used to predict the charges in covalently bonded molecules. The dielectric constant was also related to the porosity of the film. An overview of low-k dielectrics was presented, including HSQ, MSQ, and OSG. Additionally, the connectivity of OSG was discussed.

Chapter 3 The interaction of light with matter and UV curing

In Chapter 3, the interaction of light with matter and the method of ultra-violet light curing are reviewed. In simple terms, a two atom system must absorb a photon with energy equal to or greater than the cohesive energy. After the photon is absorbed, a chemical rearrangement is made to a more stable compound. The details of this process will be discussed. The chapter begins with the classical electromagnetic field and the introduction of the transverse gage. Next, the electromagnetic field will be quantized. The photon absorption rate will be calculated in terms of Fermi's Golden Rule. In order to calculate Fermi's Golden Rule, the electron states in the molecule must be examined. The electron molecular states will be presented and estimates made using tight binding theory. Finally, the method of UV curing will be presented.

3.1 The classical electromagnetic wave

In the absence of electromagnetic sources in an infinite medium, Maxwell's Equations can be written as [1]

$$\begin{aligned} &\nabla \bullet \vec{E} = 0 \qquad && \nabla \times \vec{\mathrm{E}} + \frac{1}{\mathrm{c}}\frac{\partial \vec{B}}{\partial t} = 0 \\ &\nabla \bullet \vec{B} = 0 \qquad && \nabla \times \vec{\mathrm{B}} - \frac{\mu\varepsilon}{\mathrm{c}}\frac{\partial \vec{E}}{\partial t} = 0 \end{aligned} \tag{3.1}$$

Both the electric and magnetic field, E and B, separately solve Eq. 3.1. The parameters μ and ε are used to characterize a dispersive media. They are equal to unity in free space.

By combining the left and right hand side of Eq. 3.1, the wave equation that governs the propagation of electro-magnetic waves is derived.

$$\nabla^2 u - \frac{1}{v^2}\frac{\partial^2 u}{\partial t^2} = 0$$

$$v = \frac{c}{\sqrt{\mu\varepsilon}} \tag{3.2}$$

Equation 3.2 is true for both electric and magnetic fields. From here on, fields will be considered free and the electric and magnetic fields are in phase. Maxwell's equations can be written in terms of the vector potential A, where the transverse gage is chosen $\nabla \bullet \vec{A} = \varphi = 0$. (The derivation presented here and through section 3.2 are attributed to Baym [2] and Craig and Thirunamachandran [3])

$$\vec{E} = -\frac{1}{c}\frac{d\vec{A}}{dt}$$

$$\vec{B} = \nabla \times \vec{A} \tag{3.3}$$

The solution to equation (3.2) can now be written solely in terms of the vector potential. The vector potential, $\underline{A}(\underline{r}, t)$, is represented as a Fourier Series

$$\vec{A}(\vec{r},t) = \frac{1}{\sqrt{V}}\sum_{k\lambda}\left[a_{k\lambda}\cdot\vec{\lambda}\cdot\exp\left(i\vec{k}\cdot\vec{r} - i\omega t\right) + a_{k\lambda}^{*}\cdot\vec{\lambda}^{*}\cdot\exp\left(-i\vec{k}\cdot\vec{r} + i\omega t\right)\right] \tag{3.4}$$

In Eq. 3.4, the polarization vector, λ, is always normal to the wavevector, *k.* There is a separate amplitude, $a_{k\lambda}$, for each wavevector and polarization. The wavevector, *k*, and the angular frequency, ω, are related by $\omega / k = c$. The energy of an electromagnetic wave is

$$U_{field} = \frac{1}{8\pi}\int d^3r\left(\vec{E}^2(\vec{r},t) + \vec{B}^2(\vec{r},t)\right) \tag{3.5}$$

The field energy can be rewritten in terms of the Fourier amplitude of the vector potential as

$$U_{field} = \sum_{k\lambda} \frac{\omega_k^2}{2\pi \cdot c^2} \left| a_{k\lambda} \right|^2 \tag{3.6}$$

The form of Eq. 3.6 is directly analogous to the energy of a harmonic oscillator. In fact an electromagnetic wave is a propagating oscillator and this model will be used to quantize Eq. 3.6.

3.2 Quantizing the electro-magnetic field

In the previous section, the energy in the electro-magnetic field was shown to be the same as that for a harmonic oscillator. Each mode, *k* and λ, of the radiation field is represented by an oscillator. This analogy can be made formal by the black-body argument. Any modern quantum mechanics text demonstrates the quantization of a harmonic oscillator [4, 5]. The method defines a new operator called the number operator, N. The number operator commutes with the energy and therefore can be simultaneously defined. It counts the number of quanta in the energy state. Assuming that the oscillator has one natural frequency, the energy can be quantized in the following manner

$$U_{osc} = \left(n + \tfrac{1}{2}\right) \cdot \hbar\omega \qquad n = 0, 1, 2, ... \tag{3.7}$$

Using Eq. 3.6, the energy of the electro-magnetic field is rewritten by pointing out the equivalence between the number operator and the field amplitudes. That is

$$|a_{k\lambda}|^2 = \frac{2\pi\hbar c^2}{\omega} N_{k\lambda} \tag{3.8}$$

The number operator $N_{k\lambda}$ counts the number of quanta or photons in the state, k and λ. The energy of the electro-magnetic field is expressed in terms of the number of photons with energy $\hbar\omega$.

$$U_{field} = \sum_{k\lambda} \left(N_{k\lambda} + \frac{1}{2} \right) \hbar\omega_k \tag{3.9}$$

The vacuum state of the electromagnetic field has infinite energy. This energy can always be subtracted off and should not lead to problems with the theory. Notice that the energy in the electro-magnetic field can accommodate any number of photons in any state, *k* and λ. This is a property of a Bosonic system.

An electro-magnetic wave (EM) has all the properties of a particle with mass zero. Even in the classical field equations, it is possible to assign a momentum and angular momentum to an EM wave. A very elegant manner of finding the momentum of a photon is to invoke the kinematic energy in Special Relativity.

$$E^2 - c^2 \vec{p} \cdot \vec{p} = \left(mc^2 \right)^2 \tag{3.10}$$

The energy of a photon is $\hbar\omega_k$ and it has a mass of zero. Therefore the momentum of a photon is

$$p = \frac{\hbar\omega}{c} \tag{3.11}$$

We will not derive the angular momentum of a photon. It has a spin of one. Unlike most spin 1 particles, it has only two spin orientations, 1 and -1.

The rate of photon absorption is given by Fermi's Golden Rule [2]

$$\Gamma^{abs}(\omega) = \left[\frac{N_{k\lambda}c}{V}\right]\frac{4\pi^2 e^2}{\omega \cdot c}\sum_n \left|\langle n|j_{-k}|0\rangle\right|^2 \delta\left(E_n - E_0 - \hbar\omega\right) \tag{3.12}$$

The interaction term, $\langle n|j_{-k}|0\rangle$, is the Fourier component of the current operator.

$$\begin{gathered}\langle n|j_{-k}|0\rangle = \int e^{-i\vec{k}\bullet\vec{r}}\langle n|j(\vec{r})|0\rangle d^3r = \int\left[1 - i\vec{k}\bullet\vec{r} + \ldots\right]\langle n|j(\vec{r})|0\rangle d^3r \\ j(\vec{r}) = \frac{1}{2}\sum_j {}^{dx_j}\!\!/_{dt} \cdot \delta\left(\vec{r} - \vec{r}_j\right) + \delta\left(\vec{r} - \vec{r}_j\right) \cdot {}^{dx_j}\!\!/_{dt}\end{gathered} \tag{3.13}$$

Only the first term in the expansion of the exponential is required. The integral of the current operator reduces the interaction term to the expectation value for the electron velocity; yet, the electron velocity can be calculated by the Heisenberg Equation of Motion.

$$\begin{gathered}\langle n|j_{-k}|0\rangle \cong \sum_j \langle n|\frac{dx_j}{dt}|0\rangle \\ \frac{dx_j}{dt} = \frac{1}{i\hbar}\left[x_j, H_0\right]\end{gathered} \tag{3.14}$$

H_0 is the time independent Hamiltonian for the molecule. Using Eq. 3.14, Fermi's Golden Rule can be written as

$$\Gamma^{abs}(\omega) = \left[\frac{N_{k\lambda}c}{V}\right]\sum_n \frac{4\pi^2 e^2\hbar\omega}{\hbar c}\left|\vec{d}_{0n} \bullet \vec{\lambda}\right|^2 \delta\left(E_n - E_0 - \hbar\omega\right) \tag{3.15}$$

From Eq. 3.15, the photon absorption rate is directly proportional to the density of photons, the energy of the photon, and the dipole moment of the molecule. The sum is taken over all electron states of the molecule, but the delta-function picks out only those transitions within an energy ħω. The molecular states do not necessarily have to be bound states.

3.3 Electron bonding in a molecule

This thesis will address the bonding of silicon, carbon, and oxygen and use tight binding theory to calculate the electron energy states in the molecule [6]. Silicon and carbon lie in the same column of the Periodic Table, implying that they have the same outer shell atomic orbitals. Electrons occupy two 2s-states and two 2p-states. The probability density and orientation of the *s* and *p* states are shown in Fig. 3.1.

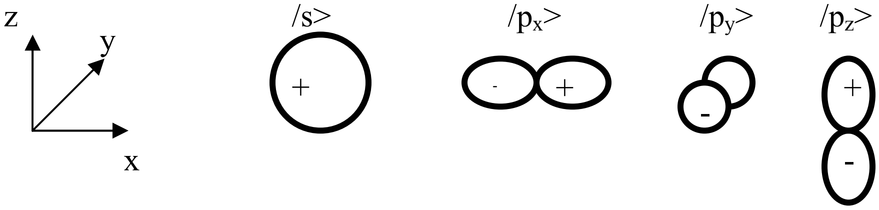

Figure 3.1 Probability density of the *s* and *p* bonding states

From the atomic orbital states shown in Fig. 3.1, the bonding sp^3 hybrid states can be introduced.

$$
\begin{aligned}
|h_1\rangle &= \frac{1}{2}\left(|s\rangle + |p_x\rangle + |p_y\rangle + |p_z\rangle\right) \\
|h_2\rangle &= \frac{1}{2}\left(|s\rangle + |p_x\rangle - |p_y\rangle - |p_z\rangle\right) \\
|h_3\rangle &= \frac{1}{2}\left(|s\rangle - |p_x\rangle + |p_y\rangle - |p_z\rangle\right) \\
|h_4\rangle &= \frac{1}{2}\left(|s\rangle - |p_x\rangle - |p_y\rangle + |p_z\rangle\right)
\end{aligned}
\qquad (3.16)
$$

The hybrid state is directional and is depicted in Fig. 3.2.

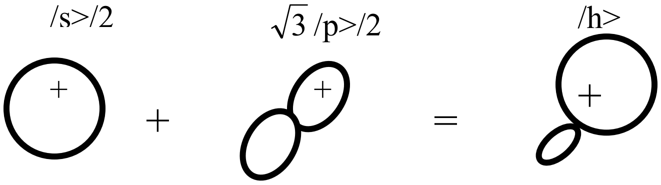

Figure 3.2 The representation of sp^3 hybrid state.

The four orthonormal hybrids given in equation 3.16 form a tetrahedron centered on the atom. The angle between these tetrahedral bonds is 109°28” [6]. The energy for a hybrid state is

$$\varepsilon_h = \frac{\varepsilon_s + 3\varepsilon_p}{4} \qquad (3.17)$$

The bond between carbon and silicon can be expressed entirely in terms of the sp^3 hybrids, Fig. 3.3 and Table 3.1. The energy for two sp^3 bonded atoms can be written as

$$\varepsilon_{bonding} = \frac{\varepsilon_{h1} + \varepsilon_{h2}}{2} - \sqrt{V_2^2 + V_3^2} \qquad (3.18)$$

where ε_{h1} and ε_{h2} are the hybrid energy states for silicon and carbon atoms, respectively. The leading term in Eq. 3.18 is referred to as the promotion energy to form hybrid bonds. After promotion to hybrid bonds, the electron energy levels split into bonding and anti-bonding states. Both bonding and anti-bonding states are proportional to the covalent bond energy, V_2, and the bond polar energy, V_3. A table of both the covalent bond energy and the polar energy for semiconductors and covalently bonded solids can be found in Harrison [6].

The cohesive energy per bond can be calculated from the data given in Table 3.1. The cohesive energy is not the bond-state energy. It is the energy difference between the bound state atoms and free atoms. Often a repulsive term must be added to the energy to approximate the cohesive energy. For semiconductors and metals, the repulsive energy is about half the covalent energy. Using the tight binding model, the Si-C cohesive bond energy is ~-3.31 eV. Compared to the experimental value for the diatomic molecule, -4.69 eV, there is almost a 30% error.

The bonding of silicon and oxygen is not as tidy. Oxygen has six outer shell electrons; two 2s-state electrons and four 2p-state electrons. When bound to silicon, the stoichiometry is SiO_2 and the silicon-oxygen-silicon bond angle is ~ 144°. (The following calculations are taken from Harrison [6].) In order to achieve this stoichiometry and directional bonding, the electronic structure of oxygen is partitioned into a non-bonding π-state, a non-bonding lone pair, and two hybrid bonds with an angle of 144 degrees. The hybrid bonds are comprised of $/s>$, $/p_x>$, and $/p_z>$. The bonding unit is shown is Fig. 3.4. The energy levels in diagram Fig. 3.4 are assigned values in Table 3.2. Again, the cohesive energy can be calculated; but, the repulsive energy is not simply proportional to the covalent energy. It has the form C/d^4, where the constant is 92.3 eV-$Å^4$ and the bond distance is 1.61 Å. In this instance, the cohesive bond energy is -7.25 eV. The experimental value for the diatomic silicon-oxygen bond energy is -8.32 eV, implying a 13% error for the tight binding method.

Table 3.3 contains the bond energy for many of the molecules that will be considered in this thesis. It will help understand the UV cure mechanism. It has already been shown with energy diagrams that the total energy of a silicon dioxide material is significantly lower than the energy of silicon-carbide. In an unstable environment, like UV curing, the molecules will transition to the most stable state possible. From the cohesive energy analysis, it may be assumed that the experimental bond strength is an indicator of system energy. Therefore, Table 3.3 can be used to predict the most probable transitions. The transition rate is given by Fermi's Golden Rule in Eq. 3.12.

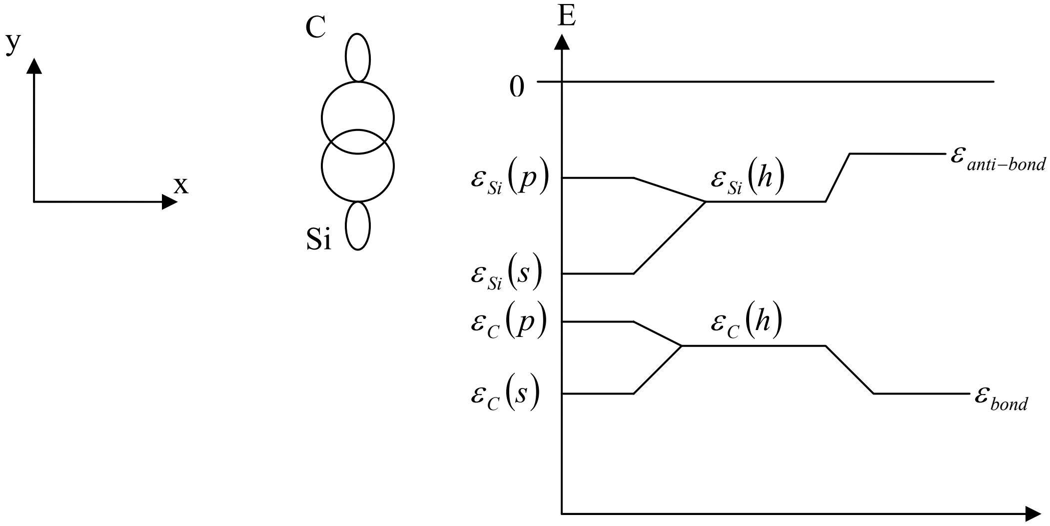

Figure 3.3 Silicon-Carbon binding through hybrid states. An energy level diagram is given at right.

Table 3.1 Tight-binding energy predictions for silicon-carbon

Electron Bond	Energy (eV)
ε_s(Si)	-14.8
ε_p(Si)	-7.6
ε_s(C)	-19.4
ε_p(C)	-11.1
ε_h(Si)	-9.4
ε_h(C)	-13.2
ε_{bond}	-18.5

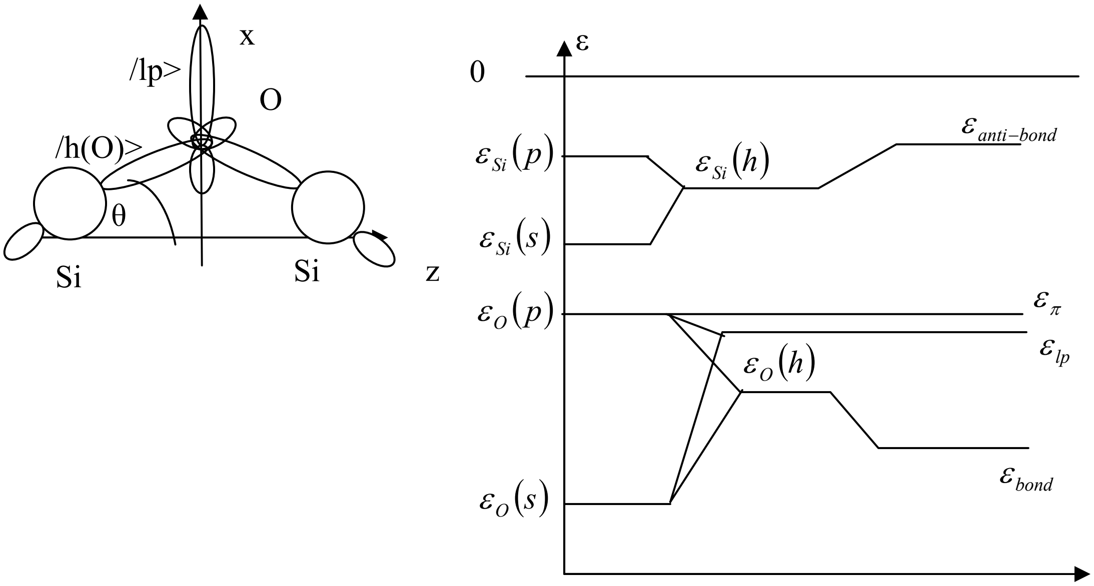

Figure 3.4 Hybrid bond configuration for silicon and oxygen. The energy level diagram is shown on the right. The bond angle θ=18°.

Table 3.2 Tight Binding energy predictions for the silicon dioxide.

Electron Bond	**Energy (eV)**
ε_s(Si)	**-14.8**
ε_p(Si)	**-7.6**
ε_s(O)	**-34.0**
ε_p(O)	**-16.8**
ε_h(Si)	**-9.4**
ε_h(O)	**-24.5**
ε_{lp}(O)	**-18.6**
ε_π(O)	**-16.8**
ε_{bond}	**-29.0**

Table 3.3. Table of the bond energy for different diatomic molecules

Bond	**Energy (eV)**	**Bond**	**Energy (eV)**
C-O	11.2	Si-O	8.3
C-C	6.3	Si-C	4.7
C-H	3.5	Si-H	<3.1
		Si-Si	3.4

3.4 The UV curing method

The application of UV curing to low-k dielectric materials is expected to improve the hardness, modulus, cohesive strength, adhesion, and dielectric constant. It is difficult to conceive how all of these improvements can occur simultaneously, but some advances have been made by tailoring the cure method. Important parameters in curing are the UV spectral intensity, temperature, time, pressure, and background gas. In this section, the effect of spectral intensity and temperature will be discussed. To the author's knowledge, only one paper has been published about the specific engineering of UV curing of low-k dielectrics. That paper is by Berry, *et al*. from Axcelis Technologies and this section will discuss some of their results [7].

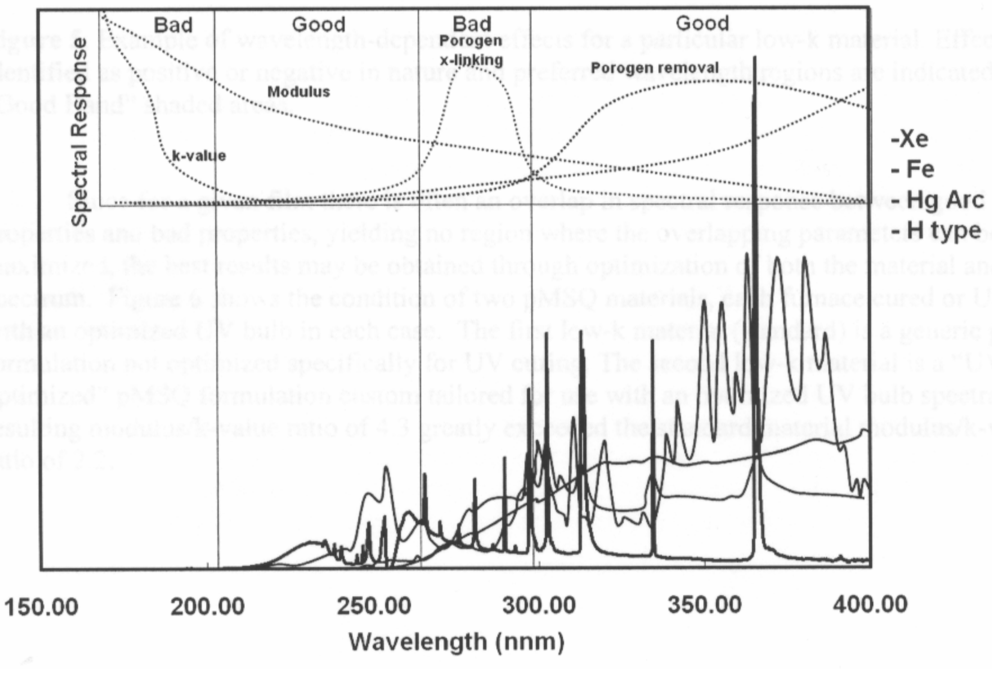

Figure 3.5 Spectral response of k-value, modulus, porogen removal, and porogen crosslinking of a hypothetical low-k overlayed on the spectrums of commercially available UV bulbs—Xe arc, Hg arc, and electrodeless Fe and H bulbs [7].

The spectral response for a hypothetical low-k is given in Fig. 3.5, overlayed on the spectrum of four different UV bulbs. The material parameters charted in the spectral response are k-value, modulus, porogen removal, and porogen crosslinking. There are two "bad" regions and two "good" regions. The "bad" region at lowest wavelength or highest energy corresponds to an increase in k-value and is unsuitable. The energy range for this "bad" region is 8.3 to 6.2 eV. The second "bad" region lies between 250 and 300 nm and corresponds to 4.97 to 4.14 eV. In this energy range, porogen crosslinking occurs and, recalling Table 3.3, this energy range corresponds to the Si-C bond. The first "good" region lies between 200 and 250 nm or 6.21 and 4.97 eV. In this region, the k-value is minimized. The other "good" region lies between 300 and 400 nm or 4.14 and 3.11 eV, where the porogen is removed. The k-value also tends to increase in this region. Interestingly, the modulus tends to increase for the entire energy range. The ability to tune the bulb to include only the "good" regions, while excluding the "bad" regions, is limited. If the other material parameters-- such as adhesion, cohesive strength, and strength of the dielectric constant, are included in the tuning process, the ability to match a bulb becomes very difficult.

While tuning the spectrum of a UV bulb is important, the cure temperature also affects the UV performance. Berry *et al*. [7] have shown that the UV cure crosslink efficiency, shown in Fig. 3.6, increases exponentially with temperature. The efficiency is defined to be the inverse of the time to reach the same degree of crosslinking as at 400°C cure. A simple model of the UV cure process is that, after the molecules absorb a photon and breaks its bond, the molecules must have sufficient mobility to re-arrange themselves to form new bonds. Iacopi *et al.* [8] have also shown the effectiveness of UV cure with temperature. They measured the elastic modulus of a low-k ~3.0 material for "no UV cure" and 300s of UV cure at room temperature, 350° C and 400° C. They found that the modulus increased with temperature by 0%, 15%, and 40%, respectively.

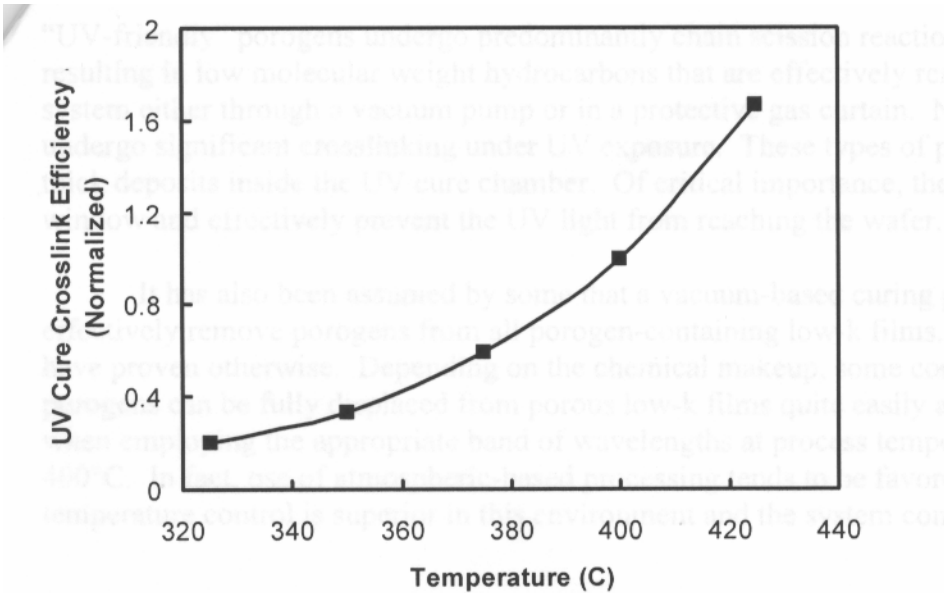

Figur 3.6 Efficiency of UV curing crosslinking of a p-MSQ material vs. cure temperature [7].

3.5 Summary

This chapter introduced the classical and quantized electro-magnetic fields. It was shown that the quantized electro-magnetic field was comprised of any number of photons with energy ħω, where a sum is taken over the photon energies. After quantizing the EM field, Fermi's Golden Rule was introduced. In order to understand the electron bonding states in the molecule used in Fermi's Golden Rule, the results of tight binding theory were applied to the molecular structure of silicon-carbon and silicon dioxide following the approach of Harrison. Hybrid bonding of the atoms was introduced and the energy level diagrams calculated. From the tight bonding calculations, the binding energies for the molecules were derived. These results roughly matched the energy of the diatomic molecules verifying the understanding of the bonding process. Finally, the UV cure method was introduced and the tuning of the UV spectrum was discussed.

Chapter 4 Solid mechanics and fracture mechanics in a bi-material system

In Chapter 4, the mechanics theory that is needed to analyze a crack at a bi-material interface is developed. The chapter begins with an overview of solid mechanics, introducing the theory of elasticity for plane strain and the symmetry principles at an interface. The majority of this chapter will be dedicated to fracture mechanics. The topics in fracture that will be discussed are cohesive failure, failure at an interface, inelastic processes at the crack tip, and sub-critical crack growth. The fracture modes, Griffith criterion, stress intensity factors, and the J-integral will be introduced for a crack in a single bulk material. By introducing an interface, the elastic solution for a single material will be reformulated. New stress intensity factors for an interface will be introduced and a non-trivial mode-mix is presented. Also, an adhesive joint is studied to predict the crack location and stability. The inelastic processes discussed are plastic deformation and asperity locking. Finally, the theory of stress corrosion, as applied to sub-critical fracture, is presented.

4.1 Elements of solid mechanics

4.1.1. Plane strain elastic theory

The necessary equations for the description of a deformed body can be written in four equations. The equilibrium condition is

$$\sigma_{ij,i} + f_i = 0 \qquad (4.1)$$

where σ_{ij} is the stress field of the body and f_i is a component of a body force such as gravity. (The Einstein summation rule is used and will be used for the remainder of this thesis, unless otherwise specified.) The kinematic relations for a deformation field $\underline{u}$ are

$$\varepsilon_{ij} = \frac{1}{2}\left(u_{i,j} + u_{j,i}\right) \qquad (4.2)$$

where ε_{ij} is the infinitesimal strain tensor. In order to uniquely solve for the displacement fields given the strains, the compatability conditions must be met.

$$\varepsilon_{ij,kl} + \varepsilon_{kl,ij} = \varepsilon_{ik,jl} + \varepsilon_{jl,ik} \qquad (4.3)$$

There are 81 possible combinations of Eq. 4.3, but only six possibilities are distinct. The constitutive law for isotropic elasticity is

$$\varepsilon_{ij} = \frac{1}{E}\left[(1+\nu)\sigma_{ij} - \nu\delta_{ij}\sigma_{kk}\right] \qquad (4.4)$$

where E is the Young's Modulus and v is Poisson's Ratio.

For the purposes of this thesis, we do not need the full set of elastic equations. Great simplifications can be made by assuming the conditions of plane strain,

$$\varepsilon_{xz} = \varepsilon_{yz} = \varepsilon_{zz} = 0 \qquad (4.5)$$

where the directions x, y, and z are labeled in Fig. 4.1. The plane strain condition is usually met when the in-plane thickness (x-direction) is much greater than the out-of-plane thickness (z-direction) and all tractions are functions of the x-y plane.

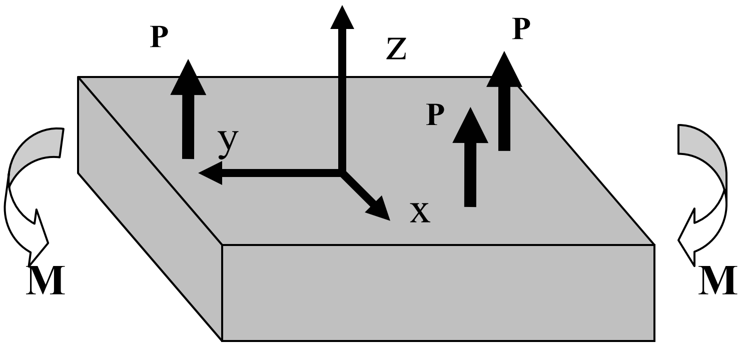

Figure 4.1 Plane strain geometry with surface tractions and couples.

In the absence of body forces and given plane strain conditions, the equilibrium equations produce two equations,

$$\begin{aligned} \sigma_{xx,x} + \sigma_{xy,y} &= 0 \\ \sigma_{xy,x} + \sigma_{yy,y} &= 0 \end{aligned} \tag{4.6}$$

The stresses can be represented by a single function, often referred to as the Airy stress function.

$$\begin{aligned} \sigma_{xx} &= \phi,_{yy} \\ \sigma_{yy} &= \phi,_{xx} \\ \sigma_{xy} &= -\phi,_{xy} \end{aligned} \tag{4.7}$$

The Airy stress function can satisfy equation 4.6 and the compatibility equations if it is bi-harmonic. That is

$$\nabla^4 \phi = 0 \tag{4.8}$$

4.1.2 Symmetry principles at an interface

The introduction of an interface between two different materials complicates the elastic solution. It is no longer possible to apply tensile stress without also producing shear stress. By Newton's Third Law, the total tractions on the surface are zero, as illustrated in Figure 4.2. Also, material continuity requires that the displacement fields be continuous at the interface.

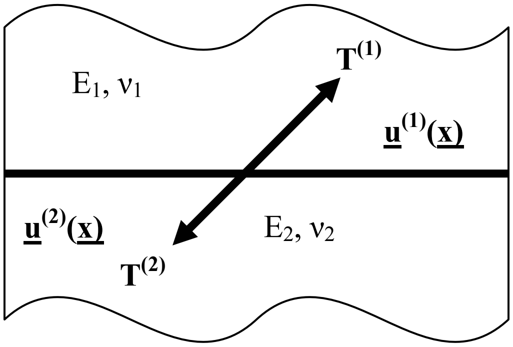

Figure 4.2. Bi-material system

The symmetry requirements at the interface are

$$\begin{aligned} \sigma_{12}^{(1)} &= \sigma_{12}^{(2)} \\ \sigma_{22}^{(1)} &= \sigma_{22}^{(2)} \\ u_i^{(1)}(\vec{x}) &= u_i^{(2)}(\vec{x}) \end{aligned} \tag{4.9}$$

Dundurs found in 1969 that many elastic solutions for the bi-material plane problems only require two non-dimensional combinations of the elastic moduli [1]. The parameters are

$$\begin{aligned} \alpha &= \frac{\mu_1(\kappa_2+1)-\mu_2(\kappa_1+1)}{\mu_1(\kappa_2+1)+\mu_2(\kappa_1+1)} \\ \beta &= \frac{\mu_1(\kappa_2-1)-\mu_2(\kappa_1-1)}{\mu_1(\kappa_2+1)+\mu_2(\kappa_1+1)} \end{aligned} \tag{4.10}$$

where μ_i is the shear modulus and $\kappa_i=3-4\nu_i$ for plane strain. The α parameter is a measure of the mismatch of the tensile moduli across the interface; while the parameter β is a measure of the mismatch between the in-plane bulk moduli.

4.2 Elements of fracture mechanics

4.2.1 Fracture and cohesive failure

The cohesive fracture of a material may occur by three normal modes. Fracture Modes I, II, and III are described in Fig. 4.3. Mode I denotes tensile stress at the crack tip; Mode II denotes shear loading at the crack tip; and Mode III denotes tearing loads.

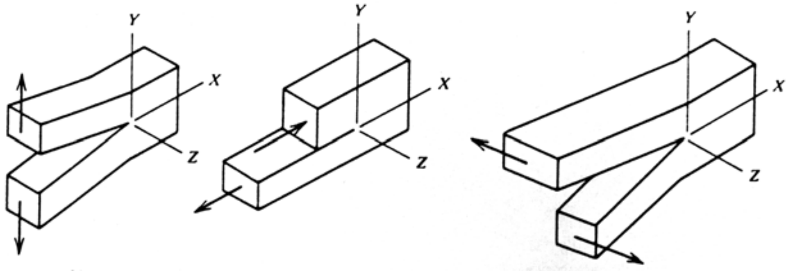

Mode I
Opening (tensile)

Mode II
Sliding (Shear)

Mode III
Tearing

Figure 4.3 Illustration of Mode I, II, and III cracking.

4.2.2 The Griffith criterion and the energy release rate

Griffith introduced a thermodynamic explanation for the advancement of cracks in brittle materials [2]. He suggested that the total energy, E, of the system was the sum of the potential energy, Π, and the surface energy, S, created during cleavage. Let Π and S be defined as the energies per unit width.

$$dE = d\Pi + dS = 0 \qquad (4.11)$$

The surface energy per unit area is a material constant and is denoted by γ. The increment of surface energy is then, $dS=2\gamma da$ where da is the increase in crack length. The fracture produces two faces and therefore the energy for a crack to advance must be twice the energy for one surface. Let Γ be the fracture toughness of the material and therefore, $\Gamma = {dS}/{da}$. Likewise, the strain-energy release rate or driving force for crack propagation is given in Eq. 4.12.

$$G = -\frac{d\Pi}{da} \qquad (4.12)$$

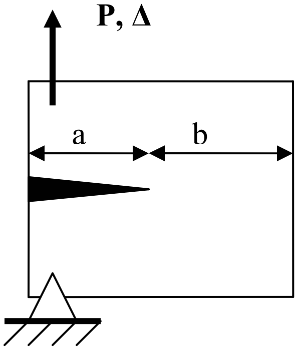

Figure 4.4 A loaded crack system

G is a function of the loading potential *Π*. Using an example from Kanninen and Popelar [3], the potential energy *Π* can be calculated and the effect of boundary conditions explored. The potential energy of deformation for an applied load, *P,* acting through a displacement, Δ, is equal to the difference in the strain energy and the work of loading the sample.

$$\Pi = U - P\Delta \qquad (4.13)$$

where *U* is the strain energy and *PΔ* is the work of loading. The strain energy is found to be $U = \frac{1}{2} P\Delta$. Eq. 4.13 is reduced to

$$\Pi = -\frac{1}{2} P\Delta \qquad (4.14)$$

The material compliance, *C*, can be used to relate the displacement to the load, $\Delta = CP$. The energy release rate from Eq. 4.12 is then

$$G = \frac{P^2}{2}\frac{dC}{da} \qquad (4.15)$$

If the load point is fixed at a prescribed displacement, the potential energy for deformation changes to $\Pi = \frac{P\Delta}{2}$. The strain-energy release rate becomes

$$G = -\frac{1}{2}\Delta\left(\frac{dP}{da}\right)_{\Delta} \qquad (4.16)$$

4.2.3 The elastic solution for the fracture of a brittle material

A crack in an elastic body can be considered a wedge in the material as shown in Fig. 4.5. Given the conditions of plane strain, the solution to this problem was given by Williams. First, recall that the plane strain solution must satisfy the bi-harmonic equation

$$\nabla^4 \Phi = 0 \tag{4.17}$$

The solution proposed by Williams [17] was that

$$\begin{gathered} \Phi = r^{\lambda+1} f(\alpha,\lambda) \\ f(\alpha,\lambda) = c_1 \cdot \sin(\lambda+1)\alpha + c_2 \cdot \cos(\lambda+1)\alpha + c_3 \cdot \sin(\lambda-1)\alpha + c_4 \cdot \cos(\lambda-1)\alpha \end{gathered} \tag{4.18}$$

The stresses in polar coordinates can be expressed in terms of the Airy stress function, Φ.

$$\begin{aligned} \sigma_{rr} &= r^{\lambda-1}\left[f''(\alpha,\lambda) + (\lambda+1)\cdot f(\alpha,\lambda)\right] \\ \sigma_{\theta\theta} &= r^{\lambda-1}\left[\lambda\cdot(\lambda+1) f(\alpha,\lambda)\right] \\ \sigma_{r\theta} &= r^{\lambda-1}\left[-\lambda f'(\alpha,\lambda)\right] \end{aligned} \tag{4.19}$$

Let the crack surfaces be traction free, then

$$\begin{gathered} \sigma_{\theta\theta}(\alpha=0) = \sigma_{\theta\theta}(\alpha=2\pi) = \sigma_{r\theta}(\alpha=0) = \sigma_{r\theta}(\alpha=2\pi) = 0 \\ \textbf{or} \\ f(0,\lambda) = f(2\pi,\lambda) = f'(0,\lambda) = f''(2\pi,\lambda) = 0 \end{gathered} \tag{4.20}$$

These boundary conditions can be satisfied if $\sin(2\pi\lambda) = 0$. Therefore, λ can take any half integer value, $\lambda = \mathbf{1/2, 1, 3/2, 2, 5/2, ...}$

After solving some algebra, the Airy stress function can be written as

$$\Phi = \sum_n r^{n/2+1}\left[c_3\left\{\sin\left(n/2-1\right)\alpha - \frac{n-2}{n+2}\sin\left(n/2+1\right)\alpha\right\} + c_4\left\{\cos\left(n/2-1\right)\alpha - \cos\left(n/2+1\right)\alpha\right\}\right]$$

(4.21)

Making the substitution of $\theta = \alpha - \pi$, the first term in the Airy stress function is

$$\Phi = r^{3/2}\left[s_1\left\{-\cos\left(\frac{\theta}{2}\right) - \frac{1}{3}\cos\left(\frac{3\theta}{2}\right)\right\} + t_1\left\{-\sin\left(\frac{\theta}{2}\right) - \sin\left(\frac{3\theta}{2}\right)\right\}\right] \qquad (4.22)$$

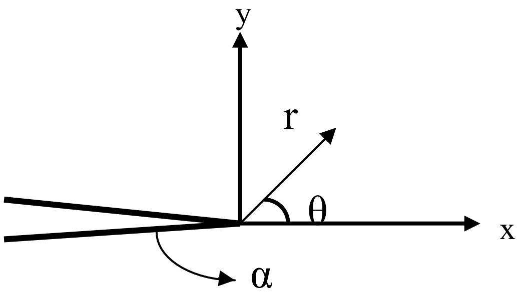

Figure 4.5 Crack orientation in polar coordinates

The constants in Eq. 4.22 can be directly related to the stress intensity factors.

$$s_1 = -\frac{K_I}{\sqrt{2\pi}}$$
$$t_1 = \frac{K_{II}}{\sqrt{2\pi}} \qquad (4.23)$$

The full elastic solution for Mode I and Mode II fracture are given in Eqs. 4.24 and 4.25.

Mode I

$$\begin{bmatrix}\sigma_{11}\\ \sigma_{12}\\ \sigma_{22}\end{bmatrix}=\frac{K_I}{\sqrt{2\pi\cdot r}}\cos\left(\theta/2\right)\begin{bmatrix}1-\sin\left(\theta/2\right)\sin(3\theta/2)\\ \sin(\theta/2)\cos(3\theta/2)\\ 1+\sin\left(\theta/2\right)\sin(3\theta/2)\end{bmatrix}$$

(4.24)

$$\begin{bmatrix}u_1\\ u_2\end{bmatrix}=\frac{K_I}{2\mu}\left(\frac{r}{2\pi}\right)^{1/2}\begin{bmatrix}\cos(\theta/2)\left\{\kappa-1+2\sin^2(\theta/2)\right\}\\ \sin(\theta/2)\left\{\kappa+1-2\cos^2(\theta/2)\right\}\end{bmatrix}$$

Mode II

$$\begin{bmatrix}\sigma_{11}\\ \sigma_{12}\\ \sigma_{22}\end{bmatrix}=\frac{K_{II}}{\sqrt{2\pi\cdot r}}\begin{bmatrix}-\sin\left(\theta/2\right)\left\{2+\cos(\theta/2)\cos(3\theta/2\right\}\\ \cos(\theta/2)\left\{1-\sin(\theta/2)\sin(3\theta/2)\right\}\\ \sin\left(\theta/2\right)\cos(\theta/2)\cos(3\theta/2)\end{bmatrix}$$

(4.25)

$$\begin{bmatrix}u_1\\ u_2\end{bmatrix}=\frac{K_{II}}{2\mu}\left(\frac{r}{2\pi}\right)^{1/2}\begin{bmatrix}\sin(\theta/2)\left\{\kappa+1+2\cos^2(\theta/2)\right\}\\ -\cos(\theta/2)\left\{\kappa-1-2\sin^2(\theta/2)\right\}\end{bmatrix}$$

where κ is 3-4ν. The leading coefficient for each mode is called the stress intensity factor. K_I and K_{II} are related to the stress fields by the following limiting processes.

$$\begin{aligned}K_I&=\lim_{r\to 0}\left(\left[2\pi\cdot r\right]^{1/2}\sigma_{22}\big|_{\theta=0}\right)\\ K_{II}&=\lim_{r\to 0}\left(\left[2\pi\cdot r\right]^{1/2}\sigma_{12}\big|_{\theta=0}\right)\end{aligned}\tag{4.26}$$

The stress intensity factors are functions of the applied load and sample geometry. The stress intensity factors may often depend on the crack length.

From the stress intensity factors, the mode-mix or phase angle may be defined [4]. The mode-mix indicates the ratio of shear to tensile stresses at the crack tip. Let ψ be the phase angle.

$$\psi = \tan^{-1}\left(\frac{K_{II}}{K_I}\right) \tag{4.27}$$

In Fig. 4.6, the strain-energy release rate increases with mode-mix. In general, the intrinsic fracture toughness is less than the measured fracture toughness. The intrinsic fracture toughness is the resistance to fracture by the creation of two new surfaces. In other words, it is the surface energy term in the Griffith criterion. Inelastic processes account for the difference, such as plasticity and asperity [5].

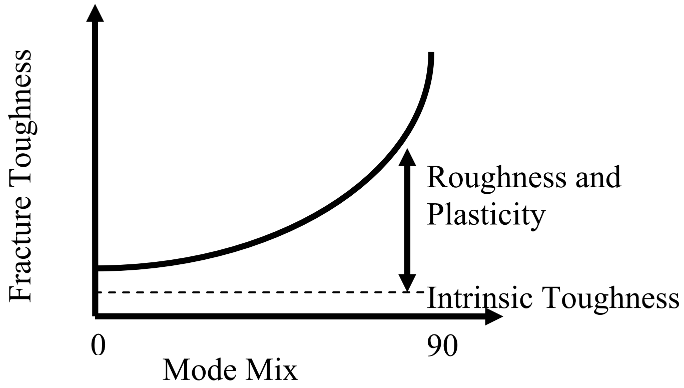

Figure 4.6 The fracture toughness as a function of Mode-mix.

In 1957, G. R. Irwin found a relationship between the stress-intensity factors and the stress energy release rate [3]. The relation is a simple quadratic sum of the stress-intensity factors. For Mode I and Mode II in plane strain,

$$G = \frac{\left(1-\nu^2\right)}{E}\left(K_I^2 + K_{II}^2\right) \tag{4.28}$$

4.2.4 The J-integral

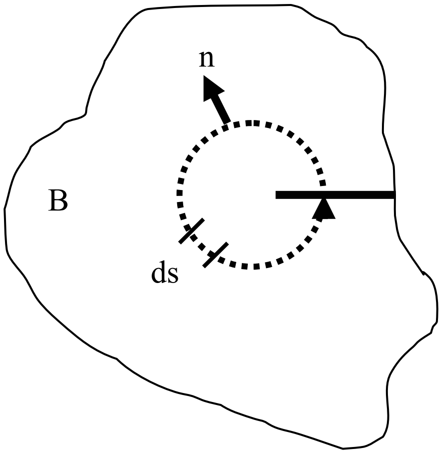

Figure 4.7 Contour for J-integral evaluation

For an elastic body, *B*, in a state of plane strain, the *J*-integral, discovered by J.R. Rice [6], is defined as

$$\begin{aligned} J &= \int_{\partial S} \left(W n_1 - \sigma_{jk} n_k u_{j,1}\right) ds \\ W &= \int_0^{\varepsilon} \sigma_{ij} \cdot d\varepsilon_{ij} \end{aligned} \tag{4.29}$$

where W is the strain energy, σ_{jk} is the stress field, u_j is the displacement field, and n_j is the outward normal to the boundary ∂S. The *J*-integral is calculated in the counter-clockwise direction. For any closed contour, the *J*-integral is zero. Consider the path integral around the crack tip in Fig. 4.8. A closed contour is represented by the curve ABCDEF, where path Γ_1 is path ABC and path Γ_2 is DEF. The contour path along CD and FA lies on the cracked edges and, therefore, does not contribute to the J-integral. The J-integral can now be written as

$$J = \int_{\Gamma_1} \left(Wn_1 - \sigma_{jk} n_k u_{j,1}\right) + \int_{\Gamma_2} \left(Wn_1 - \sigma_{jk} n_k u_{j,1}\right) = J_{\Gamma 1} + J_{\Gamma 2} = 0 \tag{4.30}$$

Consequently, it is found that $J_{\Gamma 1} = -J_{\Gamma 2}$ (the negative sign reverses the direction of integration to counter clock-wise) or the J integral is the same for any path that encloses the crack tip.

Rice found that the J-integral, for any path enclosing the crack tip, had a finite value equal to the change in potential energy with crack tip advancement.

$$J = -\frac{d\Pi}{da} = G \tag{4.31}$$

Therefore, the *J*-integral is equal to the strain-energy release rate.

The J-integral can be calculated in ABAQUS 6.6. By defining a crack in the Interaction Module of ABAQUS 6.6, the J-integral can be calculated from a contour integral in the History Output of the Step Module. In general, it is best to calculate the J-integral for multiple contours, at least 5 to 10, in order to observe convergence of the calculation. For more information see the ABAQUS Documentation, key word *contour integral*.

The J-integral can be used in both elastic and plastic yielding bodies.

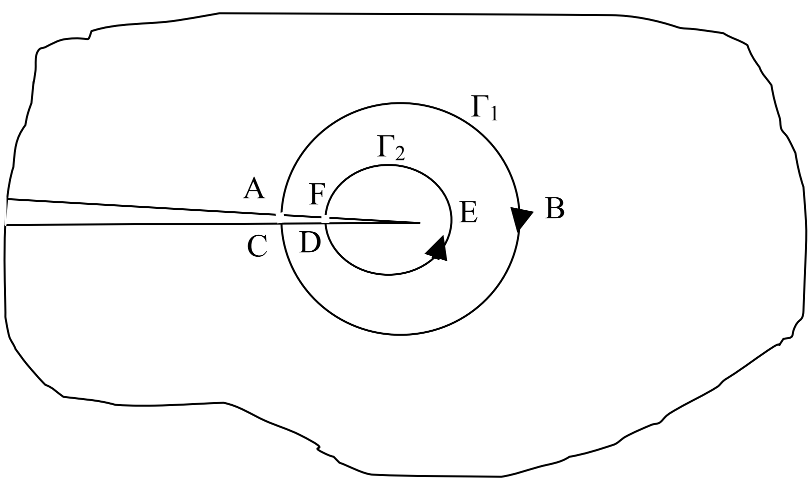

Figure 4.8 Closed Contour for J-integral analysis.

4.3 The Introduction of an interface

4.3.1 The stress-intensity factors

The introduction of an interface changes the characteristics of the stress-intensity factors. It is no longer possible to distinctly separate $\sigma_{\alpha\beta}$ into components K_I and K_{II} [4, 7]. The interface introduces a length scale into the problem whose influence is determined by the oscillatory parameter

$$\varepsilon = \frac{1}{2\pi}\ln\left(\frac{1-\beta}{1+\beta}\right) \tag{4.32}$$

The parameter β in Eq. 4.32 is a Dundurs parameter from Eq. 4.10. Consider the stress field at the interface ahead of the crack. The normalized stress fields can be written as [4, 7]

$$\sigma_{22} + i\sigma_{12} = \frac{\left(K_1 + iK_2\right)}{\sqrt{2\pi \cdot r}} r^{i\varepsilon} \tag{4.33}$$

The stress-intensity factors are now labeled with Arabic numerals, not Roman, and the oscillatory parameter guarantees that any change in the tensile stress also leads to changes in the shear stress. Displacements behind the crack tip (θ=π) are also dependent on a length scale [4, 7].

$$\begin{gathered}\delta_1 + i\delta_2 = \frac{8}{\left(1 + 2i\varepsilon\right)\cosh(\pi\varepsilon)} \frac{(K_1 + iK_2)}{E^*} \cdot \sqrt{\frac{r}{2\pi}} \cdot r^{i\varepsilon} \\ \frac{1}{E^*} = \frac{1}{2}\left(\frac{1-\nu_1^2}{E_1} + \frac{1-\nu_2^2}{E_2}\right)\end{gathered} \tag{4.34}$$

From equation 4.34 the influence of the oscillatory parameter can be appreciated. For a finite distance behind the crack tip, Eq. 4.28 predicts that the interface displacement will oscillate and the two surfaces interpenetrate.

The strain-energy release rate can still be defined in terms of the stress-intensity factors [8].

$$G = \left(\frac{\left(\kappa_1 + 1\right)\mu_2 + \left(\kappa_2 + 1\right)\mu_1}{\mu_1 \mu_2}\right) \frac{K\,\overline{K}}{16\cosh^2\left(\pi\varepsilon\right)} \tag{4.35}$$

where $\kappa_i = 3 - 4\nu_i$ and μ_i is the shear modulus.

4.3.2 A new mode-mix

With the introduction of an interface, the mode-mix is dependent on a reference length scale, *l*, [8].

$$\psi = \tan^{-1}\left(\frac{\mathrm{Im}\left(Kl^{i\varepsilon}\right)}{\mathrm{Re}\left(Kl^{i\varepsilon}\right)}\right) = \tan^{-1}\left[\left(\frac{\sigma_{12}}{\sigma_{22}}\right)_{r=l}\right] \tag{4.36}$$

The length scale, *l*, is an arbitrary distance. It can be the plastic zone size, specimen geometric length, the length of the crack, etc. A change in length scale can be defined by the following transformation

$$\psi_2 = \psi_1 + \varepsilon \ln\left({}^{l_2}\!/_{l_1} \right) \tag{4.37}$$

where l_1 is associated with ψ_1 and l_2 is associated with ψ_2.

4.3.3 The J-integral for a bi-material interface

Unlike the stress-intensity factors, the J-integral does not need to be redefined for a bi-material system. Smelser and Gurtin have shown that the J-integral, as defined in 4.29, is applicable to any system with n-layers when the interfaces are parallel to the crack plane [8].

Consider the general conservation law expressed by the J-integral.

$$\begin{aligned} &\int_{\partial R} \left(W n_i - \sigma_{jk} n_k u_{j,i} \right) ds = 0 \\ &W = \int \sigma_{ij} \, d\varepsilon_{ij} \end{aligned} \qquad (4.38)$$

where the boundary ∂R lies entirely within a homogeneous linear elastic body. W is the strain energy, σ_{ij} is the stress, u_j is the displacement, and n_j is the outward unit normal to the boundary ∂R. Now consider a bi-material system as depicted in Fig. 4.9, where the interface lies along the x_1 direction. The region of integration is now $\partial R = \partial R_1 + \partial R_2$ and the interface joining these two regions is l. The conservation law is now written as

$$\int_{\partial R} \left(W n_i - \sigma_{jk} n_k u_{j,i} \right) ds - \int_{l} \left(\left[W^{(2)} - W^{(1)} \right] \delta_{i2} - \sigma_{k2} \left[u_{k,i}^{(2)} - u_{k,i}^{(1)} \right] \right) ds = 0 \qquad (4.39)$$

where the superscripts denote the body bounding the interface. Note that if $i=1$ in Eq. 4.39, the second integral vanishes and the first integral becomes the familiar J-integral of Eq. 4.29. This proves that the J-integral can be extended to a bi-material system. Actually, by successive applications, the J-integral can be extended to any number of layers as long where the interface is in the x_1 direction.

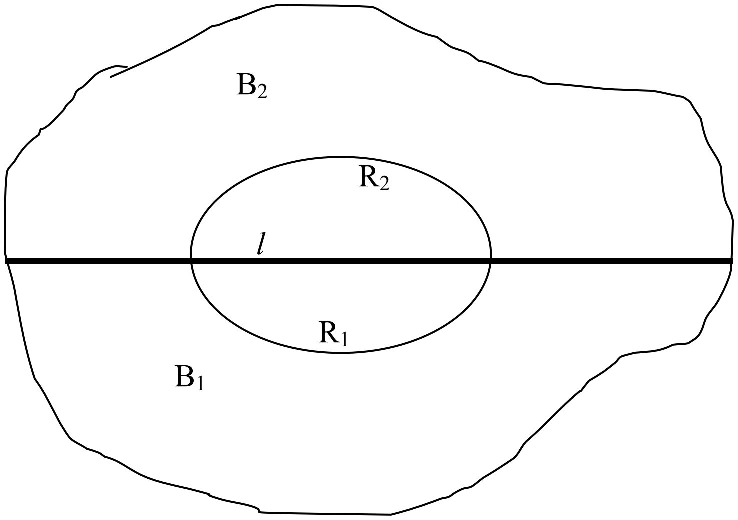

Figure 4.9 An interface between two linear elastic bodies.

4.3.4 Crack location and stability

A crack that advances in an isotropic homogeneous brittle solid chooses a path that minimizes the mode-mix, i.e. the local Mode II component is zero. It is worth emphasizing that the global mode-mix and the local mode-mix for a sample are not necessarily the same. In this section, the crack path will be determined by examining the local mode-mix. The theory, presented here, is that of Fleck, Hutchinson, and Suo [9].

The basic problem is shown in Fig. 4.10 for a crack advancing within an adhesive layer bonding two identical monolithic substrates. There are four load quantities in this example. First, the asymptotic loads and specimen geometry are characterized by K_I^{∞} and K_{II}^{∞}. These asymptotic stress intensity factors represent the flawed sample without the adhesive layer. Second, a residual stress, σ_0, may exist due to thermal mismatch or similar sources. Finally, an in-plane stress, T^{∞}, acts parallel to the crack plane. Normalized stresses ahead of the crack tip (θ=0) in the adhesive are

$$\begin{bmatrix} \sigma_{xx} & \sigma_{xy} \\ \sigma_{xy} & \sigma_{yy} \end{bmatrix} = \frac{K_I}{\sqrt{2\pi \cdot r}} \begin{bmatrix} 1 & 0 \\ 0 & 1 \end{bmatrix} + \frac{K_{II}}{\sqrt{2\pi \cdot r}} \begin{bmatrix} 0 & 1 \\ 1 & 0 \end{bmatrix} + \begin{bmatrix} T & 0 \\ 0 & 0 \end{bmatrix} + O\left(\sqrt{r}\right) \qquad (4.40)$$

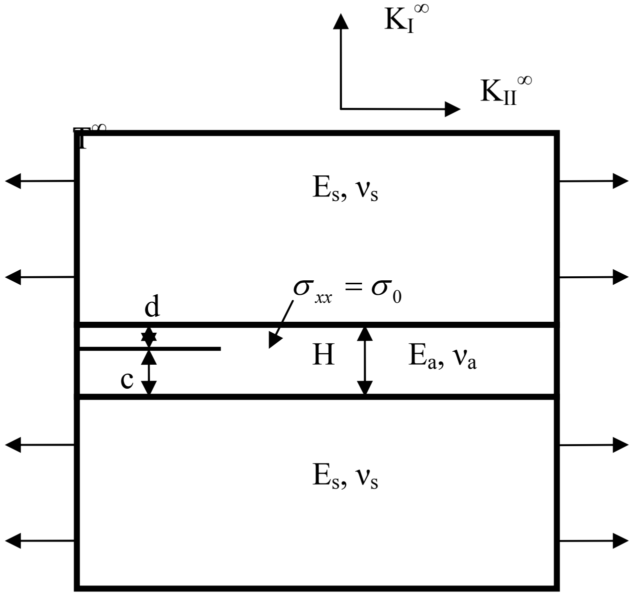

Figure 4.10 The elastic problem for crack location and stability

K_I and K_{II} are the local stress intensity factors. The stresses σ^0 and T^{∞} do not contribute to the stress intensity factors and are therefore separated into the third term of Eq. 4.40. The remote stress-intensity factors can be related to the local ones by taking two different contours for the J-integral. The first contour would be local; and the second global. The result is

$$G = J = \frac{\left(1-\nu_a^2\right)}{E_a}\left(K_I^2 + K_{II}^2\right) = \frac{\left(1-\nu_s^2\right)}{E_s}\left(\left(K_I^\infty\right)^2 + \left(K_{II}^\infty\right)^2\right) \qquad (4.41)$$

An algebraic manipulation reduces Eq. 4.33 to

$$K_I + iK_{II} = \left(\frac{1-\alpha}{1+\alpha}\right)^{1/2} \left(K_I^\infty + iK_{II}^\infty\right)\cdot e^{i\varphi} \qquad (4.42)$$

where α is a Dundurs parameter and the phase angle shift, φ, is a function of the geometry of the adhesive layer and the both Dundurs parameters.

$$\varphi = \varepsilon \ln\left(\frac{H-c}{c}\right) + 2\left(\frac{c}{H} - \frac{1}{2}\right)\left(\varphi_H(\alpha,\beta) + \omega(\alpha,\beta)\right) \qquad (4.43)$$

The geometric variables can be found in Fig. 4.10. The two new function of the Dundurs parameters, φ_H and ω, have been tabulated in Hutchinson, Mear, and Rice [10] and Hutchinson and Suo [4], respectively.

Equations 4.42 and 4.43 can be combined to find the location of the crack within the adhesive layer. If K^∞ has a phase angle of ψ, the location of the crack is determined by $\psi + \varphi = 0$.

Table 4.1 Stability of cracks in an adhesive layer.

T-stress	**Mode II Gradient**	**Crack Pattern**
T<0	$\frac{\partial K_{II}}{\partial c}>0$	Stable center line crack
T>0	$\frac{\partial K_{II}}{\partial c}>0$	Wavy around center line
T<0	$\frac{\partial K_{II}}{\partial c}<0$	Gradual approach to interface
T>0	$\frac{\partial K_{II}}{\partial c}<0$	Approaches interface at large angle

The stability of a crack is determined by the T-stress and the gradient of the local K_{II}. Consider a sample remotely loaded in Mode I, $K_{II}^{\infty}=0$. Table 4.1 indicates the character of the crack for different load conditions.

4.3.5 Inelastic processes at the crack tip

In this section, we will examine inelastic processes that contribute to the fracture toughness. The first process is plasticity and the second is asperity or surface roughness.

4.3.5.1 Plasticity & the Prandtl-Reuss equations

In this section, two possible constitutive relationships for plastic yielding, seen in Fig. 4.11, will be discussed. Both constitutive relationships will be used later in calculating the contributions to the fracture toughness, using a Finite Element Program.

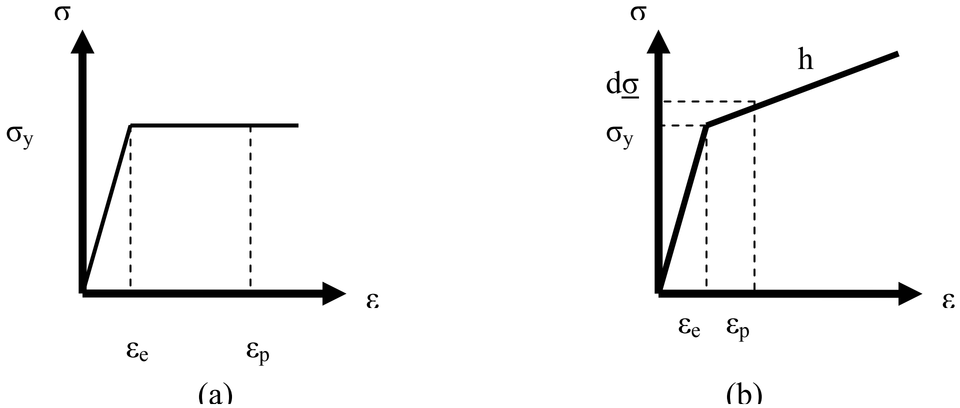

Figure 4.11 Constitutive relationship for plastic yielding

a) elastic-perfect plastic and b) strain hardening.

Figure 4.11.a represents elastic-perfect plastic deformation; while Figure 4.11.b represents strain hardening [11]. The Von Mises stress is given in Eq. 4.44.

$$\bar{\sigma} = \left(\frac{3}{2} s_{ij} s_{ij} \right)^{1/2}$$

$$s_{ij} = \sigma_{ij} - \frac{1}{3} \sigma_{kk} \delta_{ij} \tag{4.44}$$

where s_{ij} is the deviatoric stress tensor. From the Von Mises stress, the yield criterion can be specified by letting $\bar{\sigma} = \sigma_y$, where σ_y is the yield stress. For elastic-perfect plastic yielding, the Von Mises yield stress is a constant; while, for strain hardening, the Mises stress increases with plastic yielding. The Prandtl-Reuss equations, an incremental theory of plasticity, can be written as [11]

$$d\varepsilon_{ij} = \frac{1+\nu}{E} d\sigma_{ij} - \frac{\nu}{E}\delta_{ij} d\sigma_{kk} + \frac{3}{2}\frac{s_{ij}}{\overline{\sigma}} d\overline{\varepsilon}^{p} \qquad \text{a)}$$

or (4.45)

$$d\varepsilon_{ij} = \frac{1+\nu}{E} d\sigma_{ij} - \frac{\nu}{E}\delta_{ij} d\sigma_{kk} + \frac{3}{2}\frac{s_{ij}}{\overline{\sigma} h} d\overline{\sigma} \qquad \text{b)}$$

where h is the slope defined in Fig. 4.11. The effective plastic strain increment, $d\overline{\varepsilon}^{p}$, is defined by

$$d\overline{\varepsilon}^{p} = \left(\frac{2}{3} d\varepsilon_{ij}{}^{p} d\varepsilon_{ij}{}^{p} \right)^{1/2} \qquad (4.46)$$

Later, the J-integral will be used to calculate the increase in fracture toughness with plastic yielding. The strain hardening constitutive relation will be used.

4.3.5.2 Asperity contact

Asperity contact behind the crack tip acts to shield the crack from the applied loading. When asperities come into contact, a frictional force develops due to normal tractions. The frictional force must be overcome to separate the two surfaces. The degree of shielding from asperity interaction depends on the contact zone size, the amplitude and wavelength of the surface roughness, and the coefficient of friction. Unfortunately, the coefficient of friction is seldom known; nor is the scale of the surface roughness easily defined. Evans and Hutchinson [12] have solved an idealized model where the surface morphology is simple, having one roughness and wavelength. In their model, they removed the frictional force and found that the effectiveness of the shielding is gauged by a parameter χ.

$$\chi = \frac{EH}{\Gamma_0} \tag{4.47}$$

E is Young's Modulus; H is the amplitude of the roughness; and Γ_0 is the fracture toughness of the interface. The parameter χ essentially determines the contact zone size. Small values of χ result in no contact; while, large values give full contact. The shielding increases with mode-mix.

$$\Gamma = \Gamma_0\left(1 + \tan^2 \psi\right) \tag{4.48}$$

where ψ is the phase angle. According to Evans and Hutchinson [12], the transition between full contact and no contact occurs between χ values of 10 to 10^{-2}. Yet, Lane comments that a χ-value above 1 will not significantly increase the fracture toughness [5].

4.4 Sub-critical fracture

The fracture toughness of cracks is velocity dependent. Very fast cracks are usually denoted as the critical fracture toughness or critical strain-energy release rate for a material. However, slow cracks can occur at lower driving forces. These slow cracks are defined to be sub-critical. Sub-critical fracture for brittle materials is a stress-induced reaction between the material and corrosive species in the atmosphere. The rate of corrosion determines the sub-critical crack velocity and has three characteristic regimes. The ideal crack velocity curve is shown in Fig. 4.12. The initial part of the curve is defined as the threshold fracture energy. It is the minimum energy needed to propagate a crack. The first regime is due to the rate of reaction between the crack tip and corrosive species in the atmosphere. The crack velocity approaches the diffusion rate in the second regime and, finally, the third regime is attributed to critical fracture.

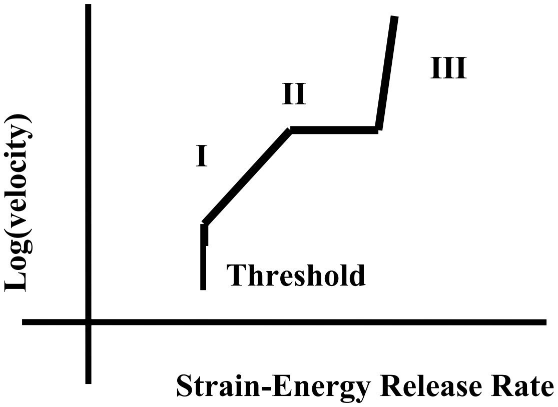

Figure 4.12 Ideal sub-critical fracture curve.

The derivation given in this section is attributed to Cook and Liniger [13]. The crack velocity in the reaction controlled region, or Region I, can be expressed as

$$v = v_0 * Sinh\left(\frac{G - \Gamma}{2NkT}\right) \tag{4.49}$$

where *G* is the strain-energy release rate, *Γ* is the fracture toughness, and *N* is the surface bond density. *T* and *k* are temperature and Boltzman's constant, respectively. From the slope of the velocity in Region I, the surface bond density, N, can be calculated. Furthermore, the bond rupture energy is related to the threshold fracture energy through the following equations [5]

$$\begin{gathered} \Gamma = N(\mu_{Si-O*} - \mu_{Si-O}) - N\mu_{H_2O} = Nu_0 \\ \mu_{H_2O} = \mu^0_{H_2O} + kT\ln(P_{H_2O}) \end{gathered} \tag{4.50}$$

The threshold fracture toughness is directly proportional to the bond rupture energy, u_0, and the partial pressure of water.

4.5 Summary

Chapter four discussed solid mechanics and fracture mechanics. The general equations of solid mechanics were used to derive the simpler equations of plane strain. Symmetry principles at an interface were also given and the Dundurs parameters were introduced. Most of the chapter was devoted to the development of fracture mechanics. The Griffith criterion was given and different boundary conditions were explored. It was also shown that the J-integral is equivalent to the Griffith criterion. The elastic solution for a crack in a brittle material was introduced for the normal modes I and II. By adding an interface to the problem, new stress intensity parameters were necessary. The problem now depends on a length scale and the oscillatory parameter. The location of the crack in an adhesive joint was investigated and the criteria for stable crack growth in an adhesive joint were derived. Also, the effect of inelastic processes—plasticity and asperity, were examined. Finally, the theory of stress-corrosion was applied to sub-critical crack growth.

Chapter 5 Analytical techniques

A few analytical techniques will be reviewed in Chapter 5. These techniques include X-ray Reflectivity (XRR), X-Ray Photoelectron Spectroscopy (XPS), Spectroscopic Ellipsometry, and Fourier Transform Infrared Spectroscopy (FTIR). XRR was used to measure the density, while XPS was used to measure the atomic composition. Spectroscopic Ellipsometry was used to measure the uniformity of the refractive index and film thickness. Finally, FTIR was employed to determine the molecular structure. The majority of this chapter will be devoted to a discussion of FTIR.

5.1 X-ray reflectivity measurements

Figure 5.1 demonstrates the basic arrangement of X-ray reflectivity (XRR) experiments. An x-ray with a typical wavelength of 1.54 Å is incident on a thin film deposited on silicon. For x-rays, the refractive index of the film is wavelength dependent, λ. The complex refractive index is

$$n(\lambda) = 1 - \delta - i\beta$$

$$\delta = \frac{r_0 \lambda^2}{2\pi} N_A \rho \frac{\sum_i c_i \left(Z_i + f_i^{'}\right)}{\sum_i c_i A_i} \qquad (5.1)$$

$$\beta = \frac{r_0 \lambda^2}{2\pi} N_A \rho \frac{\sum c_i f_i^{''}}{\sum_i c_i A_i}$$

where r_0 is the classical electron radius (2.8 fm); ρ the material mass density; N_A is Avogadro's Number; c_i is the number of the ith element in the chemical formula of the material; Z_i is the atomic number; A_i is the atomic weight; and f_i' and f_i'' are the real and imaginary dispersion correction factors of the *i*th element [1].

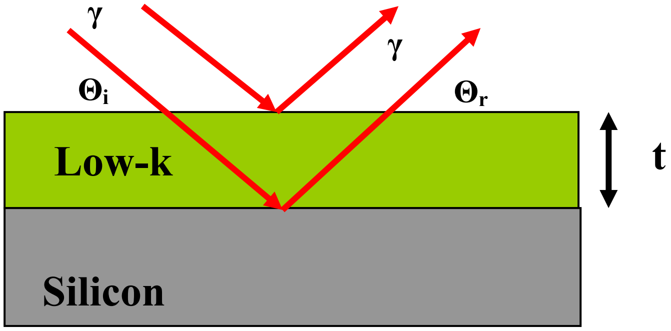

Figure 5.1 X-ray reflection from a low-k film deposited on silicon.

The real part of the refractive index is less than unity and, therefore, has a critical Brewster's angle where total internal reflection occurs at the interfaces [2]. The critical angle for the interface of a typical low-k material and air is ~ 0.12°; while the critical angle for a low-k/silicon interface is 0.205°. The critical angle can be related to the density of the film by

$$\theta_c = \sqrt{2\delta} \qquad (5.2)$$

Since the film has a thickness, *t*, the x-ray reflections from the top surface and the interface, in Fig. 5.1, produce peaks according to the Bragg condition

$$2t \sin\theta = n\lambda \qquad (5.3)$$

Fig. 5.2 depicts the results from a typical XRR experiment on a low-k film deposited on silicon.

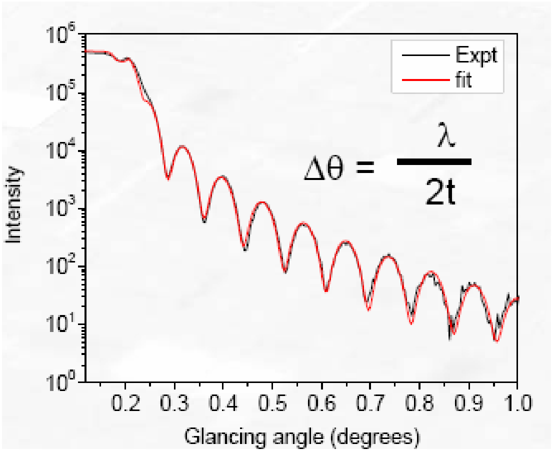

Figure 5.2 Inteferogram from XRR data of a low-k film deposited on silicon.

There are two initial drops in intensity. The first drop in intensity occurs around 0.15° and corresponds to the critical angle for low-k/air interface. A second drop occurs around 0.22° and is the critical angle for the low-k/silicon interface. The film thickness can be calculated from the periodicity of the interference peaks. The equation is inserted in Fig. 5.2.

XRR is a very robust analytic technique. It is possible to measure the density and thickness of multiple layers using XRR. In order to extract the data from the XRR results, a model is used that incorporates Schrodinger's Equation. There are software packages that will make the extraction. One example is PANanalytic X'Pert Reflectivity.

5.2 X-ray photoelectron spectroscopy

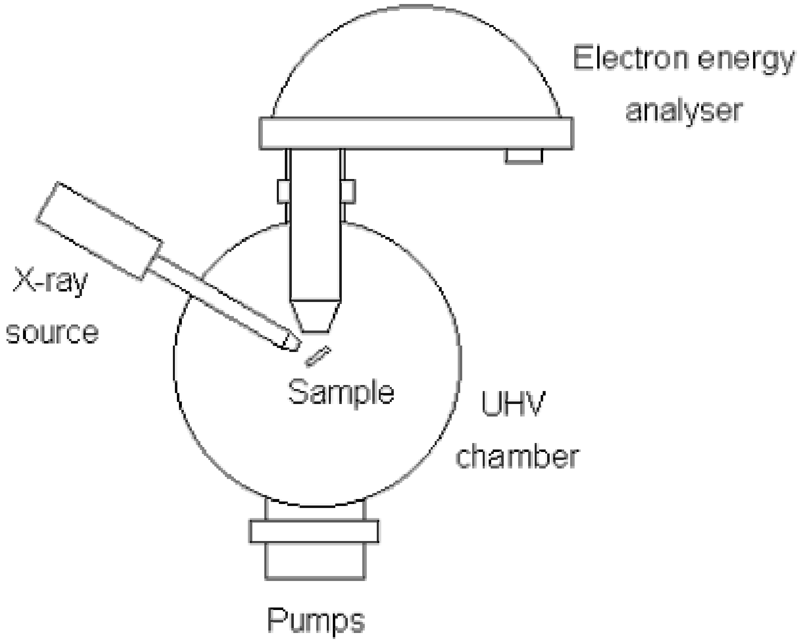

Figure 5.3. Schematic diagram of an XPS experimental set-up [3].

XPS is capable of determining the elemental composition, the concentration of those elements, and sometimes the bonding configuration of the element [4]. The elemental composition is measured by the interaction of soft x-rays with the core electrons of an element. For the XPS system used in this thesis, the soft x-rays were a monochromatic beam of Al Kα x-rays with an energy of 1486.6 eV. After photon absorption, the electron escapes the solid with a kinetic energy of

$$KE_{electron} = E_{photon} - E_{binding} - \varphi \tag{5.4}$$

where $E_{binding}$ is the binding energy of the core level and φ is the work function of the material [4]. An electron energy analyzer disperses the electrons according to their kinetic energy. The energy signature determines the elemental species. The intensity of the peak is directly proportional to the concentration of the atomic species. The constant of proportionality is the sensitivity factor. Table 5.1 contains the energy and sensitivity factors for important elements in this thesis-- silicon, oxygen, and carbon. XPS can not measure hydrogen. The energy signature shifts with different bonding configurations. The electron escape depth is about 10 to 12 nm.

Table 5.1 Binding energies and sensitivity factors for XPS analysis [5].

Element	Binding Energy (eV)	Sensitivity Factor
C (1s)	285.0	2.019
O (1s)	532.7	5.148
Si (2p)	99.3	1.866

5.3 Spectroscopic Ellipsometry

Spectroscopic ellipsometry is a useful technique for measuring the refractive index and film thickness. Ellipsometry employs the well known phenomena that the polarization of light changes when reflected from a dielectric surface. For instance, a linearly polarized beam of light, incident on a glass surface, will transition to an elliptically polarized beam after reflection. The experimental arrangement for a spectroscopic ellipsometer is depicted in Fig. 5.4. A light source emits a broad spectrum beam of light into a polarizer. After polarization, the light is incident on the sample, reflected, and the change in polarization measured.

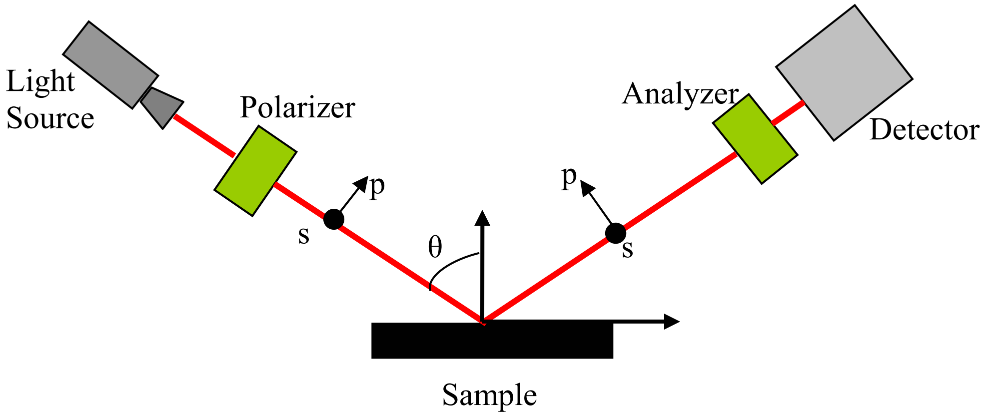

Figure 5.4 Schematic drawing of a spectroscopic ellipsometer.

In Fig. 5.4, the polarization vector is described by two orthonormal vectors, *p* and *s*. The *p* vector is parallel to the plane of incidence, while *s* is perpendicular. Both *p* and *s* are normal to the propagation vector for the beam of light. When the beam of light reflects off the surface, the magnitude the electric field in the direction of *p* and *s* will differ from the magnitudes of the incident beam, thus changing the polarization. The polarization and intensity of the reflected beam are measured at multiple incident angles for a broad spectrum of wavelengths. Typically, data for the 633 nm wavelength is used. Assume that the sample has a refractive index of n_2 and the surrounding medium (air) has refractive index n_1, the intensity of the reflected light in directions *p* and *s* can be expressed in terms of the incident angle and the refractive indices, Fresnel Equations [13].

$$R_s = \left(\frac{E_s}{E_0}\right)^2 = \left[\frac{n_1 \cdot \cos(\theta) - \sqrt{n_2^2 - n_1^2 \cdot \sin^2(\theta)}}{n_1 \cdot \cos(\theta) + \sqrt{n_2^2 - n_1^2 \cdot \sin^2(\theta)}}\right]^2$$

$$R_p = \left(\frac{E_p}{E_0}\right)^2 = \left[\frac{n_2^2 \cdot \cos(\theta) - n_1\sqrt{n_2^2 - n_1^2 \cdot \sin^2(\theta)}}{n_2^2 \cdot \cos(\theta) + n_1\sqrt{n_2^2 - n_1^2 \cdot \sin^2(\theta)}}\right]^2 \qquad (5.5)$$

The ratio of the Fresnel Equations, $\frac{R_p}{R_s}$, can be related to two parameters ψ and Δ, where

$$\frac{R_p}{R_s} = \tan(\psi) \cdot \exp[i\Delta] \qquad (5.6)$$

The function tan(ψ) is the magnitude of the amplitude ratio and Δ is the phase relationship. Given that we know the amplitude and phase relation, the dielectric constant can be calculated.

In order to calculate the film thickness, one must know how to relate the interference pattern to the film thickness. By measuring the angle resolved interference

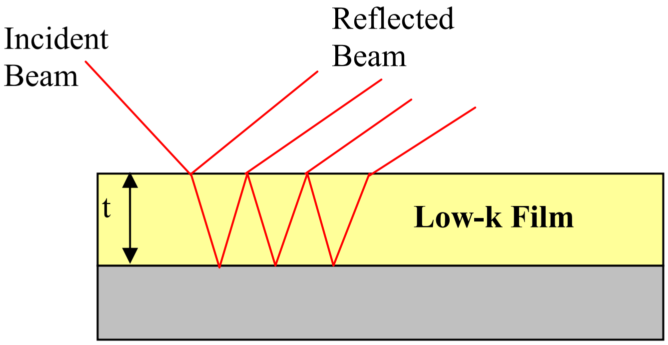

Figure 5.5 Refraction and reflection from a low-k film during an ellipsometer measurement.

pattern, the thickness can be calculated. Often the material will have multiple layers, the interference pattern for these layers will be convoluted with the reflection amplitudes for each interface. A simple model can be used to fit the spectroscopic data by giving approximate values for the dielectric constant and thickness of each layer. A regression analysis will use this approximate information to calculate the actual refractive index and film thickness.

For more information see the J. A. Woollam website, www.jawoollam.com/tutorials.

5.4 Fourier transform infrared spectroscopy (FTIR)

FTIR is a powerful technique for determining the molecular structure of a material. An infrared laser, with wavenumbers from 400 to 4000 cm^{-1}, is transmitted through a material and the characteristic wavelengths are absorbed. The infrared absorption spectra are determined by the vibrations and rotations of a molecule. In solids, the rotational spectra are suppressed. Using the spectral footprint, molecular structure can be determined.

A photon detector measures the light intensity for each wavenumber and the transmittance is calculated by the ratio of the transmitted and incident light intensities

$$T = \frac{I}{I_0} \tag{5.7}$$

where T is the transmittance and I is the measured intensity. I_0 is the intensity of the background sample. For instance, I is the measured intensity of a thin film on a silicon substrate and I_0 is the measured intensity of the silicon substrate.

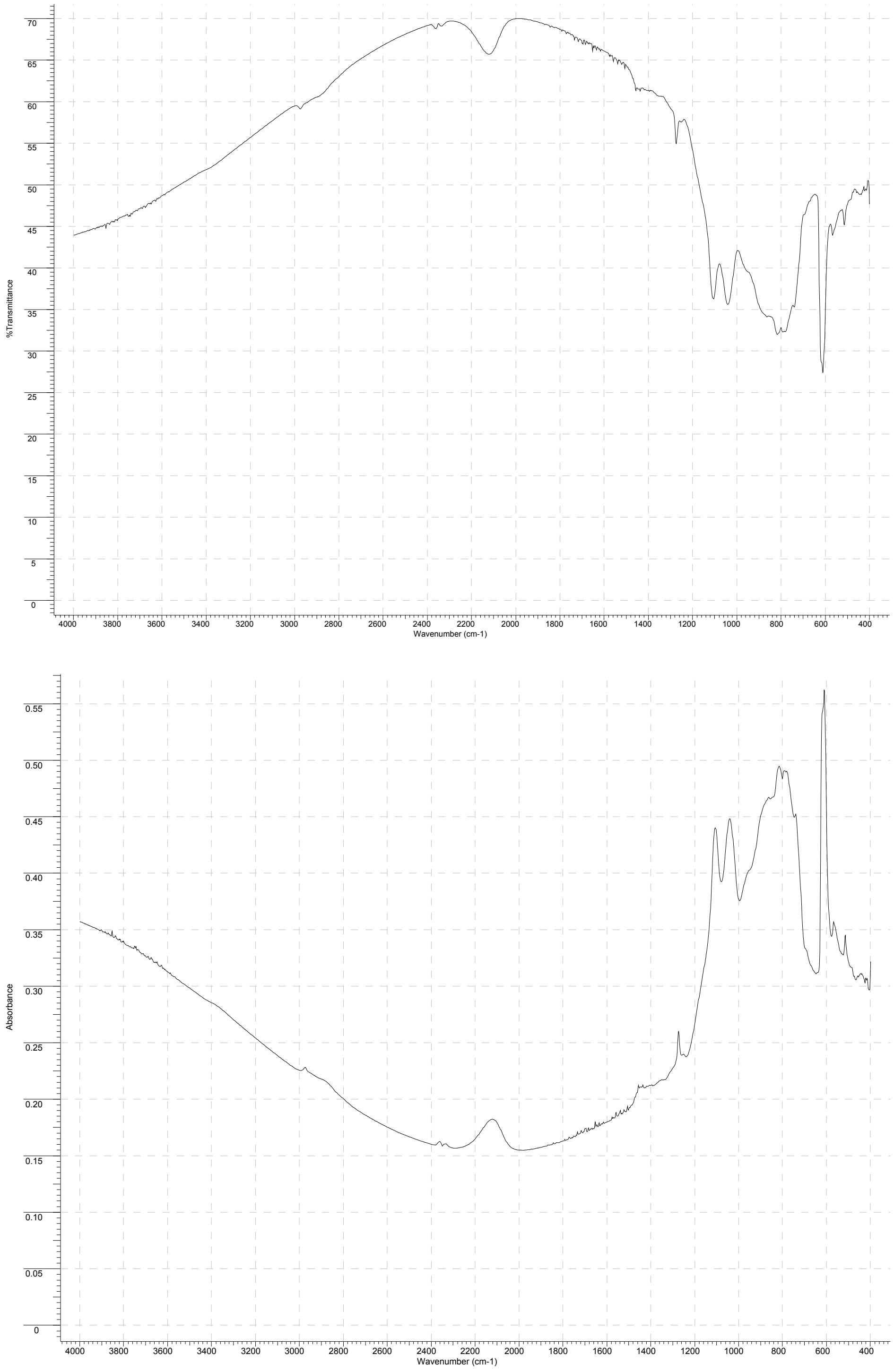

Figure 5.6 A FTIR transmittance curve is at top; while an absorbance trace is at bottom. Also apparent is the need to baseline.

According to Beer's Law, the absorbance (the logarithm of the transmittance), is directly proportional to the concentration of molecules and the thickness of the film.

$$A = -\log(T) = a \cdot c \cdot t \tag{5.8}$$

where a is the absorbance, c is the molecular concentration, and t is the film thickness [6]. Unfortunately, there are no standard tables for the absorbance. Without knowledge of the absorbance, we can only look at relative trends in the data. Often, a ratio of the intensity of spectral components is taken. This eliminates the need to know the thickness of the material.

In this thesis, all measurements were made in the transmittance mode. The films of interest were deposited on low-doped silicon wafers. Silicon is largely transparent in the range of wavelengths used in these FTIR experiments.

5.4.1 The Michelson interferometer

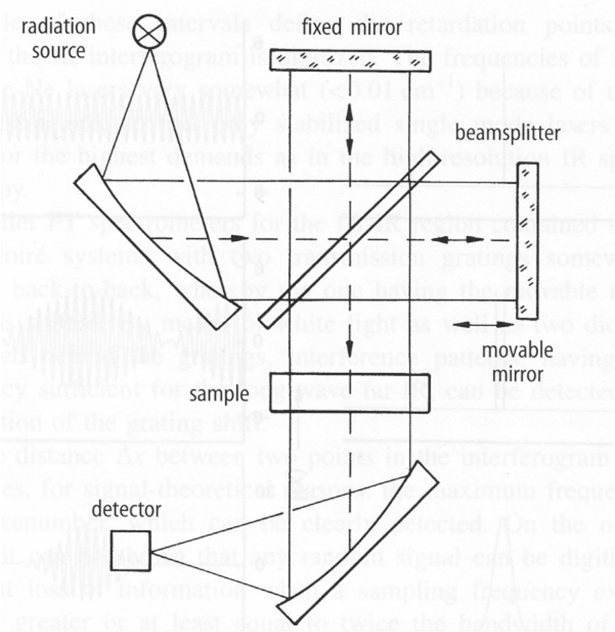

Figure 5.7 A schematic drawing of the Michelson Interferometer [6].

The Michelson Interferometer is the basic design of a FTIR system. It creates a mechanical convolution of the transmitted intensity of a broad band infrared source. The mechanical convolution can be Fourier Transformed back into a frequency dependent intensity profile [6].

Before considering a broad band source, let the radiation source be a monochromatic laser. The laser beam is incident on a collimating mirror that directs the source onto a beamsplitter. The beam is split onto a fixed mirror and a moving mirror. Let the dimension of mirror motion be x. When the beam path to the moving mirror is unequal to the fixed mirror path, a phase difference develops between the two split beams. The beams recombine at the beam splitter and are directed toward the sample and the transmittance is subsequently measured at the detector.

The difference in phase at the beam splitter leads to interference, modulating the incident intensity on the sample. The amplitude is a function of the displacement x.

$$I(x) = I_0\left(1 + \cos\left(2\pi\bar{\nu}x\right)\right) \tag{5.9}$$

where I_0 is the incident intensity, $\bar{\nu}$ is the wavenumber of the incident laser, and x is the difference in path length. Now, consider a polychromatic infrared beam. The intensity profile is

$$I(x) = \sum_{\bar{\nu}} S_{\bar{\nu}}\left(1 + \cos\left(2\pi\bar{\nu}x\right)\right) \tag{5.10}$$

Using Eq. 5.10, the inverse Fourier Transform can now be made. The intensity of each component of the polychromatic beam is

$$S_{\bar{\nu}} = \int_{-\infty}^{\infty} I(x)\cos(2\pi\bar{\nu}x)dx \tag{5.11}$$

The maximum wavenumber that can be measured depends on the minimum increment of translation, Δx.

$$\bar{\nu}_{\max} = \frac{1}{2\Delta x} \tag{5.12}$$

Likewise, the resolution of wavenumbers, $\Delta\bar{\nu}$, is dependent on the maximum translation of the moving mirror.

$$\Delta\bar{\nu} = \frac{1}{2x_{\max}} \tag{5.13}$$

The FTIR system used for this thesis had a wavenumber resolution of 4 cm^{-1}.

5.4.2 Data acquisition and baselining spectra

When the sample is placed in the FTIR transmittance holder and the chamber closed, nitrogen is used to purge the system of water vapor and carbon dioxide. The purge usually lasted fifteen minutes. Then, the infrared beam is directed onto the sample and a set of 256 spectra were taken from 400 to 4000 cm^{-1}. The 256 spectra are averaged to produce the final spectrum. Each set of spectra used the same background. The background was created by removing the thin film from the substrate with a razor blade. Before a careful examination of FTIR spectra, it is necessary to baseline the results. Baselining requires a determination of which peaks should be zero on the wavenumber scale and using a spline fit between them. Many analysis software packages provide an automatic baseline feature, but a more consistent method is needed to compare spectra, especially for subtractive techniques. In order to meet this requirement, a consistent baseline for all spectra measured was used. The wavenumbers to be zeroed are given in Table 5.2.

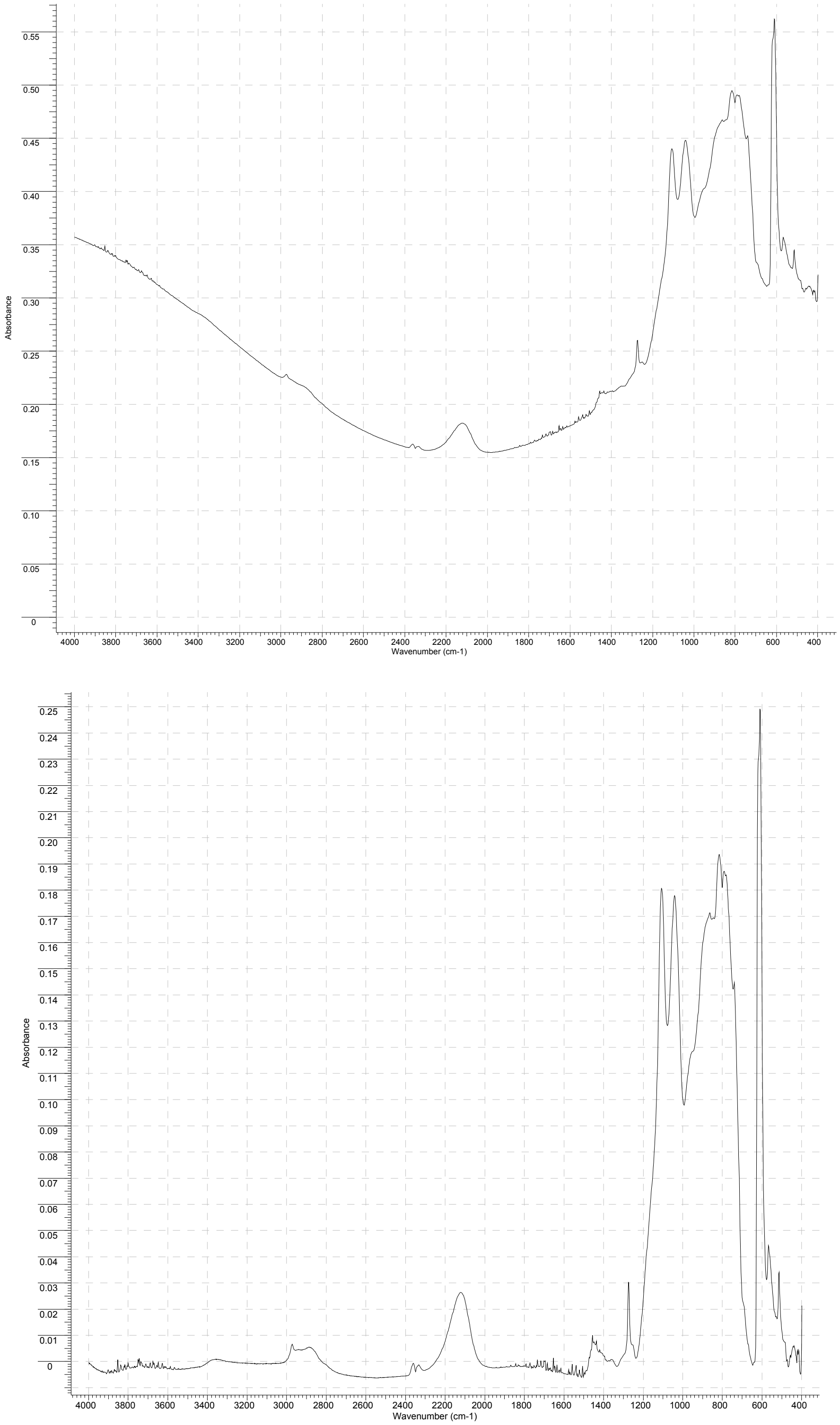

Figure 5.8 These traces depict the effect of baselining spectra. The figure at top is taken before baselining and the figure at bottom has been baselined.

Table 5.2 Wavenumbers that should have zero intensity.

Wavenumber (cm^{-1})	**Wavenumber (cm^{-1})**
3999.7	2309.9
3800.9	2137.4
3148.8	1801.2
3002.8	1330.5
2818.6	658.1
	523.6

5.4.3 Subtractive FTIR

Figure 5.9 demonstrates the subtractive FTIR technique [7]. After making a consistent baseline for two different spectra, the absorbance curves can be subtracted from each other. The negative peaks indicate a reduction of that molecular structure and a positive peak indicates an increase in that molecular structure. Subtractive FTIR will be employed in later sections to more accurately measure the molecular evolution of low-k dielectrics with UV exposure.

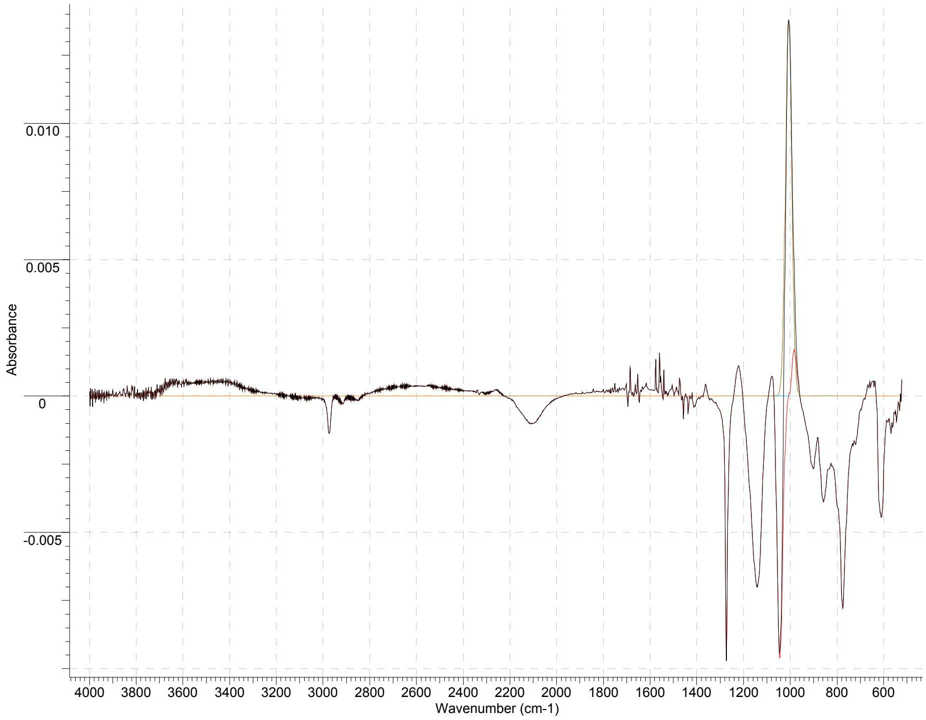

Figure 5.9 An example of subtractive FTIR.

5.4.4 The spectral distribution of OSG

FTIR measures the concentration of molecular species by measuring the photon absorption by vibrating molecules. The normal modes of vibration are quantized allowing for discrete absorption terms.

Fig. 5.10 is a typical FTIR spectrum of OSG. The principal peaks are grouped under the anti-symmetric stretch region of Si-O-Si – 900 to 1250 cm^{-1}. The symmetric bending of CH_3 in the silicon methyl bond is located at 1273 cm^{-1}. The silane (Si-H) peak is located at 2180 cm^{-1} and the antisymmetric stretch of the CH_3 occurs at 2970 cm^{-1}.

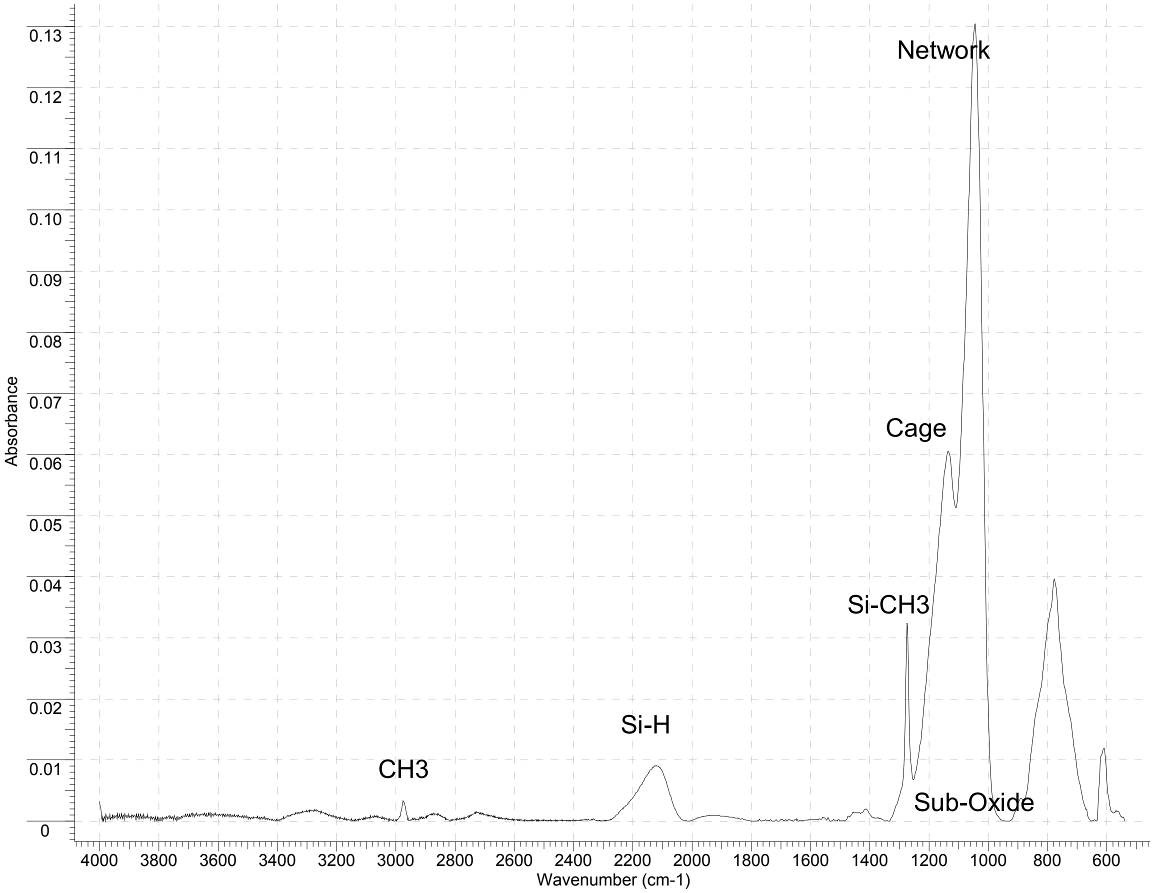

Figure 5.10 A typical FTIR Spectrum of OSG.

The vibrational frequencies of the Si-O-Si bond are dependent on the bond angle of Si-O-Si. A schematic is shown in Fig. 5.11.

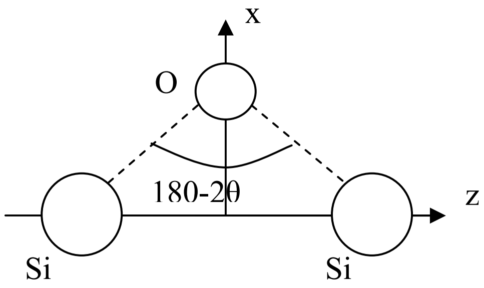

Figure 5.11 A schematic drawing of the Si-O-Si bond.

The vibrating frequency for the oxygen atom was found to be

$$\omega_z{}^2 = \frac{2k_O \cos^2 \theta}{M_O} \tag{5.14}$$

Following Eq. 5.14, the antisymmetric stretch region for the Si-O-Si bond can be decomposed to find three distinct molecular units. These units are cage, sub-oxide, and network. Table 5.3 contains the molecular unit, its vibrating frequency, and its bond angle. The spectral decomposition of the antisymmetric Si-O-Si region is shown in Fig. 5.12 [8].

Table 5.3 Molecular structure unit of Si-O-Si and their FTIR peaks and bond angles.

Structure	**Peak Position (cm^{-1})**	**Bond Angle (deg)**
Cage	**1135**	**~ 150**
Network	**1060**	**~ 144**
Sub-Oxide	**1028**	**< 140**

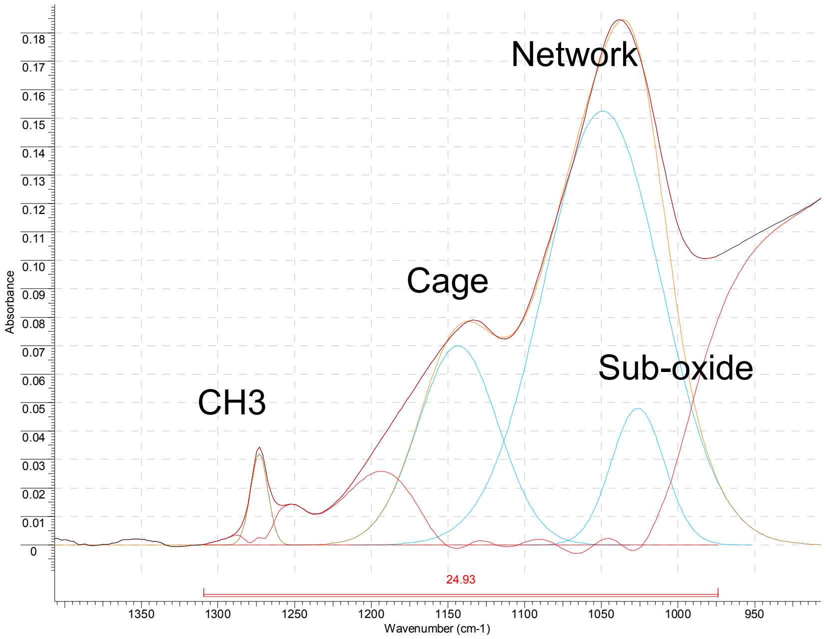

Figure 5.12 The spectral decomposition of the anti-symmetric stretch region of Si-O-Si and the components are labeled: cage, network, and sub-oxide.

In Chapter Two, the cage and network molecular units were explained in some detail. The sub-oxide unit was only briefly mentioned. The bond angle of the sub-oxide unit occurs when oxygen is substituted for silicon, carbon, or hydrogen and does not form the cage structure. The electronegativity of silicon, carbon, and hydrogen is lower than that of oxygen. Hence, a different dipole moment exists, distorting the tetrahedral bond to an angle less than 140° [8, 9].

Ross and Gleason have shown that the connectivity, discussed in Chapter 2, can be determined by decomposing the methyl peak at 1270 cm^{-1} [10]. The FTIR peaks for “M,” “D,” and “T” connectivity appear in the spectral range 1250, 1260, and 1270 cm^{-1}, respectively.

Table 5.4, shown below, contains the FTIR peak assignments for OSG films. It was taken from Grill and Neumayer [8].

Table 5.4 FTIR peak assignments for OSG [8].

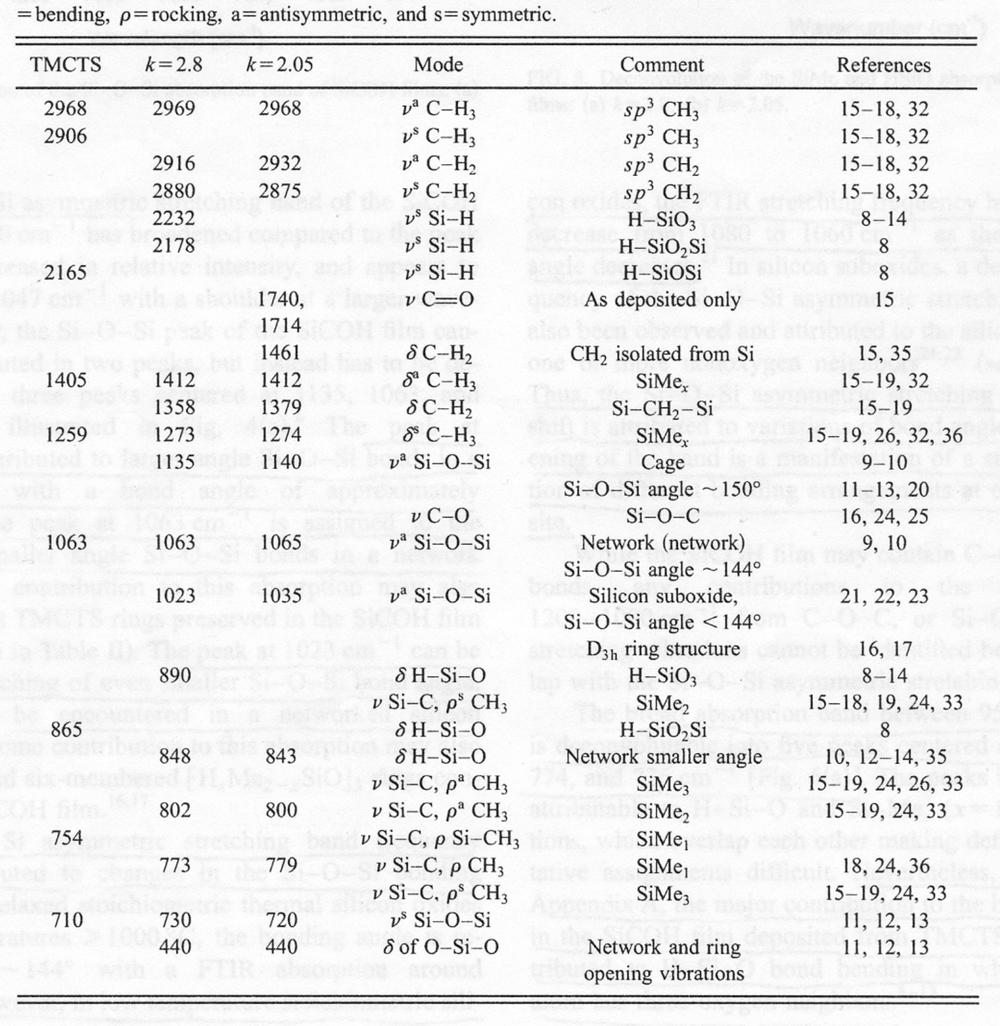

TABLE II. FTIR peak assignments. Major contributors are listed first for each vibration. ν = stretching, δ = bending, ρ = rocking, a = antisymmetric, and s = symmetric.

TMCTS	$k=2.8$	$k=2.05$	Mode	Comment	References
2968	2969	2968	ν^a C–H$_3$	sp^3 CH$_3$	15–18, 32
2906			ν^s C–H$_3$	sp^3 CH$_3$	15–18, 32
	2916	2932	ν^a C–H$_2$	sp^3 CH$_2$	15–18, 32
	2880	2875	ν^s C–H$_2$	sp^3 CH$_2$	15–18, 32
	2232		ν^s Si–H	H–SiO$_3$	8–14
	2178		ν^s Si–H	H–SiO$_2$Si	8
2165			ν^s Si–H	H–SiOSi	8
		1740, 1714	ν C=O	As deposited only	15
		1461	δ C–H$_2$	CH$_2$ isolated from Si	15, 35
1405	1412	1412	δ^a C–H$_3$	SiMe$_x$	15–19, 32
	1358	1379	δ C–H$_2$	Si–CH$_2$–Si	15–19
1259	1273	1274	δ^s C–H$_3$	SiMe$_x$	15–19, 26, 32, 36
	1135	1140	ν^a Si–O–Si	Cage	9–10
				Si–O–Si angle ~150°	11–13, 20
			ν C–O	Si–O–C	16, 24, 25
1063	1063	1065	ν^a Si–O–Si	Network (network) Si–O–Si angle ~144°	9, 10
	1023	1035	ν^a Si–O–Si	Silicon suboxide, Si–O–Si angle <144°	21, 22, 23
				D$_{3h}$ ring structure	16, 17
	890		δ H–Si–O	H–SiO$_3$	8–14
			ν Si–C, ρ^s CH$_3$	SiMe$_2$	15–18, 19, 24, 33
865			δ H–Si–O	H–SiO$_2$Si	8
	848	843	δ H–Si–O	Network smaller angle	10, 12–14, 35
			ν Si–C, ρ^a CH$_3$	SiMe$_3$	15–19, 24, 26, 33
	802	800	ν Si–C, ρ^a CH$_3$	SiMe$_2$	15–19, 24, 33
754			ν Si–C, ρ Si–CH$_3$	SiMe$_1$	
	773	779	ν Si–C, ρ CH$_3$	SiMe$_1$	18, 24, 36
			ν Si–C, ρ^s CH$_3$	SiMe$_3$	15–19, 24, 33
710	730	720	ν^s Si–O–Si		11, 12, 13
	440	440	δ of O–Si–O	Network and ring opening vibrations	11, 12, 13

5.4.5 The dipole moment and infrared absorption

In section 3.2, Eq.3.12, Fermi's Golden Rule was used to predict the photon absorption rate by an electron. Fermi's Golden Rule can be slightly modified for the absorption of a photon by a vibrating molecule.

$$\Gamma^{abs}(\omega) = \left[\frac{N_{k\lambda} c}{V}\right] \frac{4\pi^2}{\omega \cdot c} \sum_n \left|\langle n | j_{-k} | 0 \rangle\right|^2 \delta\left(E_n - E_0 - \hbar\omega\right) \tag{5.15}$$

For the purposes of this section, the interaction term will be discussed and its influence on absorption clarified. The interaction term is

$$\langle n|j_{-k}|0\rangle = \int e^{-i\vec{k}\bullet\vec{r}}\langle n|j(\vec{r})|0\rangle d^3r = \int d^3r\left[1 - i\vec{k}\bullet\vec{r} + ...\right]\langle n|j(\vec{r})|0\rangle \tag{5.16}$$

where the exponential has been expanded in terms of $\vec{k}\bullet\vec{r}$. Only the first term is needed.

$$\langle n|j_{-k}|0\rangle \cong \langle n|j_0|0\rangle \tag{5.17}$$

The classical current used in the interaction term is $j_0 = \sum_i q_i \, {}^{dx_i}\!/_{dt}$, where q_i is the charge of each vibrating atom and the derivative of x_i is the atomic velocity. From Heisenberg's Equation of Motion, the atomic velocity can be calculated

$$ {}^{dx_j}\!/_{dt} = \frac{1}{i\hbar}\left[x_j, H_0\right] \tag{5.18}$$

where x_j is the position vector of the jth atom and H_0 is the Hamiltonian of the vibrating system. Substituting Eq. 5.18 into Eq 5.17, the interaction term becomes

$$\langle n|j_{-k}|0\rangle = \frac{E_0 - E_n}{i\hbar}\sum_j \langle n|r_j|0\rangle = i\omega\cdot\vec{d}_{0n} \tag{5.19}$$

where E_0-E_n=-$\hbar\omega$=absorbed photon energy, and $\vec{d}_{0n}$ is the off diagonal matrix element of the molecular dipole moment. Using Eq. 5.19, the absorption rate can be re-written as

$$\Gamma^{abs}(\omega) = \left[\frac{N_{k\lambda}c}{V}\right]\frac{4\pi^2 q^2\omega}{c}\left|\vec{d}_{0n}\bullet\vec{\lambda}\right|^2 \tag{5.20}$$

where $\vec{\lambda}$ is the polarization vector for the incident photon. The important aspect of Eq. 5.20 is that, for absorption to occur, the vibrating molecule must possess a non-trivial dipole moment. Vibrations that do not induce a dipole moment are infrared inactive. As was discussed in Chapter 4, the charge on each vibrating atom is determined by its electronegativity. Some examples are illustrated in Fig. 5.13 [6].

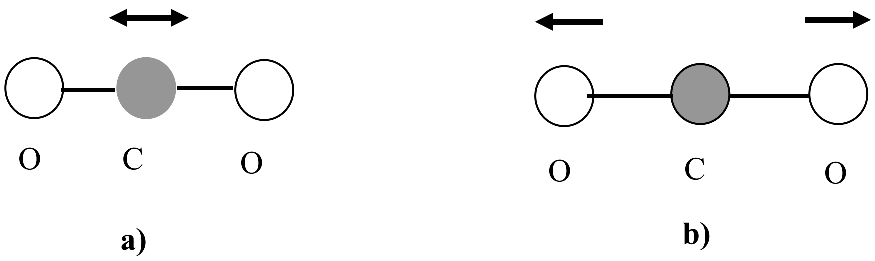

Figure 5.13. Vibrating systems a) is an IR active vibration with a non-trivial dipole moment. The vibrating system in b) is IR inactive with a trivial dipole moment [6].

5.4.6 The Kramers-Kronig relations

The FTIR spectra can also be used to measure the ionic contribution of the dielectric constant [11, 12]. The ionic contribution was discussed in section 2.2.2. The absorbance spectrum of FTIR essentially charts the frequency dependence of the absorption term of the refractive index. The relationship between the real or transmittance term of the refractive index and the imaginary or absorptive term is given by the Kramers-Kronig relations.

Consider an electro-magnetic wave normally incident on a dielectric film. In general, the refractive index is frequency dependent and has the form [13]

$$n(\omega) = \bar{n}(\omega) + i \cdot \kappa(\omega) \qquad (5.21)$$

The dispersion relation for an electromagnetic wave in a dielectric is , $\omega \cdot n = c \cdot k$; where ω is the frequency; c is the vacuum velocity of light; and k is the magnitude of the wavevector. Using the dispersion relation, the magnitude of the electromagnetic wave in the dielectric medium can be written

$$E = E_0 \exp\left[i\left(k \cdot x - \omega \cdot t\right)\right] = E_0 \exp\left[i \cdot \omega\left(\frac{n \cdot x}{c} - t\right)\right] \tag{5.22}$$

The refractive index in Eq. 5.21 can be substituted into Eq. 5.22.

$$E = E_0 \exp\left[\frac{-\omega \cdot \kappa(\omega) \cdot x}{c}\right] \cdot \exp\left[i \cdot \omega\left(\frac{\overline{n}(\omega) \cdot x}{c} - t\right)\right] \tag{5.23}$$

From Eq. 5.23, the time average of the amplitude can be written as

$$\frac{E_{average}}{E_0} = \exp\left[-\frac{\omega \cdot \kappa(\omega) \cdot x}{c}\right] \tag{5.24}$$

The time average amplitude in Eq. 5.24 can be related to the absorbance by

$$A(\overline{\nu}) = -\log\left(\frac{E_{average}^2}{E_0^2}\right) = -\frac{2}{2.31}\ln\left[\frac{E_{average}}{E_0}\right] = \frac{2 \cdot \omega \cdot \kappa(\omega) \cdot x}{2.31 \cdot c} = \frac{4\pi \cdot \overline{\nu} \cdot \kappa(\overline{\nu}) \cdot x}{2.31} \tag{5.25}$$

where $\overline{\nu}$ is the wavenumber. Eq. 5.25 will be used in the Kramers-Kronig relations [12].

The Kramers-Kronig relations use the Cauchy theorem of analyticity to relate the real and imaginary parts of the refractive index. For the purposes of this thesis, only the determination of the real part of the refractive index is needed. The Kramers-Kronig relation can be written as

$$n_i = n_\infty + \frac{2}{\pi} P\int_0^\infty \frac{\overline{\nu} \cdot \kappa(\overline{\nu})}{\overline{\nu}^2 - \overline{\nu}_i^2} d\overline{\nu} \tag{5.26}$$

where n_∞ is the refractive index at an asymptotic frequency and the subscript i indicates the frequency at which the refractive index is calculated. Unfortunately, we do not know the asymptotic refractive index. However, it is possible to measure the refractive index at a 633 nm wavelength or wavenumber of 15800 cm^{-1}, using an ellipsometer. The Kramers-Kronig relation can now be written as [12]

$$n_i = n_{15800} + \frac{2}{\pi}\left[P\int_{\bar{\nu}_a}^{\bar{\nu}_b} \frac{\bar{\nu}\cdot\kappa(\bar{\nu})}{\bar{\nu}^2 - \bar{\nu}_i^2} d\bar{\nu} - P\int_{\bar{\nu}_a}^{\bar{\nu}_b} \frac{\bar{\nu}\cdot\kappa(\bar{\nu})}{\bar{\nu}^2 - (15800)^2} d\bar{\nu} \right] \tag{5.27}$$

The limits of the integral have been changed to indicate the observed limits of the FTIR spectrum- 400 to 4000 cm^{-1}. The integrand in Eq. 5.27 can be written in terms of the FTIR absorbance spectrum, via Eq. 5.25.

$$\bar{\nu}\cdot\kappa(\bar{\nu}) = \frac{2.31\cdot A(\bar{\nu})}{4\pi\cdot d} \tag{5.28}$$

where d is the thickness of the dielectric film.

An example of the FTIR spectrum is given in Fig. 5.10. From this spectrum, the refractive index is calculated and shown in Fig. 5.14.

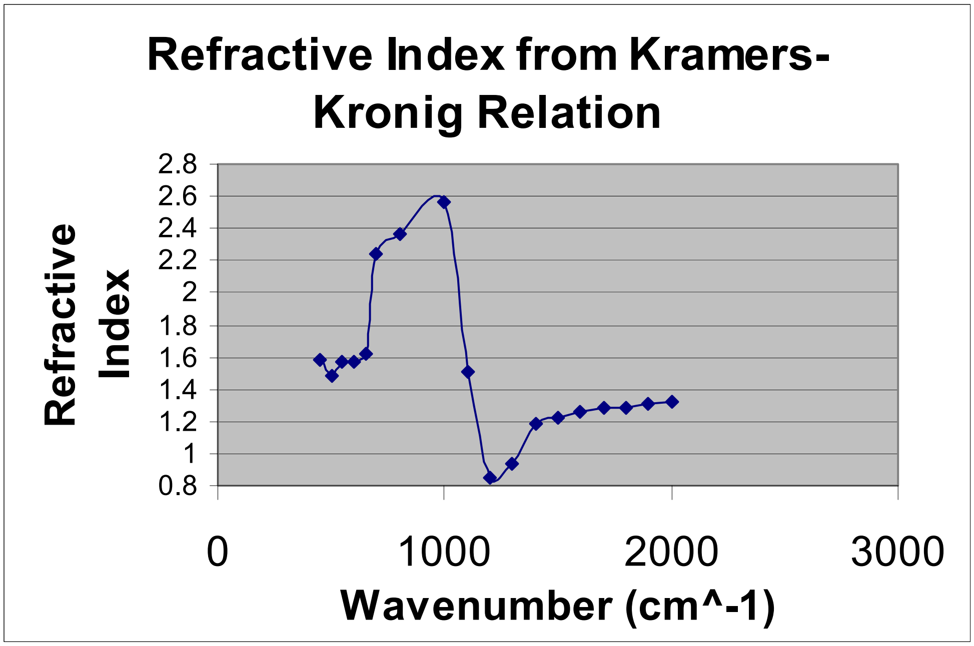

Figure 5.14 Calculation of the refractive index by the Kramers-Kronig relation.

The ionic contribution to the refractive index is measured as the difference in refractive index at low wavenumbers and the asymptotic value at high wavenumbers. The latter is usually taken to be the refractive index at 633 nm. The calculation of the dielectric constant is

$$\varepsilon_i = n_i^2 + \kappa_i^2 \tag{5.29}$$

The κ_i term on the right hand side of Eq. 5.29 can be calculated from Eq. 5.25.

5.5 Summary

Chapter 5 discussed four different analytical techniques that were used in this dissertation. X-ray Reflectivity was discussed first. It was shown that XRR can measure the mass density and film thickness of a low-k film. Next, the basics of X-ray

Photoelectron Spectroscopy were introduced. XPS can measure the elemental composition of the low-k film by analyzing the binding energy of the emitted electrons. Thirdly, Spectroscopic Ellipsometry was described. Ellipsometry can measure the refractive index and thickness of a low-k film. Finally, Fourier Transform Infrared Spectroscopy was discussed at length. Topics in FTIR were transmittance and absorption, the Fourier Transform method, data acquisition, subtractive FTIR, and the spectral distribution of p-OSG. Also, it was shown that FTIR can only characterize molecular vibrations that produce a dipole moment. The chapter concluded by calculating the ionic contribution of the dielectric constant from FTIR spectra.

Chapter 6 Experimental techniques in fracture

Chapter six will discuss the different techniques in fracture that were used to obtain the fracture toughness of UV cured OSG. The chapter begins with a discussion of sample preparation, followed by a presentation of the Four-point Bend Flexure Technique (4pt-bend). The Mixed-Mode Double Cantilever Beam (MMDCB) will be discussed next and, finally, the chapter will conclude with a discussion on sub-critical fracture measurements.

6.1 Sample preparation

The adhesive fracture toughness of the OSG/SiCN interface was investigated with two techniques: four-point bend flexure and mixed-mode double cantilever beam. Both techniques require the interface of interest to be sandwiched between two thick elastic layers. The elastic layers were typically made from 300 mm silicon wafers with a thickness of 770 um. Films were deposited on the test wafers in the following sequence: Si/OSG/SiCN. These wafers were mated to a dummy wafer of Si. Fracture samples were prepared in the following manner.

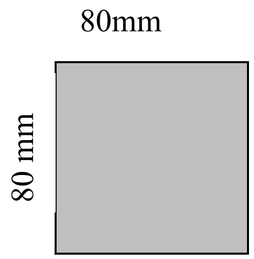

Step 1: A 80 mm × 80 mm piece was cleaved from the test and dummy wafers.

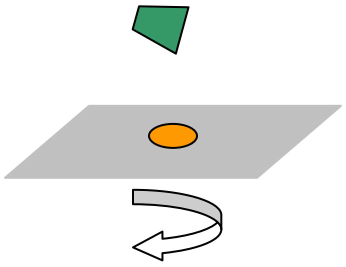

Step 2: Epoxy is spin coated on the 80 × 80 mm^2 test wafer at 6500 rpm. The sandwich is made and cured at 100°C for 1 hour.

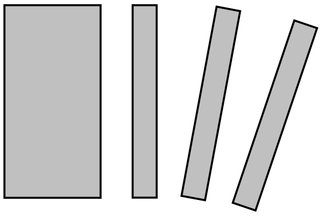

Step 3: Post cure. The 80 × 80 mm^2 sandwich is cleaved into individual 6 × 80 mm^2 planks, using a scribe and wafer cleavers.

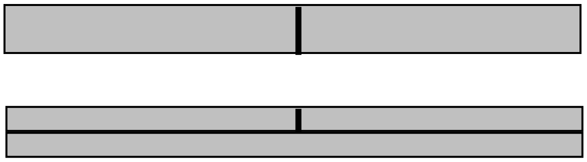

Step 4: A notch is made in the top 6 × 80 mm^2 plank using a K&S wafer saw.

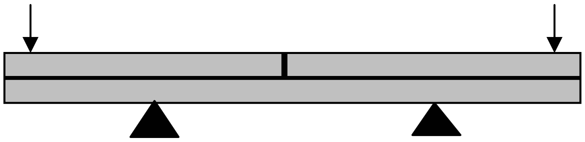

Step 5: Test in Four-point bend

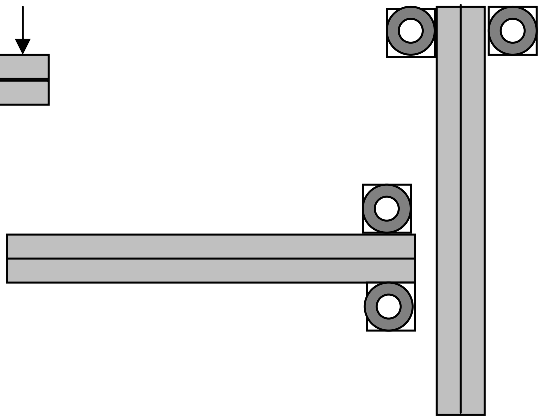

.

.

Step 6: Break Four-point bend samples in half and adhere aluminum tabs to the remaining halves.

The final film stack is Si/OSG/SiCN/Epoxy/Si. The stack layers can be seen in Fig. 6.1. The OSG film is 275 nm thick; while the SiCN cap layer is 300 nm. The thin epoxy layer is achieved by two processes. The epoxy is spin coated at 6500 rmp as described in Step 2 of sample preparation. After the dummy wafer is mated to the test wafer, mechanical pressure is applied with a vice grip and the sample was cured at 100°C for one hour. This ensures a uniform layer of epoxy with a thickness of one to two microns. It is important that the epoxy layer be as thin as possible.

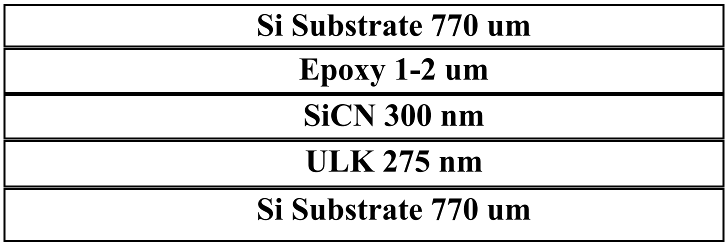

Figure 6.1 The OSG film stack after sample preparation for fracture experiments.

Aside from the epoxy thickness, the depth of the notch in 4-pt. bend samples is important. The distance between the notch bottom and the epoxy layer should not exceed 200 um.

6.2 Four-point bend flexure

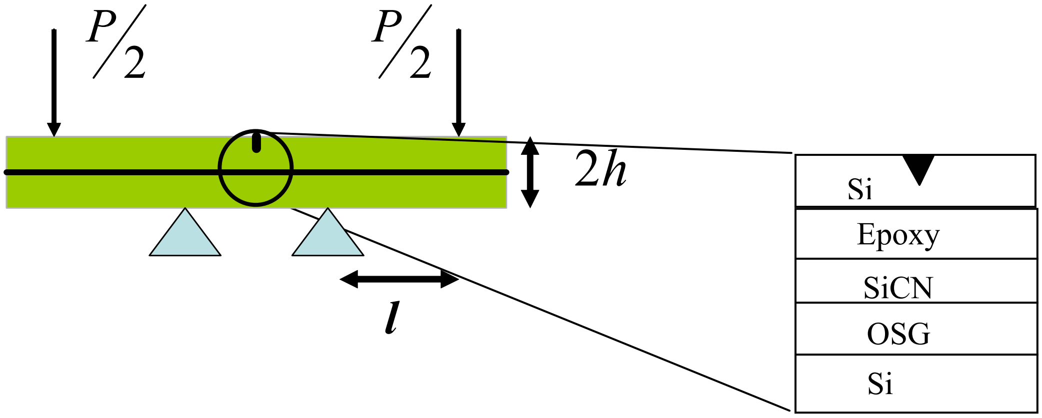

Figure 6.2 A diagram of the Four-Point Bend Flexure Technique.

The four-point bend technique has become a standard for the evaluation of adhesion of low-k films. The crack develops from the notch and propagates normal to the interface until it reaches the weakest interface, where it diverts parallel to the interface. In our samples, the crack diverted into the OSG, close to the OSG/SiCN interface.

The strain-energy release rate is a constant after the crack length is greater than twice the specimen thickness and while the crack remains within the inner load points [1]. The equation for the strain energy release rate is

$$G = \frac{21\left(1-\nu^2\right)P^2 l^2}{16 E b^2 h^3} \tag{6.1}$$

where P is the measured load, l the distance between inner and outer load points, b the sample width, h is the sandwich half-height. E is Young's Modulus, and ν is Poisson's Ratio. The constancy of the strain energy release rate can be easily shown. It is due to the constancy of the mechanical moment inside the interior nodes. Consider the origin of the system to be at the symmetry plane of the 4pt-bend system.

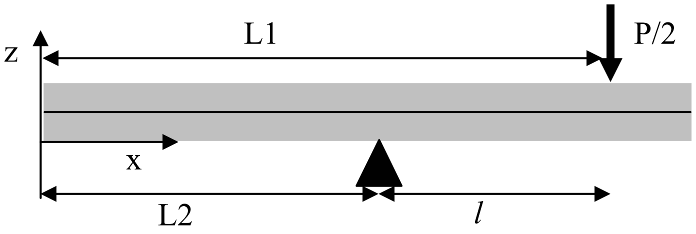

Figure 6.3 Moment configuration about the symmetry plane of a 4pt-bend sample.

$$M_{total} = \frac{P}{2}\left(L_1 - x\right) - \frac{P}{2}\left(L_2 - x\right) = \frac{P}{2}\left(L_1 - L_2\right) = \frac{P \cdot l}{2} \tag{6.2}$$

where M_{total} is the total moment within the interior load points.

The mode-mix for a crack between two elastic layers loaded in the 4-point bend is ~ 42°. Yet, the system contains more than two layers. The system that was tested contains five layers. The layer of particular interest was the OSG layer sandwiched between the Si and SiCN layers. The mode mix changes with the multiple layers. An FEM model of the four-point bend technique was made. It contained two large elastic beams of silicon, 1 mm x 6 mm x 70 mm, bonded together by a 5 um epoxy layer. A packaged program in ABAQUS made a path integral calculation that produced the stress intensity factors. It was found that the phase angle at the crack tip differs from 42°. A crack tip between the epoxy layer and the bottom silicon substrate has a phase angle of 37°. Later, a XPS study of the fracture surfaces will show that fracture of these samples was cohesive. A cohesive crack has a local mode-mix of zero.

The experimental procedure for 4pt-bend required pre-cracking the samples. Initially, the interior nodes were separated at a distance of 10 mm and the sample was loaded at 5 um/s to critical fracture. The sample was then unloaded and the interior node distance expanded to 55 mm. The sample was then loaded at 0.5 um/s to critical failure. Without pre-cracking, the characteristic plateau of 4pt bend experiments was often difficult to measure. The cracks would initiate and quickly spread to the interior nodes, meaning that the actual plateau was never observed. The load displacement curve for a pre-cracked sample is shown in Fig. 6.4. The load at the plateau can be used in Eq. 6.1 to calculate the strain-energy release rate.

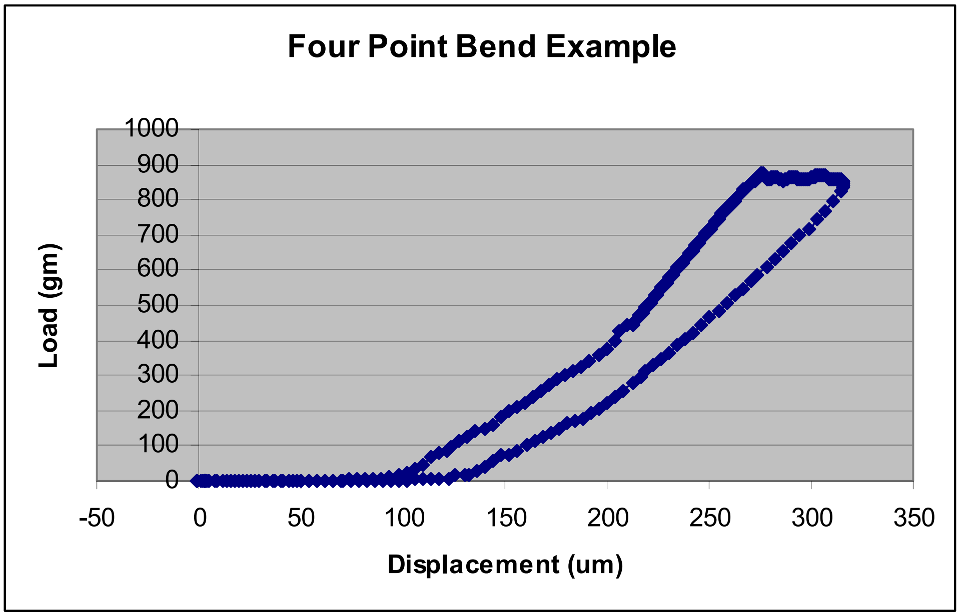

Figure 6.4 An example of the Four-Point Bend load vs. displacement curve.

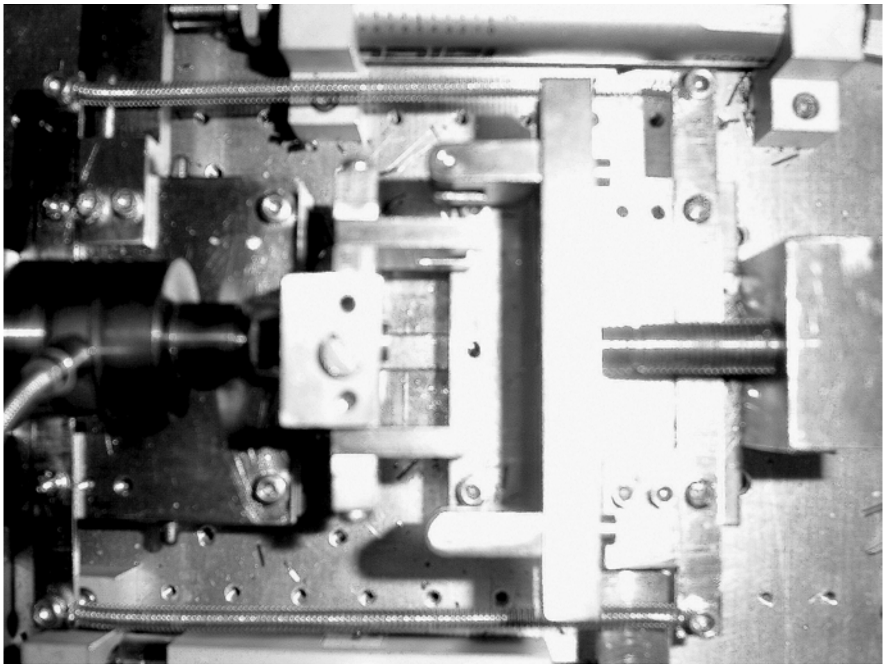

Figure 6.5 Photo of 4pt bend system.

6.3 The mixed mode double cantilever beam (MMDCB)

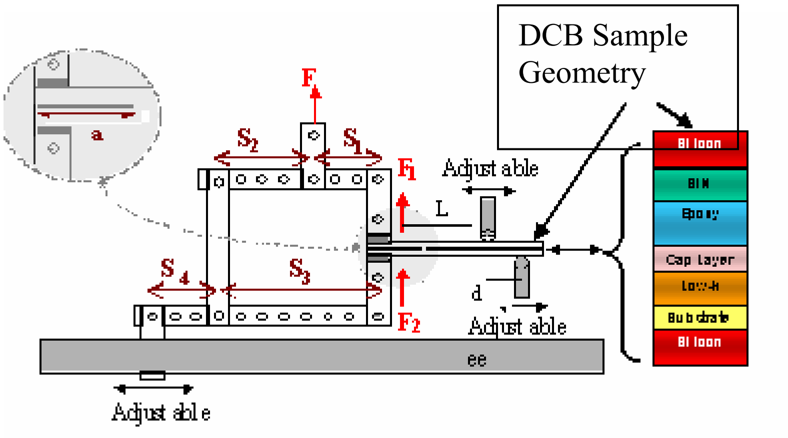

Figure 6.6 A schematic of the Mixed Mode Double Cantilever Beam system.

The Mixed-Mode Double Cantilever Beam (MMDCB) technique was originally developed by Fernlund and Spelt [2]. It consists of a load jig with several pivot points. Four of these pivot points can be moved to change the jig geometry by varying the spacing $s_1, s_2, s_3, \text{and}\, s_4$, seen in Fig 6.6. The load jig attaches to aluminum tabs bonded to the test specimen (step 6 in sample preparation). Depending on the jig geometry, a different force will be exerted on each tab, F_1 and F_2.

$$\begin{aligned} F_1 &= \frac{F}{b}\left(1 - \frac{s_1}{s_3}\right) \\ F_2 &= F_1\left(\frac{s_1}{s_2}\right)\frac{1}{1+\dfrac{s_3}{s_4}} \end{aligned} \tag{6.3}$$

where F is the load applied to the jig, b is the sample width, and $s_1, s_2, s_3, \text{and}\, s_4$ are defined in Fig. 6.6. Assuming that the adhesive layer is thin, the strain-energy release rate, G, and the phase angle of loading, ψ, can be expressed in terms of the forces as

$$G = \frac{(F_1 a)^2}{2D}\left[1+\left(\frac{F_2}{F_1}\right)^2-\frac{1}{8}\left(1+\left(\frac{F_2}{F_1}\right)^2\right)\right]$$

$$\psi = \arctan\left[\frac{\sqrt{3}}{2}\frac{\left(\frac{F_1}{F_2}+1\right)}{\left(\frac{F_1}{F_2}-1\right)}\right] \tag{6.4}$$

$$D = \frac{Eh^3}{12}$$

where *a* is the crack length and *D* is the flexural rigidity per unit width. In order to calculate *G*, we must know the crack length. The crack length is calculated from the system compliance.

The sample compliance and the MMDCB jig's compliance are not the same. In order to calculate the initial crack length, the jig compliance must be found and related to the sample compliance. The displacements of the sample, δ_1 and δ_2, at the load points are known from beam theory.

$$\begin{aligned}\delta_1 &= \frac{F_1}{D}\left[\frac{a^3}{3}+\frac{1}{24}\left(1+\frac{F_2}{F_1}\right)\left(L^2(L+d)-a^3\right)\right]\\ \delta_2 &= \frac{F_1}{D}\left[\frac{a^3}{3}\frac{F_2}{F_1}+\frac{1}{24}\left(1+\frac{F_2}{F_1}\right)\left(L^2(L+d)-a^3\right)\right]\end{aligned} \tag{6.5}$$

where the parameters *L* and *d* can be found in Fig. 6.6.

Let the displacement at the load point of the jig be Δ. The displacement is restricted to one dimension. From geometry, we find that

$$\Delta = \left(\frac{s_2}{s_1 + s_2}\right)\delta_1 + \left(\frac{s_4}{s_3 + s_4}\right)\delta_2 = c_{12}\delta_1 + c_{34}\delta_2$$

$$c_{12} = \frac{s_2}{s_1 + s_2} \qquad c_{34} = \frac{s_4}{s_3 + s_4} \tag{6.6}$$

After solving some algebra, the crack length can be found.

$$a^3 = \frac{3bD\left(\frac{\Delta}{F}\right)\left[\frac{s_3}{s_3 - s_1}\right] - \frac{1}{8}L^2(L+d)\left(1 + \frac{F_2}{F_1}\right)(c_{12} + c_{34})}{\left\{c_{12} + \frac{F_2}{F_1}c_{34} - \frac{1}{8}\left(1 + \frac{F_2}{F_1}\right)(c_{12} + c_{34})\right\}} \tag{6.7}$$

The MMDCB is not an inherently stable test. The window of stability is inversely related to the phase angle and can be expressed in terms of a single parameter, β.

$$\beta = \frac{L^2(L+d)}{a^3} - 1 \tag{6.8}$$

A graph of the phase angle vs. β is given in Fig. 6.7. The stable region lies below the curve and the unstable region lies above it.

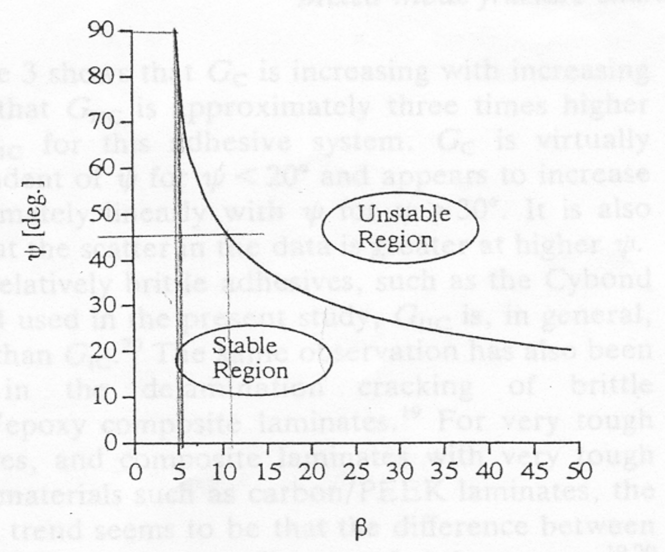

Figure 6.7 The stability curve for the MMDCB [2].

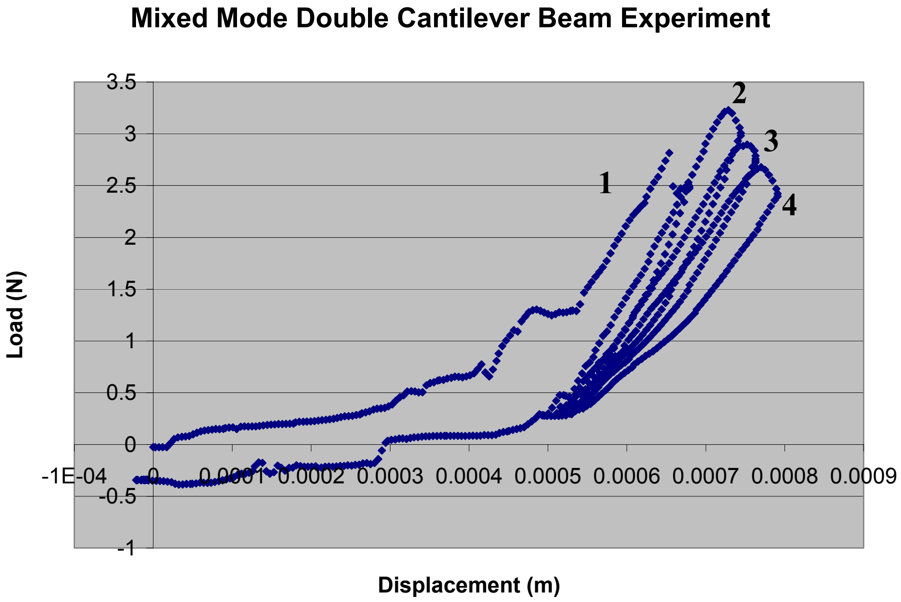

Figure 6.8 An example of the load vs. displacement curve for the critical fracture of a Mixed Mode Double Cantilever Beam sample.

Fig. 6.8 depicts the load vs. displacement curve for a critical fracture toughness experiment with the MMDCB. There are three important observations about this chart. First, the initial run-up to critical failure should not be used for calculating the fracture toughness. The MMDCB samples were made from the 4pt-bend samples and therefore the crack location may change with a MMDCB test at a new phase angle. The second run-up to critical fracture is therefore taken as the real fracture toughness. Second, at the critical fracture point the load curve begins to decrease, indicating that the fracture is moving faster than the system can be loaded. Therefore, the velocity of the crack should be maintained between experiments. If the loading rate is held constant, the velocity of the crack will change with mode-mix. The load rate was consequently changed with each mode-mix to maintain a constant crack velocity. Third, friction affects the measurement.

During the initial load, the effect of friction is quite noticeable—another reason not to use the first load cycle. After unloading and reloading, the effect does not appear to be as significant; but, some friction remains and must be subtracted from the load curve. The contribution of friction can be seen by the small plateau at the beginning of each load curve.

In order to calculate the strain-energy release rate of the MMDCB, it is necessary to know the initial crack length. The crack length can be calculated from the compliance in Eq. 6.7. The factor Δ/F can be replaced by the slope of the loading curve in Fig. 6.8. The critical fracture toughness is calculated using the initial crack length and the peak load.

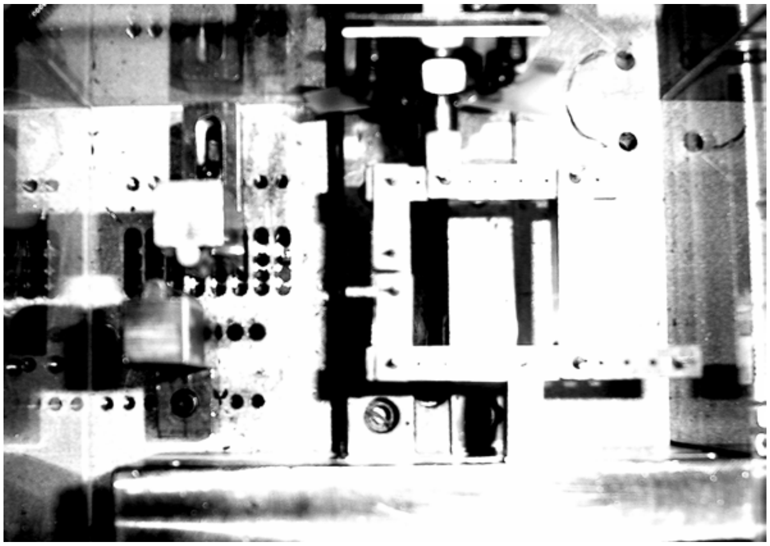

Figure 6.9 Photo of the Mixed Mode Double Cantilever Beam system.

6.4 Subcritical fracture experiments

Sub-critical fracture is time dependent and by definition occurs at loads below the critical stress-energy release rate. In our experiments, we induced sub-critical crack growth by static displacement. The MMDCB jig was loaded until the beginning of critical fracture, as indicated by a brief plateau in the load-displacement trace, and stopped. The location of the plateau depends on the velocity of the crosshead. In order to capture crack velocities near 1 mm/s, it is necessary to actuate the crosshead at a rate of 10 $\mu m/s$ .We can calculate the crack velocity from the compliance.

$$da/dt = -\frac{a_0}{3F}\frac{dF}{dt} \tag{6.9}$$

where a_0 is the initial crack length and F is the applied load. Eq. 6.9 is only accurate for a Mode I arrangement of the MMDCB. The initial crack length is calculated in the same manner as for critical loads, using Eq. 6.7. When numerically calculating the subsequent sub-critical crack growth, the following expression is useful.

$$\begin{aligned} \Delta a &= -\frac{a_0}{3}\cdot\frac{\Delta F}{F} \\ a_i &= a_{i-1} - \frac{a_{i-1}}{3}\cdot\frac{F_i - F_{i-1}}{F_{i-1}} \end{aligned} \tag{6.10}$$

The crack velocity is then taken to be the slope of the crack length vs time curve for each crack length a_i. .Shown below in Fig. 6.10 is the load vs. time curve for sub-critical fracture. However, it should be noted that the contribution of friction to the load must be subtracted from the load curve in Fig. 6.10, shifting the entire curve down. The resulting load should be F_i used in Eq. 6.10. The strain-energy release rate is calculated by Eq. 6.4 for each crack length a_i and load F_i. .

$$G_i \sim (F_i \cdot a_i)^2 \tag{6.11}$$

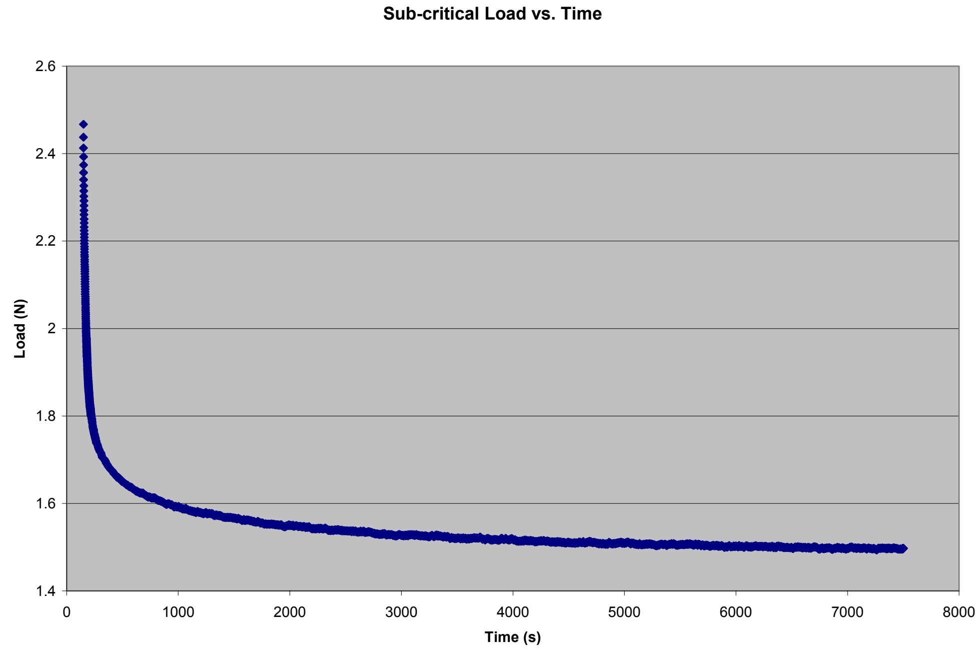

Figure 6.10 Load vs. time for sub-critical fracture loaded in Mode I.

All sub-critical crack growth experiments were performed in a controlled atmosphere. A small polycarbonate box covered the MMDCB jig and had a port for pumping moisture into the chamber. A dry nitrogen line led to a water bath, where it picks up moisture, and supplied the chamber with constant humidity. The humidity limits of the chamber were 10% to 85% RH. Temperature in the box was not controlled and typically stayed at ambient ~ $23^\circ C$.

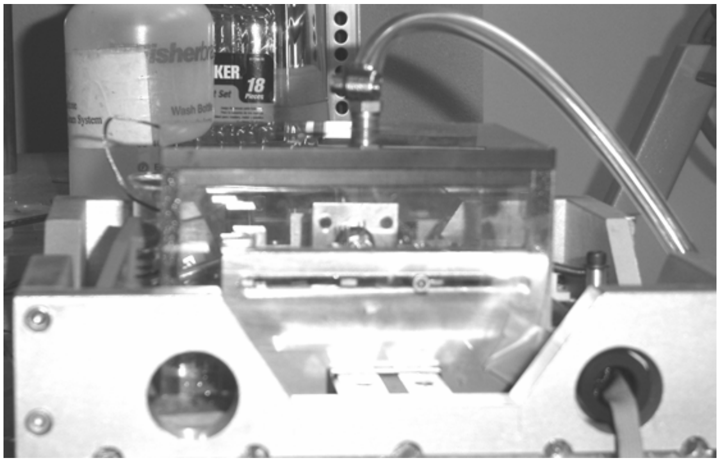

Figure 6.11 Photo of the relative humidity chamber that encloses the MMDCB.

6.5 Summary

Chapter six discussed the fracture experiments used in this dissertation. The chapter began with presentation of the sample preparation method. The preparation method for both Four-point Bend Flexure (4pt bend) and Mixed-Mode Double Cantilever Beam (MMDCB) was given. Several aspects of 4pt. bend were outlined. It was shown that the strain-energy release rate was a constant within the interior nodes. The phase angle was also constant within the interior nodes. The method of data acquisition was also presented. The MMDCB was discussed. Equations for the strain-energy release rate and phase angle were reported. It was shown that the sample compliance and the jig compliance were not the same and the equations for extracting the crack length were derived. The technique for data acquisition was also discussed. Finally, the method of sub-critical fracture experiments was presented.

Chapter 7 Results: Part I, material properties of a UV cured ultra low-k.

In Chapters 7 and 8, an investigation of the effect of UV curing on the molecular structure and fracture properties of a porous OSG material with k ~2.5 is presented. By following the UV exposure time, the modification of the molecular structure and its affect on material properties were examined.

These results are divided in two parts. This chapter, Part I, discusses the influence of UV curing on the material properties and molecular structure of the ULK film. The material properties presented will include changes in density, mass, and k-value. Molecular structure will be investigated with Fourier Transform IR (FTIR) and X-ray Photo-emission Spectroscopy (XPS). The changes in molecular structure will be correlated to condensation reactions with UV light that directly affect material properties.

I would like to acknowledge Ting Tsui, formerly at Texas Instruments, for sample preparations and some of the film characterization in section 7.2. Particularly, the data in Figs. 7.2, 7.3, and 7.4 were obtained at Texas Instruments in Dallas, TX.

7.1 Materials

For this study, an ultra-low-k was PECVD deposited on a silicon substrate, using a diethoxymethylsilane (DEMS) precursor, and loaded with an aromatic-organic porogen.

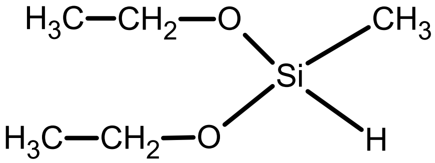

Figure 7.1 Chemical structure of diethoxymethylsilane (DEMS).

Table 7.1. UV cure schedule for ULK

Thermal Cure Temperature (deg C)	400	400	400	400	400
UV Cure Time (min)	0	1	2	9	36

The exact deposition technique is proprietary. The porogen was subtracted from the film during subsequent heating and UV exposure. The final film had a porosity of 25%. The pores were uniformly distributed with a mean pore size of 2 nm. The deposited films were cured with UV light, 6kW output, for multiple exposure times at 400 ˚C, under ultra-high vacuum (UHV). After UV curing the films were capped with SiCN. The final stack was Si/ULK/SiCN. The cure schedule can be found in Table 7.1.

7.2 Film characterization

7.2.1 Material properties, including shrinkage, density, and dielectric constant

During the UV cure process, several material properties changed, including the out-of-plane thickness, the modulus, the in-plane stress, the density, and dielectric constant. The film shrank by ~22% in the out-of-plane thickness after a 40 minute exposure, Fig. 7.2. The hardness and modulus increased by ~18% and 20%, respectively, after a 25 minute UV exposure. The hardness and modulus were measured by nano-indentation at Texas Instruments. Both the modulus increase and film shrinkage indicated an increase in the in-plane stress. The in-plane stress was measured and found to increase ~ 46% after sixty minutes of UV exposure.

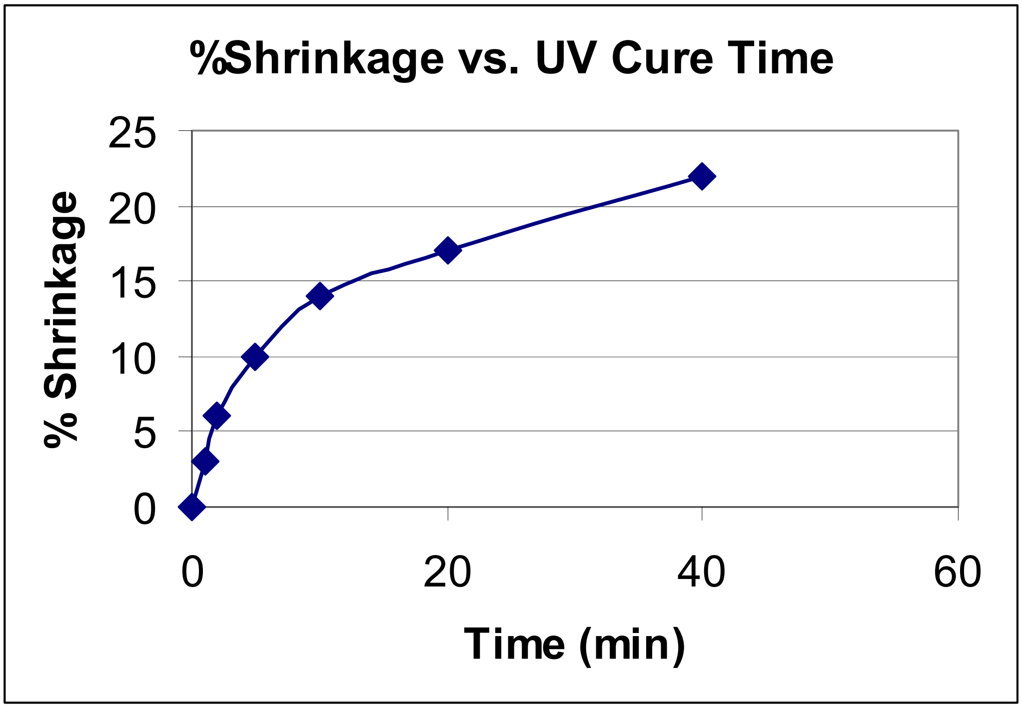

Figure 7.2 The percent volume shrinkage after UV exposure.

The effect of UV curing on film density and dielectric constant (k-value) are plotted in Figs. 7.3 and 7.4. During the first minute of UV cure, the porogen is removed which leads to a drop in density and k-value. The subsequent increase in density and k-value were attributed to changes in the molecular structure. The removal of the porogen will be demonstrated later in the discussion of FTIR results.

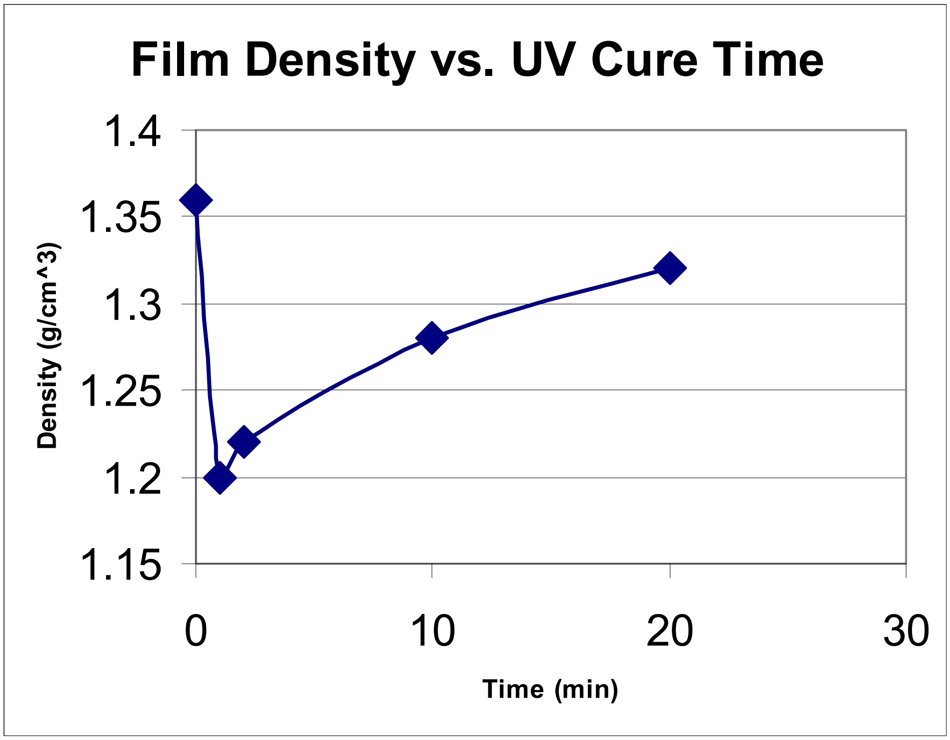

Figure 7.3 Density (g/cm^3) as a function of UV cure time.

In section 2.4.4, the connectivity of OSG molecular units were labeled M, D, T, and Q, according to the number of oxygen bonds in the OSG unit. In a later section of this chapter, the FTIR spectra will show that the connectivity of the OSG films, in this thesis, is primarily T with a small contribution of M. Therefore, it is assumed that the average stoichiometry of the p-OSG film is $(CH_3)SiO_{3/2}$.

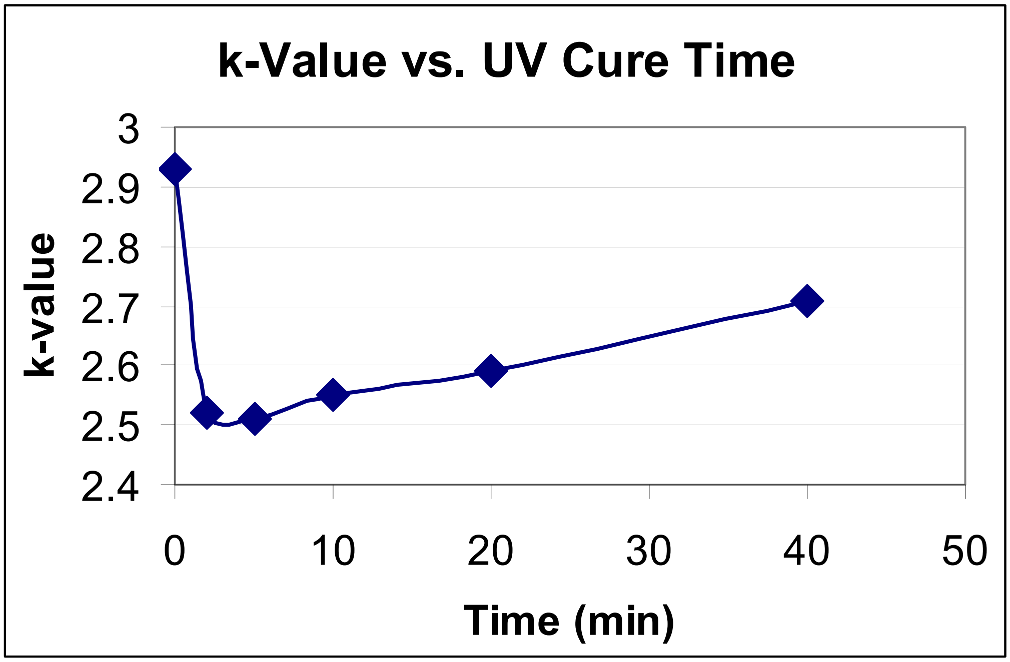

Figure 7.4 k-values as a function of UV cure exposure.

From the volume shrinkage and density measurements, it is possible to calculate the percent mass lost during UV curing.

$$\frac{M}{M_0} = \frac{\rho \cdot V}{\rho_0 \cdot V_0} \tag{7.1}$$

where M is the film mass, ρ is the film density, and V is the film volume. The subscript in Eq. 7.1 refers to the initial value without UV cure. The quantity V/V_0 is taken from the %Shrinkage in Fig. 7.2 ($V/V_0 = 1 - \%Shrinkage$). The density is taken from Fig. 7.3. Since V/V_0 is a decreasing function of cure time, the film lost mass during the UV cure as can be seen in Fig. 7.5. After a twenty minute exposure, the film has lost approximately nine percent of its initial mass.

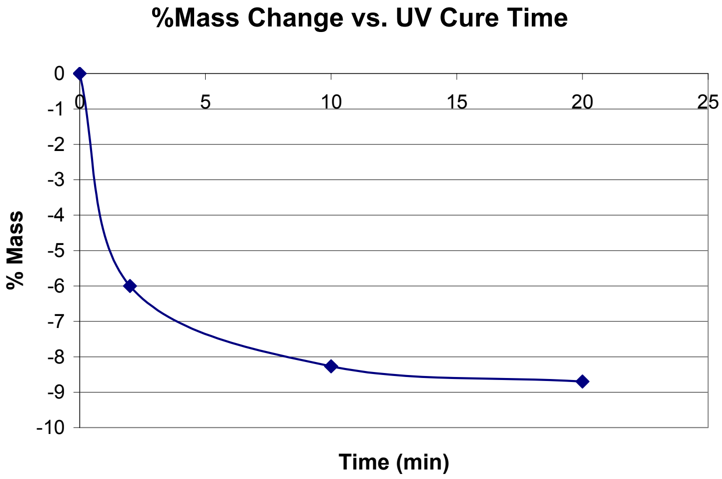

Figure 7.5 Percent mass lost during UV exposure.

Using XPS, the elemental composition of the OSG film can be measured. The results show that carbon is depleted during UV exposure. The ratio of carbon to silicon is charted in Fig. 7.6 as a function of UV cure. The loss of carbon indicates that the interaction of UV light and the film produces methane. Assuming that the initial drop is due to porogen removal, UV curing liberates 38% of the carbon in the film. Given an average stoichiometry of $(CH_3)SiO_{3/2}$, a 38% loss of carbon translates into a 7% loss in mass.

With the removal of carbon from the film, it may be asked whether the effects of UV cure are uniform. In Fig. 7.7, an XPS depth profile is displayed for a sample that has been cured for ten minutes. The profile suggests that UV light penetrates the film and uniformly interacts with the molecules. A J.A. Woollam ellipsometer was also used to measure the depth profile of the refractive index. The best fit was a uniform refractive index. A uniform film is not necessarily obvious. Beer's Law requires that the intensity of light transmitted through the film decreases exponentially. The uniformity implies that the film weakly absorbs the UV light.

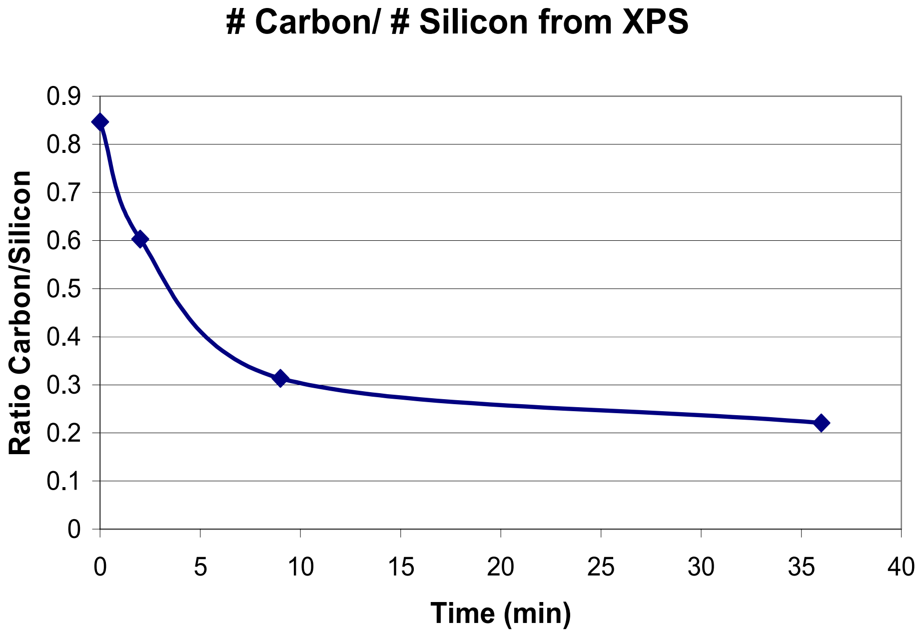

Figure 7.6 Ratio of carbon to silicon content from XPS data.

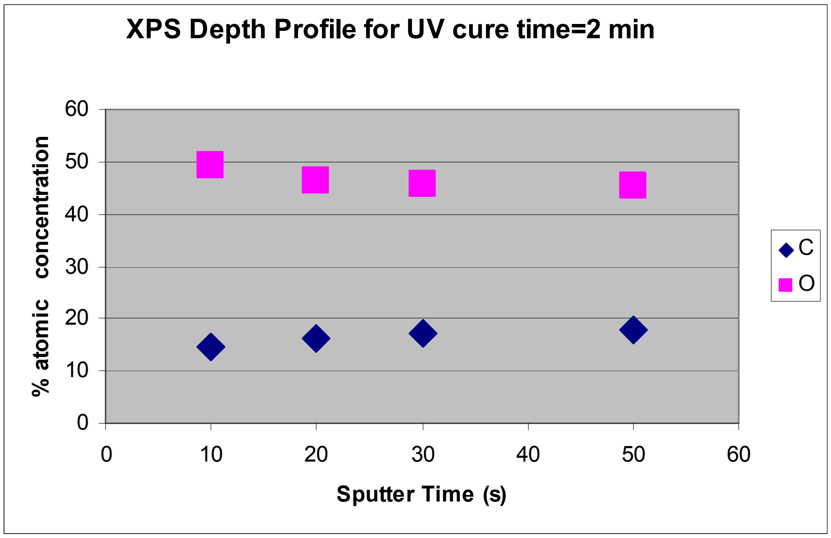

Figure 7.7 XPS depth profile of an OSG film after 10 minutes of UV exposure.

7.2.2 The dielectric constant: electronic and ionic contributions

The k-value in Fig. 7.4 was measured at 1 MHz. At 1 MHz, the dielectric constant has contributions from electronic (Δk_e), ionic (Δk_i), and dipolar (Δk_d) polarizations, Eq. 7.2 [1].

$$k_r(1\,MHz) = 1 + \Delta k_e + \Delta k_i + \Delta k_d \qquad (7.2)$$

The electronic contribution to the dielectric constant $(1+\Delta k_e)$ was measured with an ellipsometer at a wavelength of 633 nm or wavenumber of 15800 cm^{-1}. The results are shown in Fig. 7.8. The rise in dielectric constant is only 0.03 from 2 minutes to 36 minutes of exposure. The refractive index measurement is accurate to +/- 0.001.

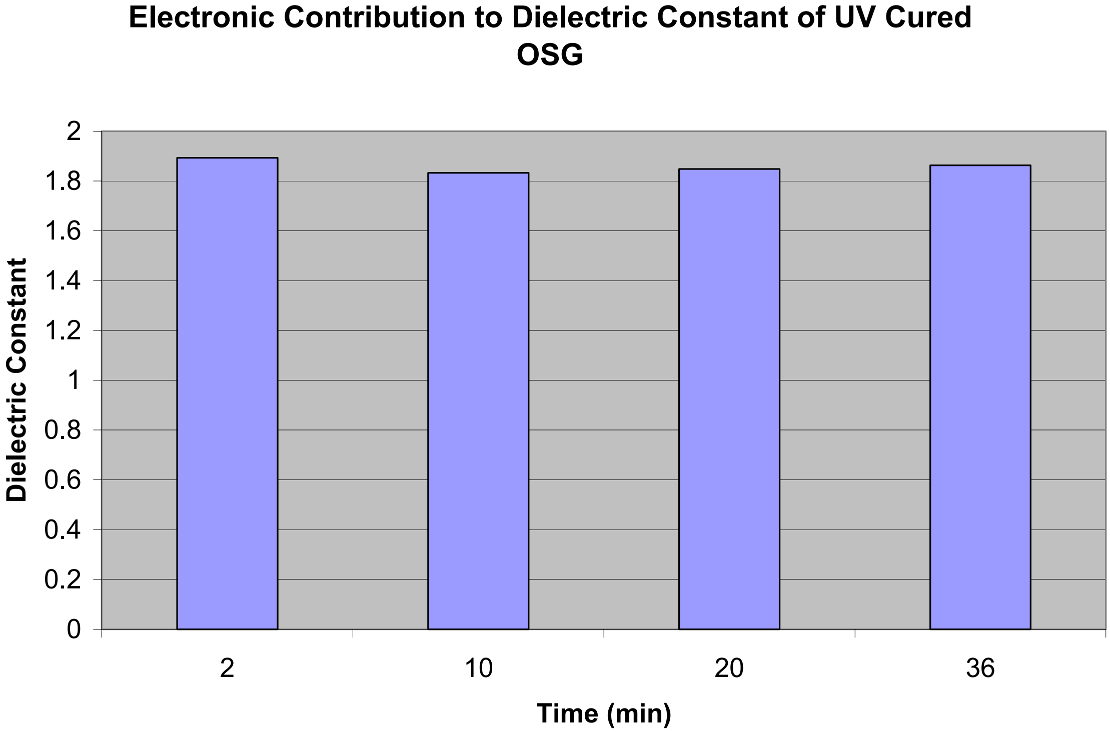

Figure 7.8 Electronic contribution to the dielectric constant as measured with an ellipsometer at 633 nm.

The ionic contribution to the dielectric constant can be calculated from the FTIR spectrum using the Kramers-Kronig relations from section 5.3.6. In section 5.3.6, an expression for the Kramers-Kronig relation was given and is reprinted here

$$n_i = n_{15800} + \frac{2}{\pi}\left[P\int_{\bar{\nu}_a}^{\bar{\nu}_b} \frac{\bar{\nu}\cdot\kappa(\bar{\nu})}{\bar{\nu}^2 - \bar{\nu}_i^2} d\bar{\nu} - P\int_{\bar{\nu}_a}^{\bar{\nu}_b} \frac{\bar{\nu}\cdot\kappa(\bar{\nu})}{\bar{\nu}^2 - (15800)^2} d\bar{\nu} \right] \tag{7.3}$$

where n_i is the refractive index at wavenumber v_i. The nomenclature P represents the “Principal Value” of the integral. The principal value is taken by excluding the region around the resonance point, v_i and 15800 cm^{-1}, and taking the limit of the excluded region. An example is shown in Eq. 7.4.

$$P\int_{\bar{v}_a}^{\bar{v}_b} \frac{\bar{v}\cdot\kappa(\bar{v})}{\bar{v}^2-\bar{v}_i^2}d\bar{v} = \lim_{\delta\to 0}\left(\int_{\bar{v}_a}^{\bar{v}_i-\delta} \frac{\bar{v}\cdot\kappa(\bar{v})}{\bar{v}^2-\bar{v}_i^2}d\bar{v} + \int_{\bar{v}_i+\delta}^{\bar{v}_b} \frac{\bar{v}\cdot\kappa(\bar{v})}{\bar{v}^2-\bar{v}_i^2}d\bar{v}\right) \tag{7.4}$$

The numerator of each integrand can be expressed in terms of the FTIR absorption spectrum.

$$\bar{v}\cdot\kappa(\bar{v}) = \frac{2.31\cdot A(\bar{v})}{4\pi\cdot d} \tag{7.5}$$

where $A(\bar{v})$ is the absorbance from the FTIR spectrum and d is the film thickness. An example spectrum is given in Fig. 7.9. Using Eq. 7.5, the integral in Eq. 7.4 can be expressed as

$$n_i = n_{15800} + \frac{2.31}{2\pi^2\cdot d}\left[P\int_{\bar{v}_a}^{\bar{v}_b} \frac{A(\bar{v})}{\bar{v}^2-\bar{v}_i^2}d\bar{v} - P\int_{\bar{v}_a}^{\bar{v}_b} \frac{A(\bar{v})}{\bar{v}^2-(15800)^2}d\bar{v}\right] \tag{7.6}$$

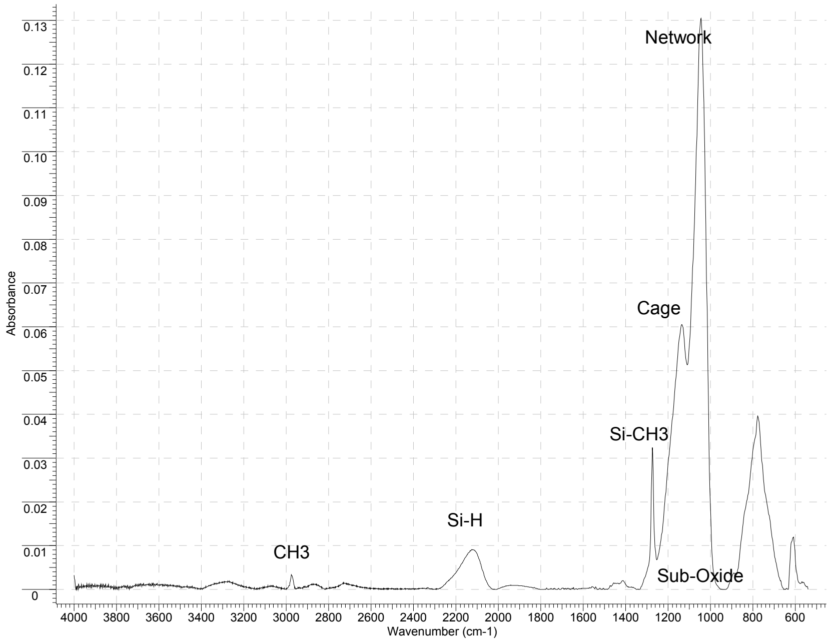

Figure 7.9 FTIR spectrum of OSG

The refractive index can be calculated by numerically integrating Eq. 7.6, using the absorbance values in Fig. 7.9. The numerical integration was performed in an Excel spreadsheet using the trapezoidal integration technique. In each integration, the "Principal Value" was taken by setting the integrand to zero for the wavenumber under consideration. The results of this integration are shown in Fig. 7.10. There are two important regions to review in Fig. 7.10. At low wavenumber, a plateau in the graph emerges. This plateau is the total refractive index at low wavenumbers. At high wavenumbers, another plateau develops and represents the asymptotic or electronic contribution to the refractive index. After converting the refractive index into the dielectric constant, the ionic contribution to the dielectric constant can by calculated by taking the difference between the low-wavenumber plateau in the dielectric constant and the asymptotic value at high wavenumbers. The ionic contribution to the dielectric

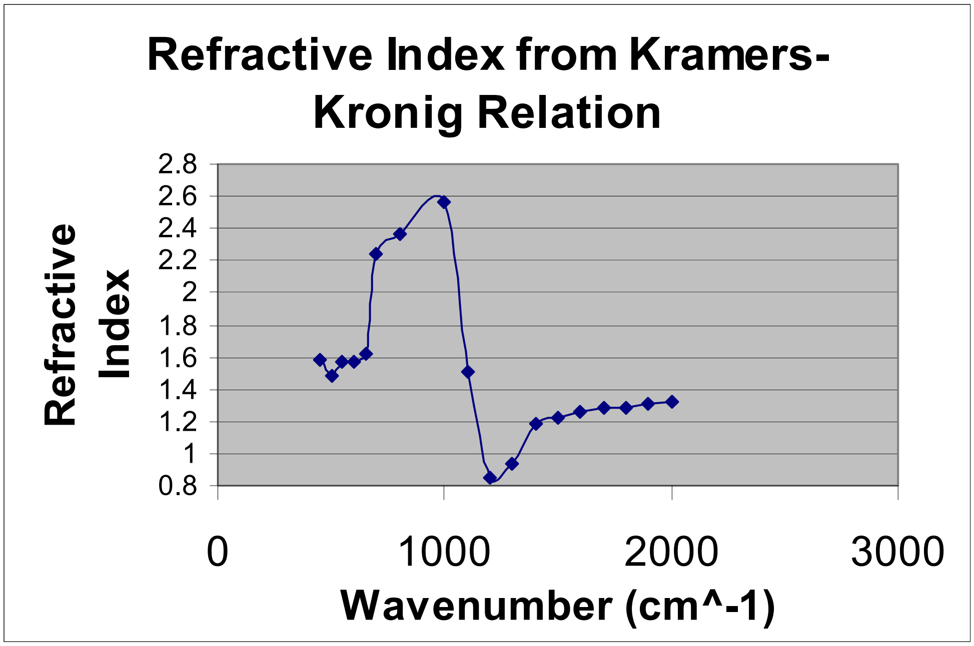

Figure 7.10 Refractive index calculation using the Kramers-Kronig relations.

constant is charted in Fig.7.11. It consistently increases with UV exposure. Although, the slope would appear small for the increase in ionic content, the spread in dielectric constant from two to thirty-six minutes of exposure is 0.2. This number is considerably larger than the increase in electronic contribution.

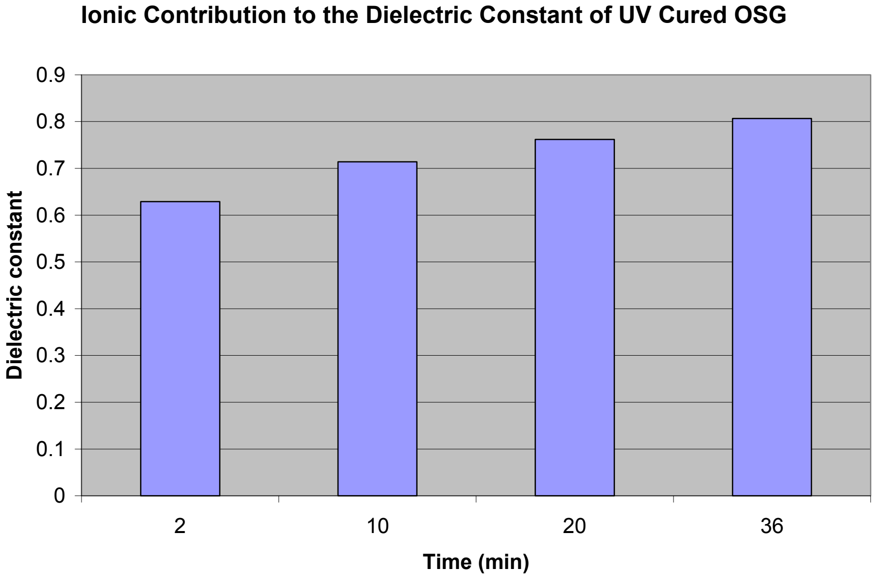

Figure 7.11 Ionic contribution to the total dielectric constant.

The sum of electronic and ionic contributions is a good fit to the total dielectric constant. Therefore, any dipolar contribution is negligible. The measured k-value at 1 MHz and the tabulated contributions from electronic and ionic polarizations to the total dielectric constant are shown in Table 7.2.

Table 7.2 Comparison between the k-value (1 MHz) and the sum of ionic and electronic contributions to the dielectric constant for different UV exposure times.

Time (min)	**k-Value (1 MHz)**	$1+\Delta k_e+\Delta k_i$
2	2.53	2.52
10	2.56	2.55
20	2.59	2.61
36	2.68	2.67

The Clausius-Mossotti equation (Eq. 2.16, section 2.2.2) [2], indicates that the dielectric constant is proportional to the polarizability. The Clausius-Mossotti equation is written again in Eq. 7.7.

$$\frac{k-1}{k+2} = \frac{4\pi}{3}\left(N_e \alpha_e + N_i \alpha_i\right) \tag{7.7}$$

where k is the dielectric constant, N_i is the number of dipoles per unit volume with polarizability α_i. Table 7.3 indicates that an increase in Si-O and Si-CH_2 molecules would increase the dielectric constant, specifically the ionic contribution.

Table 7.3. Table of polarizability/unit volume and bond energy for different molecular bonds [3-5].

Molecular Bond	**Polarizability/ Unit Volume**	**Bond Energy (eV)**
Si-O	**0.123**	**8.32**
Si-CH_3	**0.076**	**4.69****
Si-CH_2	**0.132**	**See above**
Si-H	**~0.07***	**<3.11**
C-H		**3.51**

*Assumes liquid density and wavelength of 538 nm.
**Bond energy for Si-C

7.3 FTIR investigation of molecular structure

The molecular structure of the UV cured ULK was further determined by Fourier Transform Infrared Spectroscopy (FTIR). As discussed in Chapter 5, the anti-symmetric stretch region for Si-O-Si stretches from 950 to 1250 cm^{-1} and is a convolution of network, cage and sub-oxide spectra. These sub-structures can be differentiated by the Si-O-Si bond angle. Network structures have a bond angle of ~144˚. The cage bond angle is ~150˚; while, the sub-oxide has a bond angle of <140˚. The peak positions for important molecular structures are given, again, in Table 7.4. Network, cage, and sub-oxide peaks can be found at 1060, 1135, and 1028 cm^{-1}. Methyl peaks occur at 800 (rocking), 1273 (bending), and 2970 (stretching) cm^{-1}. The primary methyl peak was at 1273 cm^{-1}. The silane peak (Si-H) can be found at ~ 2180 cm^{-1} and the silanol (Si-OH) peak is located between 3200 and 3700 cm^{-1} [4].

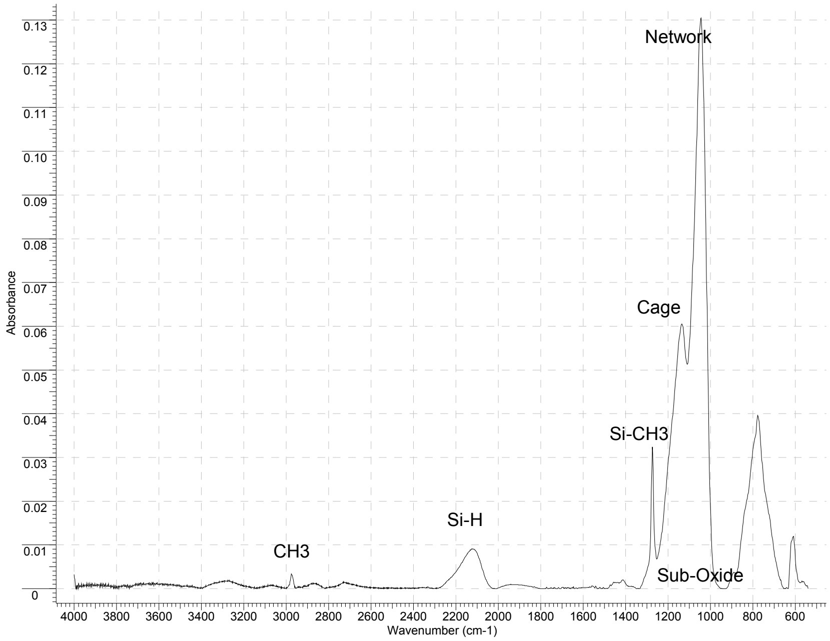

Figure 7.12 A typical FTIR Spectrum of OSG without SiCN cap-layer.

Table 7.4. FTIR peak positions.

Structure	Wavenumber (cm^{-1})
Si-OH	3200 - 3700
CH_3	2970
Si-H	2178
Si-CH_3	1273
Cage	1140
Network	1060
Sub-oxide	1023
SiC, CH_3	800

In Fig. 7.13, the bending region of the Si-CH_3 bond is examined more closely for clues to the connectivity of the OSG samples. There are two absorbance peaks in the range of 1270 cm^{-1}. The first peak is at 1274 cm^{-1} and the second at 1253 cm^{-1}. In section 5.3.4, the IR absorbance peaks for differently connected OSG units were discussed. The OSG films measured have both T and M groups, but later FTIR will show that only the T groups are affected by UV curing.

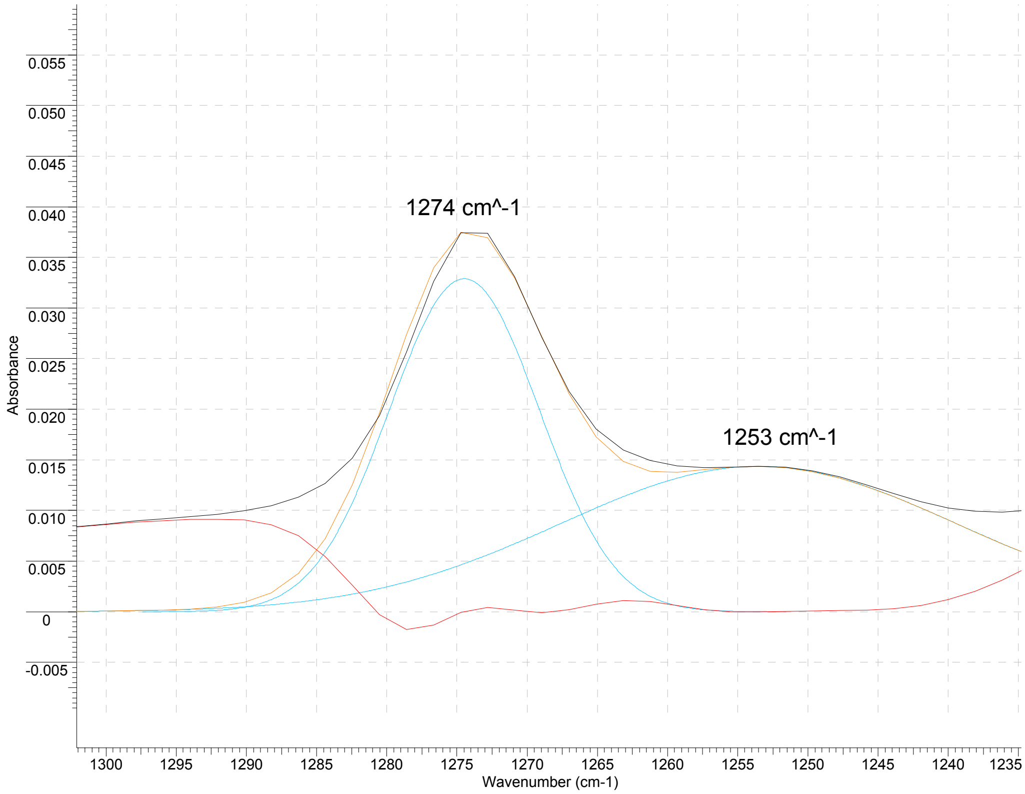

Figure 7.13 FTIR spectrum of Si-CH_3. Two absorption peaks are observed at 1274 cm^{-1} and at 1253 cm^{-1}.

In section 5.3.4, the spectral distribution of a UV cured sample was presented. The sample did not have a cap-layer of SiCN. The samples used in the fracture studies were Si/ULK (UV cured)/SiCN. The different spectra for the UV cured ULK/SiCN samples is presented in Fig. 7.14. These spectra are used for analysis, because they were the samples used in fracture studies. A good deconvolution of the spectra in Fig. 7.14 is

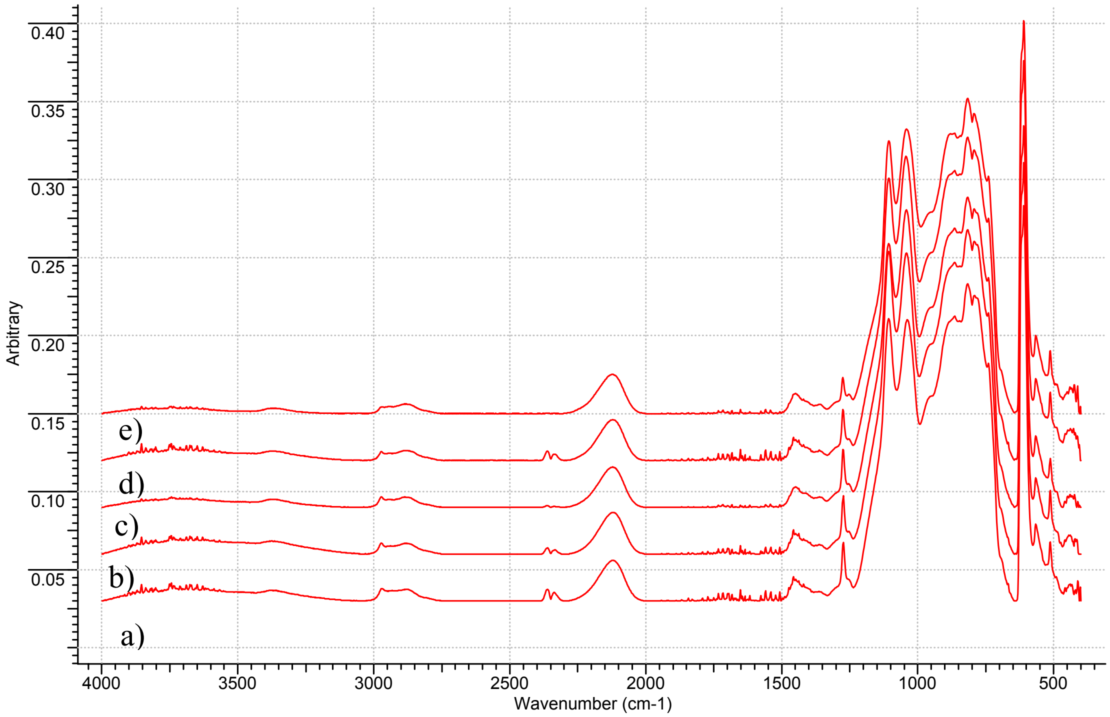

Figure 7.14 Spectrum of UV cured samples. The sample stack is Si/ULK/SiCN. Spectrum a) was not UV cured, b) was cured for 1 minutes, c) for 2 minutes, d) for 9 minutes, and e) for 36 minutes.

difficult to determine from these spectra, necessitating subtractive FTIR. The SiCN layer is a constant and should not contribute to the subtracted spectrum.

Fig. 7.15 demonstrates the differential spectrum, where the spectrum for no UV exposure was subtracted from the spectrum for a one minute exposure. Before a subtraction can be made, both spectra have to be fit to the same baseline. The baseline used was reported in Table 5.2. Differential spectra were calculated for one minute of UV exposure less that of no exposure, 2 minutes - 1 minute, 9 minutes – 2 minutes, and 36 minutes – 9 minutes. The spectra showed good peak areas for the major molecular structures—sub-oxide, network, cage, methyl, and silane. The subtraction result that is depicted in Fig. 7.15 indicates a decrease in methyl, cage, sub-oxide, and CH_x bonds. It also shows an increase in network and silane bonds. Close observation of the CH_x bonds in Fig. 7.15 proves that porogen was removed from the film during the first minute of UV cure. While the CH_3 peak (2970 cm^{-1}) continually decreases with UV exposure, the number of CH_x bonds (2930 cm^{-1} and 2875 cm^{-1}) remains constant after the first minute of UV cure. The loss of CH_x species indicates the removal of porogen.

Fig. 7.16 differentiates between an exposure of 36 minutes and 9 minutes. In Figs. 7.15 and 7.16, the methyl and cage structures decreased. The sub-oxide peak decreases with a one minute exposure; yet, increases during long exposures. The network trend is opposite.

The relative absorbance, charted in Fig. 7.17, was calculated from the subtractive spectra. The absorbance was calculated by taking the area under the curve for each molecular structure at each consecutive subtraction. The area under the curve for each subtraction was added to the previous results to obtain the change in relative absorbance with time, Fig. 7.17. The trend for methyl and cage are similar. Both continuously decrease with time. The network signal indicates an increase up to 9 minutes of exposure; but, the network signal decreases with long exposure to UV light. The sub-oxide peak is very interesting. It begins by decreasing before increasing in a manner similar to the density profile. Matsuura *et al.* noted a similar increase in sub-oxide with UV curing [6].

The decrease in methyl content is consistent with the XPS data in Fig. 7.6. And the loss of cage structures could be due to the collapse of the pores. Also, the only methyl absorbance peak that changes with UV cure is the T group.

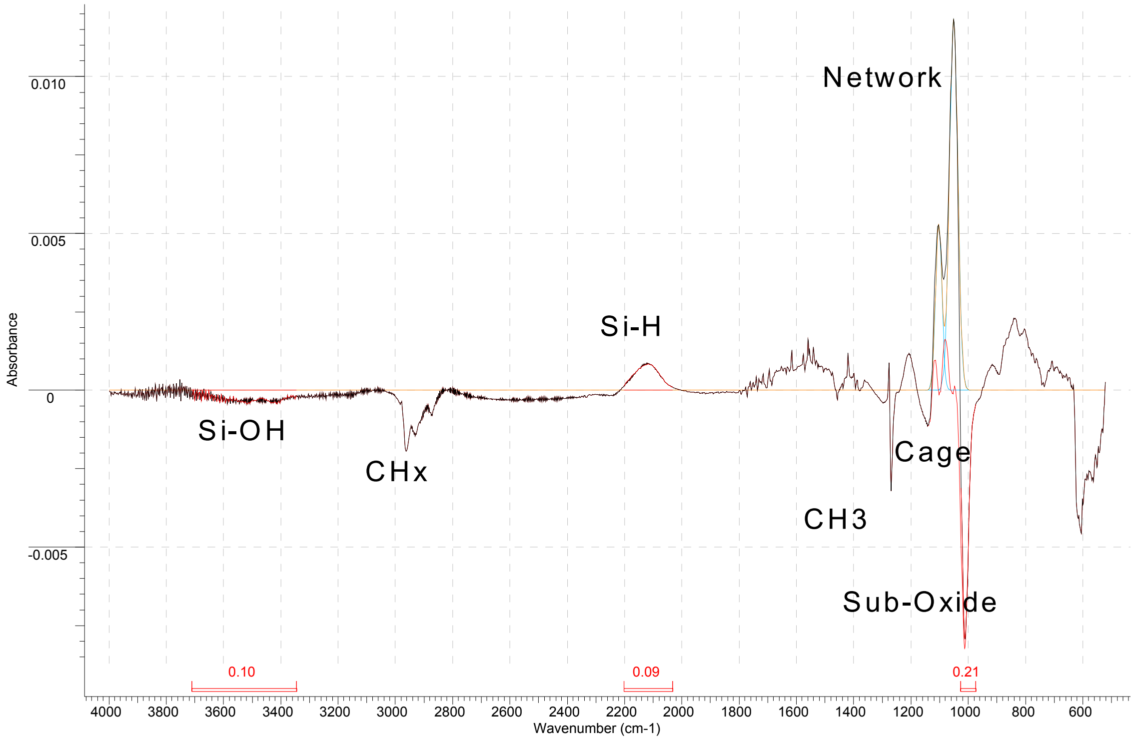

Figure 7.15 FTIR differential spectrum for one minute UV exposure less the spectrum for no cure.

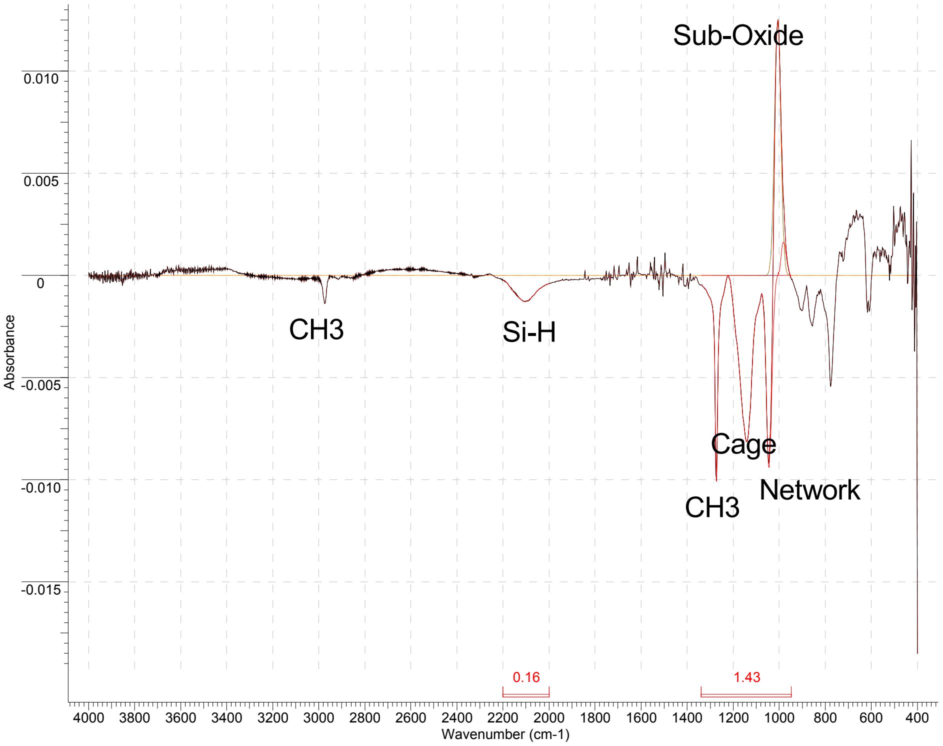

Figure 7.16 FTIR subtraction spectrum for 36 min. exposure less the 9 min. exposure.

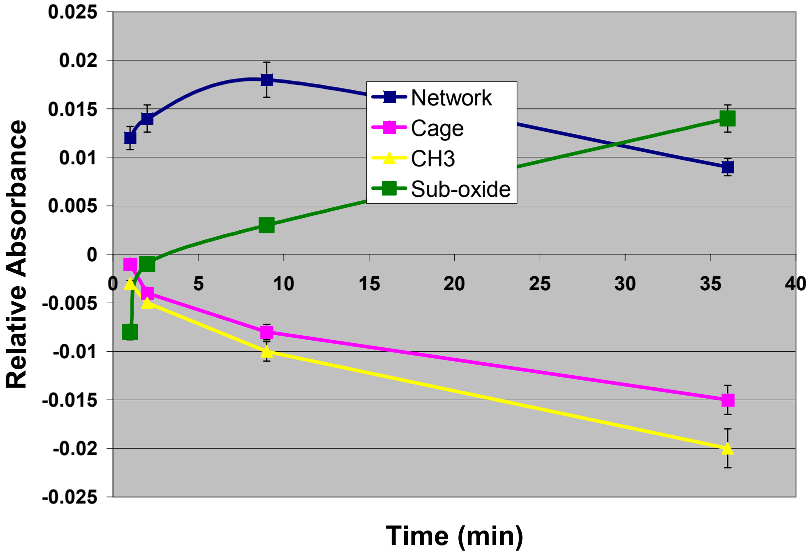

Figure 7.17 Relative absorbance for the principle sub-structures: network, cage, sub-oxide and methyl.

Figs. 7.18 and 7.19 chart the changes in the ratios of methyl/silicon-oxide and sub-oxide/silicon-oxide. The methyl content exponentially decreases with time; while, the sub-oxide linearly increases. The density and k-value as a function of hydrogen, methyl, and sub-oxide content are plotted in Figs. 7.20 and 7.21. Density and k-value are a decreasing function of hydrogen and methyl; while, both density and k-values increase with the sub-oxide content. The sub-oxide content is attributed to the termination of silicon dioxide with silicon, carbon, or hydrogen. Although the film is losing hydrogen and carbon, the rise in sub-oxide indicates that a condensation reaction occurred, increasing the number of silicon bonds with carbon or other silicon.

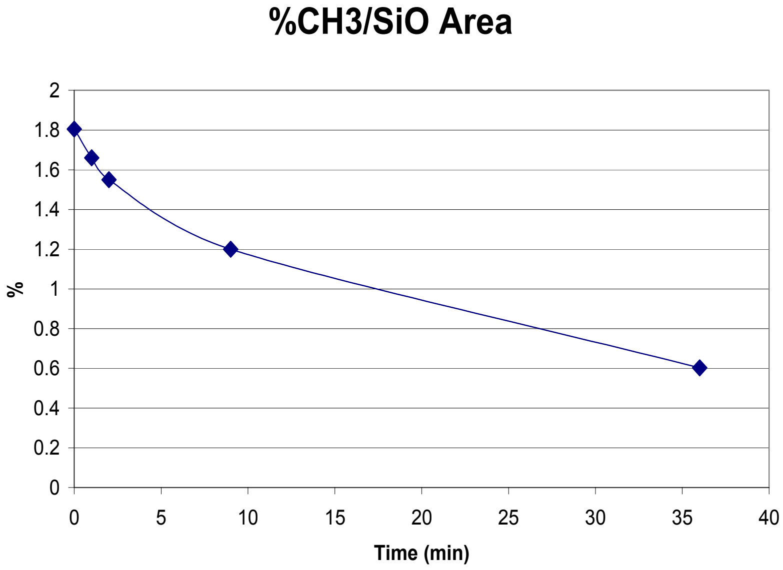

Figure 7.18 Percent methyl to SiO area.

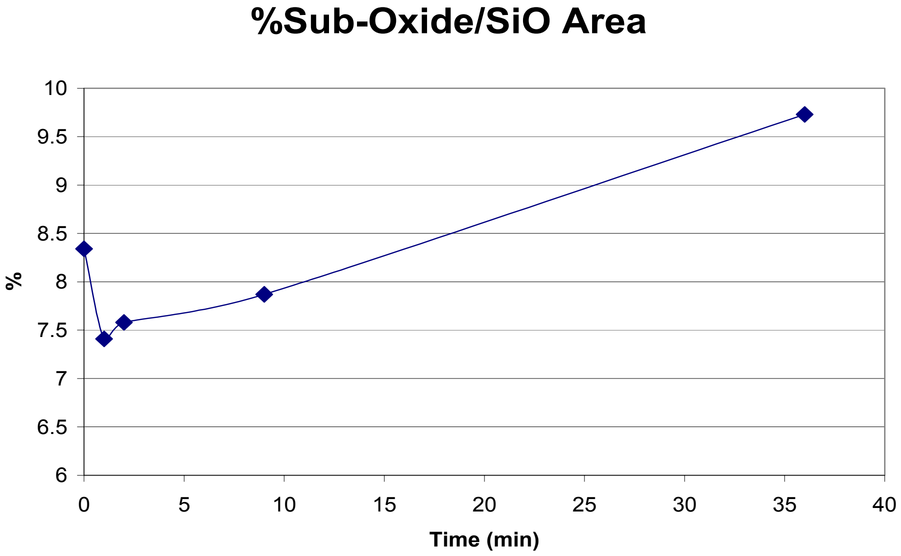

Figure 7.19 Percent sub-oxide to SiO area.

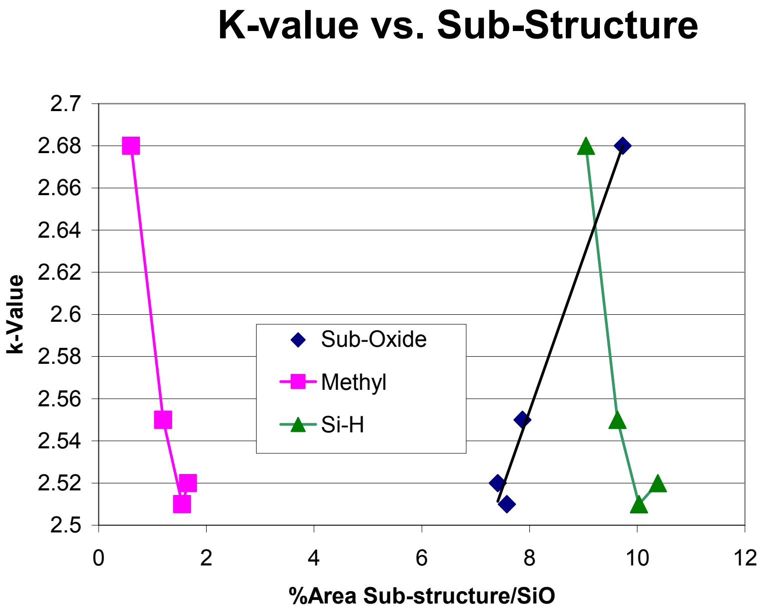

Figure 7.20 k-values as a function sub-structure content.

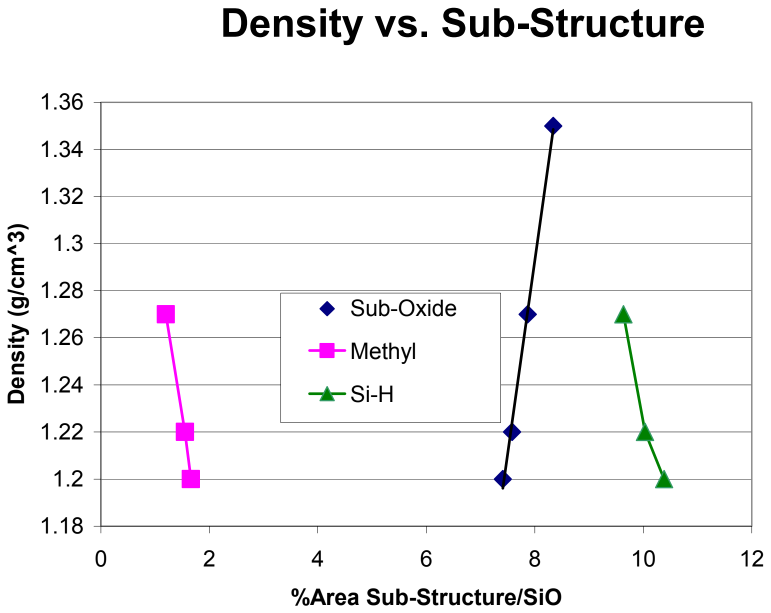

Figure 7.21 Density as a function of substructure content.

The following reaction paths for UV and the ULK at 400˚C are possible [7, 8].

$$\begin{aligned}
&i) -Si-CH_3 + H-Si- + \gamma \rightarrow -Si-CH_2-Si- + H_2\\
&ii) -Si-CH_3 + CH_3-Si- + \gamma \rightarrow -Si-C\equiv C-Si- + 3H_2\\
&iii) -Si-CH_3 + CH_3-Si- + \gamma \rightarrow -Si-CH=CH-Si- + H_2\\
&iv) -Si-CH_3 + CH_3-Si- + \gamma \rightarrow -Si-CH_2-Si- + CH_4\\
&v) -Si-CH_3 + OH-Si- + \gamma \rightarrow -Si-O-Si- + CH_4\\
&vi) -Si-CH_3 + H-Si- + \gamma \rightarrow -Si-Si- + CH_4\\
&vii) -Si-CH_3 + OH-Si- + \gamma \rightarrow -Si-CH_2-Si- + H_2O
\end{aligned} \tag{7.8}$$

The reaction paths in Eq. 7.8 are grouped according to bond energy. In reactions i) to iii), the energy necessary to break the C-H bond is 3.51 eV. The energy to break the Si-C bonds in reactions iv) to vi) is 4.69 eV. Finally, the Si-O bond energy in vii) is 8.32 eV. Unfortunately, reactions ii) and iii) can not be measured by FTIR, nor can reaction vi). However, reaction v) can be measured. The increase in Si-O-Si bonds can be measured with FTIR and Fig. 7.17 indicates an increase in this bond. Also, Figs. 7.17 and 7.19-21 show an increase in sub-oxide content. Of the reactions in 7.8, reactions i), iv), vi) and vii) would increase the sub-oxide content. Reaction vii) is highly unlikely, as the bond energy is high. The absorbance spectrum of Si-CH_2-Si is in the same region as Si-O-Si, and therefore not distinguishable; however, it also has a weak peak at 2930 cm^{-1}. Strong indirect evidence is the increase in sub-oxide structures in the film. The loss of carbon (as measured by XPS) and hydrogen (FTIR) reduces the list of reactions to i), iv), v), and vi). Reaction i) is most energetically favored; while reaction iv), v) and vi) may occur with the same frequency.

The reactions i) and iv)-vi) increase the connectivity of silicon; increase the density; and, with the exception of reaction v), increase the ionic contribution to the dielectric constant. In each case, a terminating group is replaced by a bridging molecule. The bridge increases the number of connecting bonds in the molecular structure and, thereby, increases the rigidity and fracture toughness. The increase in density can be seen by the decrease in molar volume, presented in Table 7.5. Each reaction product has a significant ionic polarizability.

Table 7.5 The change in volume and density for given reaction paths.

Reaction	**% Decrease in Molar Volume (mol/cm^3)**	**% Density Increase (g/cm^3)**
i)	21	22.1
iv)	31	27.5
v)	29	24.2
vi)	34	30.3

7.4 Summary

Chapter 7 discussed the changes in material properties of a k~2.5 OSG ultra low-k dielectric with UV curing. The density and dielectric constant increased with UV exposure. The increase in dielectric constant was broken down to insignificant increases in the electronic contribution and more significant ionic contribution. The increase in both density and dielectric constant were attributed to a decrease in carbon within the film by the production of methane. The evolution of the molecular structure with UV curing was measured by FTIR. In particular, the network, cage, sub-oxide, and hydrogen content of the OSG film were measured. It was found that the cage, methyl, and hydrogen content continually decreased with UV exposure; while, network and sub-oxide content increased. The position of the methyl absorbance peak indicated the film had a T group connectivity. A list of possible condensation reactions was discussed and the reactions deemed most probable produced methane and hydrogen. The reactions also produced bridging connections to other OSG groups. The bridging led to an increase in bond density and mass density.

An increase in bond density should lead to an increase in fracture toughness. The effect of UV curing on fracture toughness is discussed in Chapter 8.

Chapter 8 Results: Part II, fracture toughness

In Chapter 8, the second part of the results section, the effect of UV curing on the fracture properties of the low-k film will be investigated. It will be shown that UV curing increases the critical fracture energy for all mode-mixes, and the crack location was found to be cohesive for all cracks. However, the sub-critical fracture toughness was insensitive to UV curing. The difference is explained by the nucleation of voids and coalescence of micro-cracks with the main crack during sub-critical crack growth. Void nucleation and coalescence during sub-critical fracture of silica were recently demonstrated by Bonamy *et al*. [1].

8.1 Experimental procedures

The fracture toughness of the ULK/SiCN interface was investigated using the Four Point Bend Flexure (4pt-bend) and Mixed-Mode Double Cantilever Beam (MMDCB) techniques. The 4pt-bend was used to measure critical fracture toughness; while, sub-critical and multi-phase angle critical fracture were measured with the MMDCB. Both 4pt-bend and MMDCB samples are made from a sandwich structure. The film stack for the sandwich structure was presented in Fig. 6.1. It is reprinted here in Fig. 8.1.

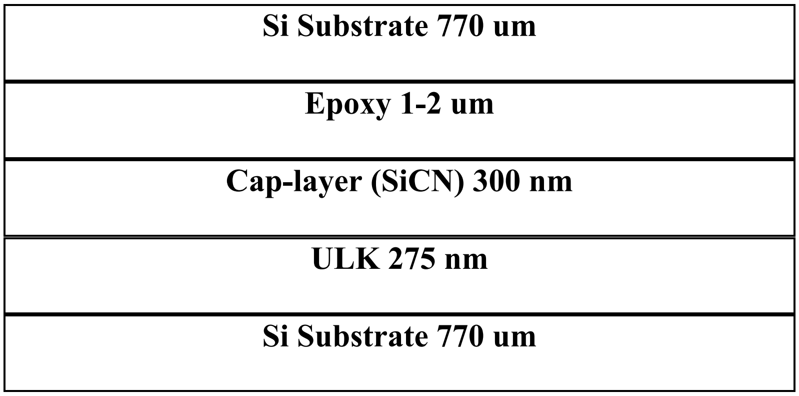

Figure 8.1 Film stack for sandwich samples

The 4pt-bend is illustrated in Fig. 8.2. The crack was initiated from the notch in the top silicon plank. It traveled normal to the interface and, upon reaching the low-k layer, diverted its path into that layer. While the crack remained between the interior nodes, the crack driving force and phase angle were constant. The equation for the driving force or strain-energy release rate is

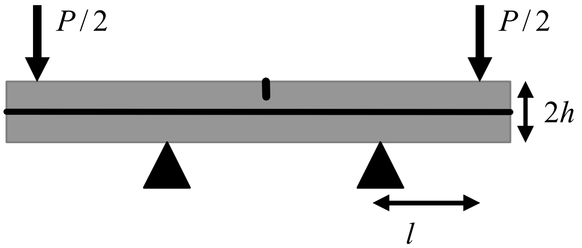

Fig. 8.2 Diagram of the Four-Point Bend Technique.

$$G = \frac{21\left(1-\nu^2\right)P^2 l^2}{16Eb^2h^3} \tag{8.1}$$

where *P* is the load, *l* the torque arm, *b* the sample width, and *h* is the half height. The mechanical properties *E* and *v* are the Young's Modulus and Poisson's Ratio, respectively. The experiment and sample preparation have been previously explained in sections 6.1 and 6.2. The Mixed Mode Double Cantilever Beam, which consists of a load jig with several pivot points, was also used for steady-state fracture studies at different phase angles. The MMDCB was also discussed in Chapter 6, section 6.3. The phase angle for the Four-Point Bend is ~42°. The pin spacing was adjusted, Fig. 6.6, such that the MMDCB phase angle was zero, 15°, or 32°.

Sub-critical crack growth was induced by static displacement in the Mixed Mode Double Cantilever Beam, as discussed in section 6.4. The MMDCB was loaded in Mode I until the beginning of critical fracture and stopped. The crack velocity was calculated from the compliance.

$$da/dt = -\frac{a_0}{3F}\frac{dF}{dt} \qquad (8.2)$$

where a_0 was the initial crack length and *F* was the applied load. All sub-critical crack growth experiments were performed in a controlled atmosphere. The humidity limits of the chamber were 10% to 85% +/- 4% RH. The ambient temperature was $\sim 23^\circ C$.

The location, interface or cohesive, of the fracture surface was determined by XPS.

8.2 Critical fracture

The critical fracture toughness of the ULK for different mode-mixes is presented in Fig. 8.3. The phase angle of the four point bend measurement is ~ 42°. Although the crack was close to the interface, XPS results indicate that the fracture was cohesive for all mode mixes, Fig. 8.4. Fig. 8.3 charts the fracture toughness as a function of the film density. The Mode I toughness grows linearly with density; while, the mixed-mode toughness deviates from linearity. The data point at 1.35 g/cm^3 corresponds to thermal cure only. The transition from 1.35 g/cm^3 to 1.2 g/cm^3 is due to porogen removal. The deviation from linearity suggests that inelastic processes affect the strain energy release rate above 2 J/m^2.

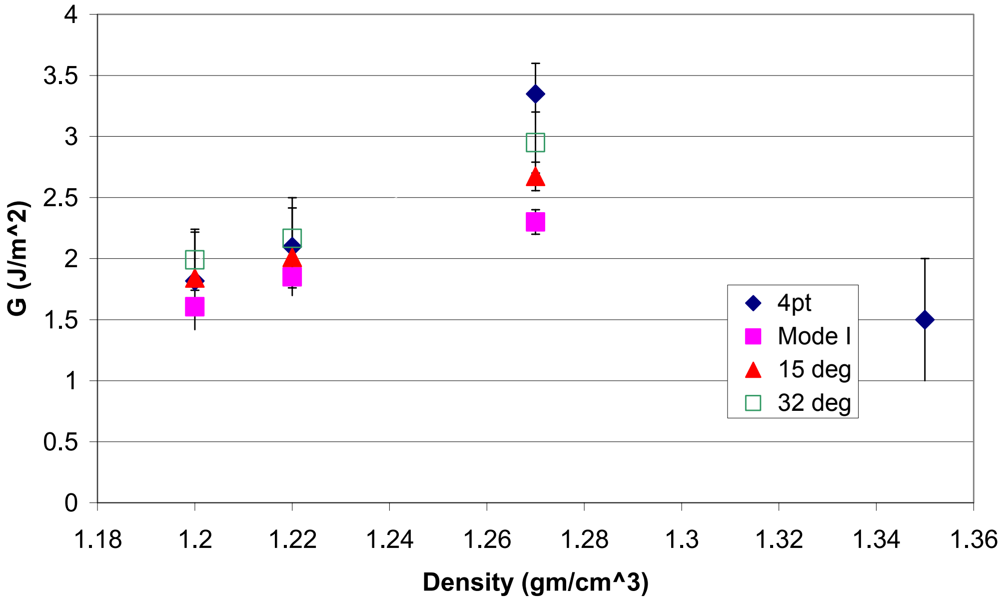

Figure 8.3 Four-point Bend and Mixed-mode fracture toughness relationship to film density (g/cm^3).

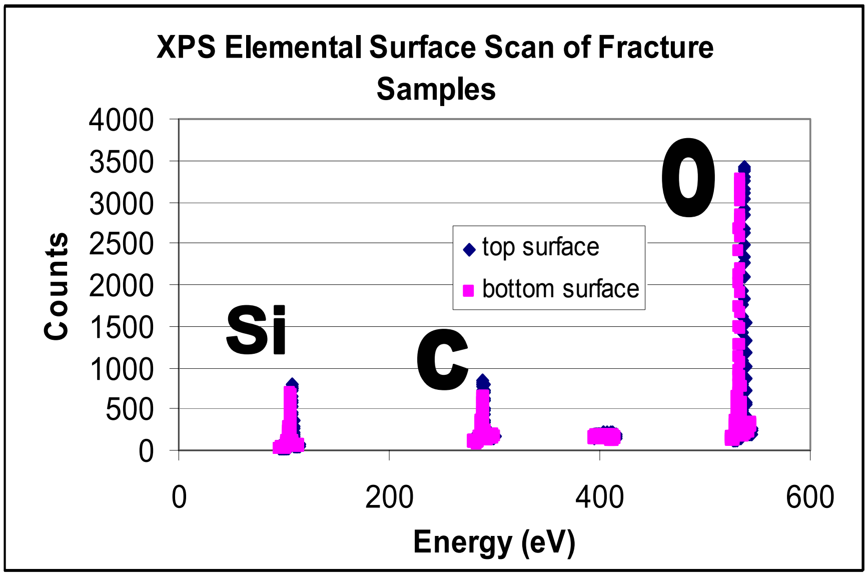

Figure 8.4 XPS elemental surface scan of fracture surfaces.

8.3 Sub-critical fracture

Sub-critical fracture toughness was measured by the Mixed Mode Double Cantilever Beam system loaded in Mode I configuration. As described in the section 6.4, the samples were loaded at 10 um/s to critical failure and stopped. The subsequent sub-critical fracture occurred at static displacement. The crack velocity was calculated from the sample compliance, Eq. 8.2.

Sub-critical fracture was discussed in section 4.4. The three regimes of sub-critical fracture were presented. Also, the analysis of stress corrosion was presented. Sub-critical crack growth measurements are displayed in Figs. 8.5 and 8.6. Each figure charts the results of a test at constant UV cure exposure and different relative humidity.

The samples represented in Fig. 8.5 were not exposed to UV light. The samples represented in Fig. 8.6 were UV cured for thirty-six minutes

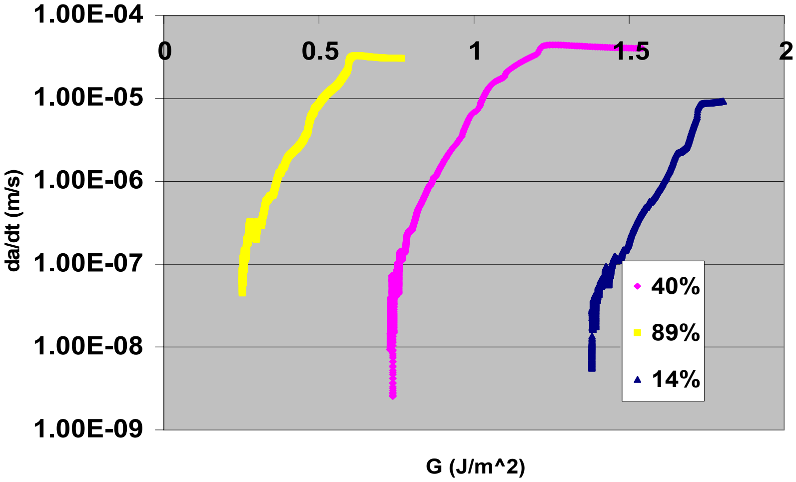

Figure 8.5 Sub-critical fracture at multiple relative humidities and no UV exposure.

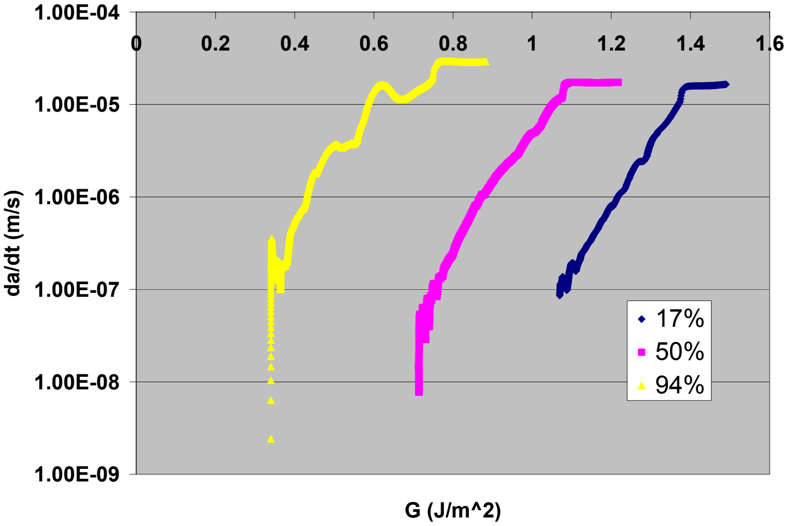

Figure 8.6 Sub-critical fracture at multiple relative humidities and 36 minutes UV exposure.

8.4 Discussion

8.4.1 Critical fracture and the contributions of inelastic processes

The critical fracture that was shown in Fig. 8.3 demonstrates a dependence on low-k density and subsequently UV exposure. The fracture energy does not indicate a dependence on mode-mix below 2 J/m^2. Above 2 J/m^2, the fracture toughness monotonically increased with mode-mix. The linear increase with density in Mode I can be directly related to the linear increase in sub-oxide bonds in section 7.3, Figs. 7.19 to 7.21. The possible bridging bonds were presented in Eq. 7.8. The bridging bonds were shown to reduce to the following possibilities in Eq. 8.3. The increase in bridging bonds should also increase the number of broken bonds on the crack surface. This increase in broken bonds raises the surface free energy and consequently the fracture toughness.

$$\begin{aligned}
&i) - Si - CH_3 + H - Si - + \gamma \rightarrow -Si - CH_2 - Si - + H_2 \\
&ii) - Si - CH_3 + CH_3 - Si - + \gamma \rightarrow -Si - CH_2 - Si - + CH_4 \\
&iii) - Si - CH_3 + OH - Si - + \gamma \rightarrow -Si - O - Si - + CH_4 \\
&iv) - Si - CH_3 + H - Si - + \gamma \rightarrow -Si - Si - + CH_4
\end{aligned} \tag{8.3}$$

The plastic contribution to the fracture toughness by the epoxy layer was calculated in ABAQUS 6.6 (under academic license from Hibbitt, Karlsson, and Sorensen, Inc.) with two material responses—elastic and strain hardening. The ABAQUS model consisted of two silicon planks of 1 mm thickness, bonded together with a 5 micron epoxy layer. The crack was placed at the bottom epoxy/silicon interface. For the elastic analysis, the modulus was taken to be 4 GPa and Poisson’s ratio was 0.3. For the strain hardening model, the material response of the epoxy was taken directly from the stress-strain curve in Fig. 8.7.

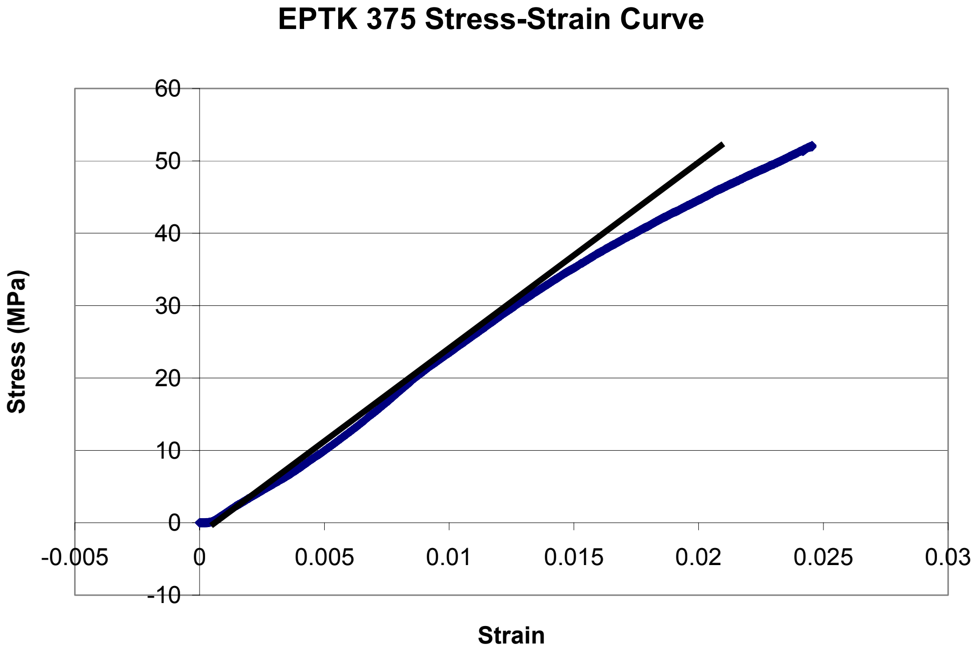

Figure 8.7 The stress-strain curve for epoxy, Epotek 375.

The yield stress was taken to be 30 MPa, where the curve in Fig. 8.7 deviates from linearity. The plastic contribution to the fracture toughness was calculated by comparing the J-integral analysis of the elastic and strain-hardening models. The J-integral was calculated in ABAQUS 6.6 using a packaged program. The results are shown in Fig. 8.8. The results indicate that plasticity is not responsible for the increase in fracture toughness with mode-mix in Fig. 8.3.

Another possible contribution to the fracture toughness is asperity. Asperity was discussed in section 4.3.5.2. The surface roughness for 4pt-bend samples with different curing times is plotted in Fig. 8.9. The roughness is essentially constant with a slight rise at thirty-six minutes of UV exposure. The fracture toughness should increase with roughness due to asperity and an increase in surface area. The shielding parameter, χ, is

1.8, indicating that some asperity shielding is possible (see section 4.3.5.2), although the fracture toughness does not strictly follow the prediction of Evans and Hutchinson [2].

$$\Gamma_i = \Gamma_0 \left(1 + \tan^2 \psi\right) \tag{8.4}$$

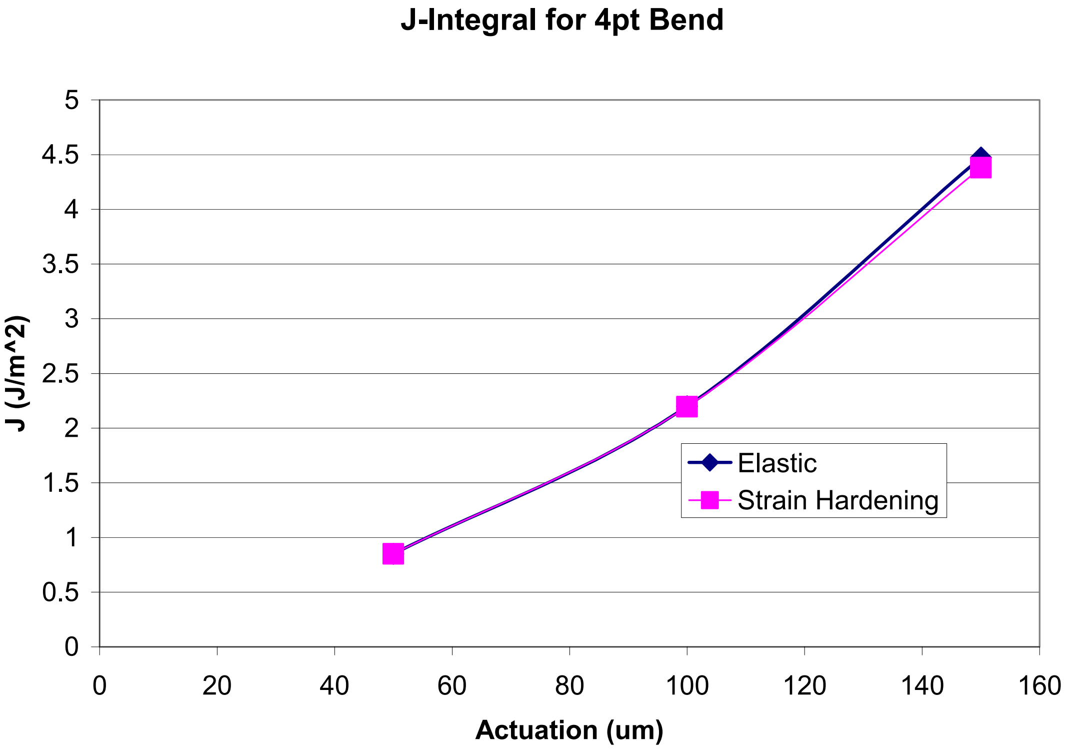

Figure 8.8 J-Integral calculations for an elastic and strain-hardening epoxy resin.

8.4.2 The phase angle and crack location

XPS measurements of all critical fractures, regardless of mode-mix, indicated cohesive failure. However, the crack was very close to the interface. Although the mode mix for a cohesive crack in the bulk material must be locally Mode I, a crack close to and paralleling the interface must approach the mode mix of the interface [12]. During the change from 4pt bend, phase angle of 42°, to Mode I, the crack location moved 60 nm toward the film interior. The change in crack location was measured with a Tencor Alpha Step 200.

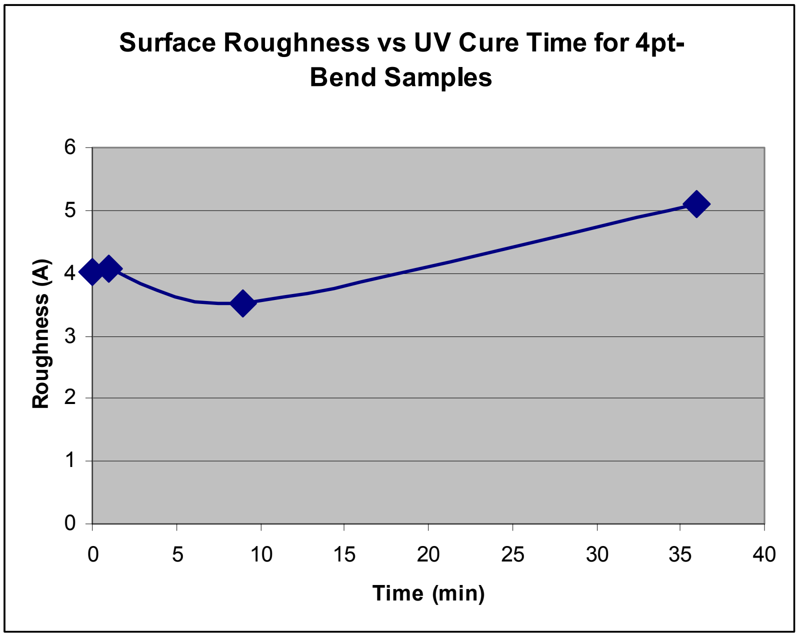

Figure 8.9 AFM surface roughness measurements.

8.4.3 Sub-critical crack growth and UV curing

The sub-critical fracture of the OSG films are charted in Figs. 8.10, 8.11, and 8.12. The velocity curves in Fig. 8.10 are the benchmark tests. The relative humidity was held at a constant 46% for all sub-critical experiments shown in Fig. 8.10. The sub-critical velocity curves for an average relative humidity of 87% and 15% are shown in Figs. 8.11 and 8.12, respectively. The major conclusion of these experiments is that sub-critical fracture in these p-OSG films was insensitive to UV exposure.

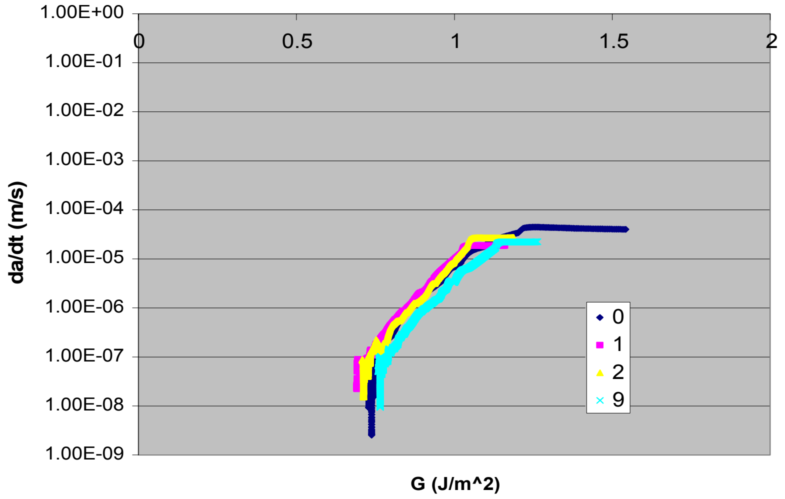

Figure 8.10 Sub-critical velocity curves for UV cured OSG at a constant RH of 46%

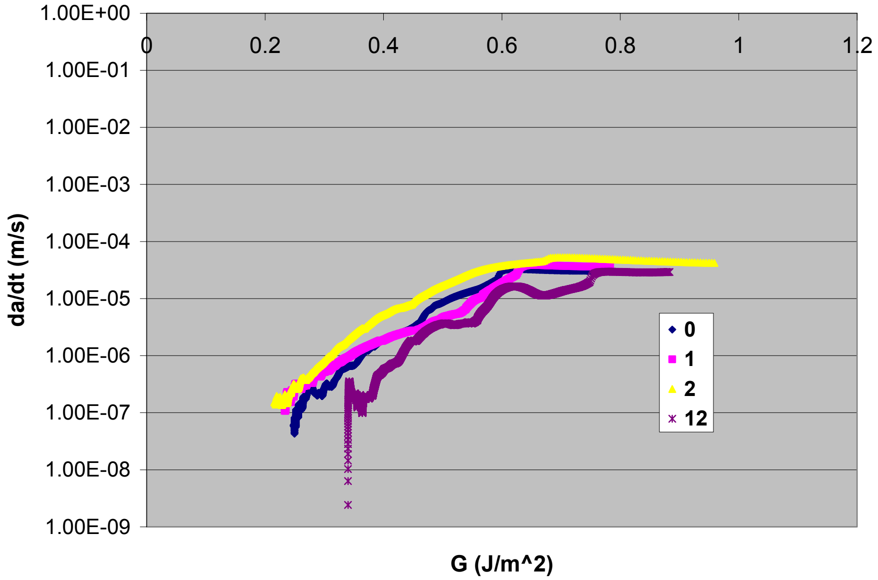

Figure 8.11 Sub-critical velocity curves for UV cured OSG for an average RH of 87%

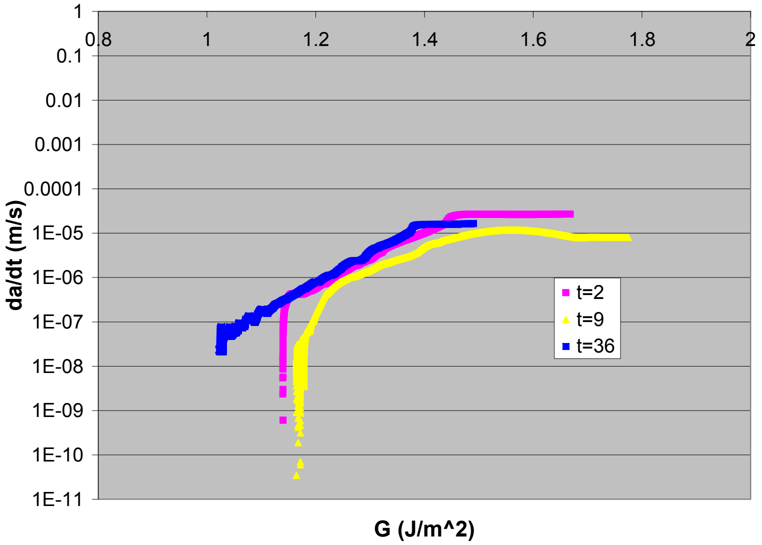

Figure 8.12 Sub-critical velocity curves for UV cured OSG for an average RH of 15%

Sub-critical fracture can be explained by the ideal curve in Fig. 4.10. The crack velocity in the reaction controlled region, or Region I, can be expressed as [3]

$$v = v_0 * Sinh\left(\frac{G-\Gamma}{2NkT}\right) \quad (8.5)$$

where *G* is the strain-energy release rate, *Γ* is the threshold fracture toughness, and *N* is the surface bond density. *T* and *k* are temperature and Boltzman's constant, respectively. From the slope of the velocity in Region I, we can calculate the surface bond density, *N*. The results (displayed in Fig. 8.13) indicate that the surface bond density is roughly constant for all UV exposures. If that reaction is between silicon dioxide and water, the reaction can be specified as follows [4, 5]

$$-\mathrm{Si}-\mathrm{O}-\mathrm{Si}+\mathrm{H_2O} \rightarrow -\mathrm{Si}-\mathrm{OH}+\mathrm{HO}-\mathrm{Si}- \quad (8.6)$$

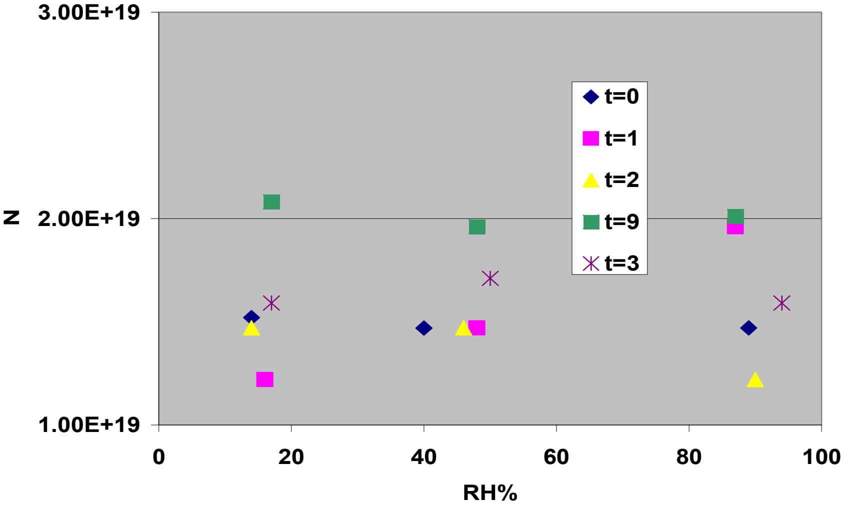

Figure 8.13 Calculated surface bond densities for different UV exposures.

Generally, the reaction is mediated by an activated complex whose decay products are displayed on the right hand side of Eq. 8.6. Furthermore, the bond rupture energy is related to the threshold fracture toughness through the following equations [6]

$$\begin{aligned} \Gamma &= N(\mu_{Si-O*} - \mu_{Si-O}) - N\mu_{H_2O} = Nu_0 \\ \mu_{H_2O} &= \mu^0_{H_2O} + kT\ln(P_{H_2O}) \end{aligned} \tag{8.7}$$

The threshold fracture toughness and the corresponding bond rupture energy are displayed in Figs. 8.14 and 8.15. Both charts indicated a linear dependence on the relative humidity. At 46% relative humidity, the bond rupture energy is ~ 0.29 eV. This value is lower than a previously reported value of 0.45 eV for silicon dioxide [7].

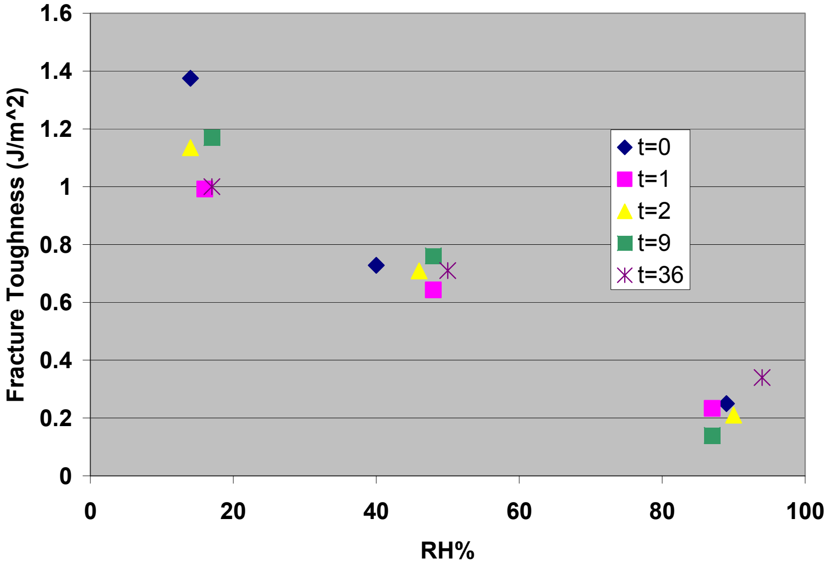

Figure 8.14 Threshold fracture toughness as a function of relative humidity.

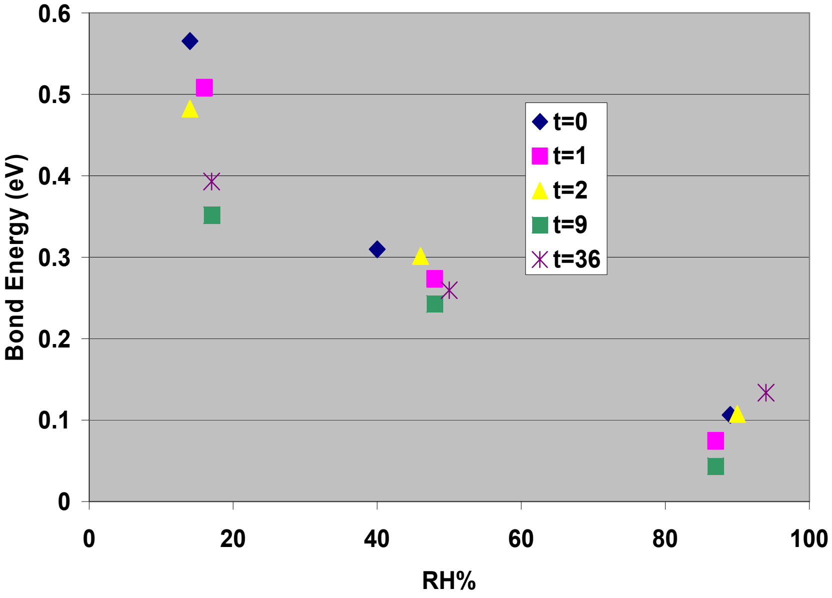

Figure 8.15 Bond rupture energy as a function of relative humidity

8.4.4 Reaction kinetics, void nucleation, and sub-critical crack propagation

At the present time, a complete explanation for the difference in critical and sub-critical fracture after UV curing is not available. Yet, a plausible argument can be made, using reaction rate kinetics and recent discoveries about sub-critical fracture in silica glass. Previously, silica glass was considered the "archetype brittle material [1]." Recent experiments and molecular dynamics (MD) simulations, have shown that glass has inelastic behavior at the nano-scale. Particularly, silica glass exhibits void nucleation and coalescence during sub-critical fracture [1].

The reaction of the crack tip with water was discussed in section 8.4.3. The crack velocity was related to the bond density and threshold fracture toughness; yet, the insensitivity to UV was not explained. An increase in Si-CH2-Si bonds was discussed in section 8.4.3, Eq 8.5. The increase in bridging bonds should also increase the fracture toughness, but sub-critical fracture is dependent on reaction rates at the crack tip. A kinetic theory is needed. Suppose that there are two molecular species at the crack tip, Si-O-Si and Si-CH2-Si. The reaction paths with water are given in Eq. 8.8 [4, 8, 9]

$$\begin{aligned} &-Si-O-Si-+H_2O \rightarrow -Si-OH \; + \; HO-Si- \\ &-Si-CH_2-Si-+H_2O \rightarrow -Si-O-Si-+ \; CH_4 \end{aligned} \tag{8.8}$$

The concentration of silica bonds needs to be understood better. The limiting reaction is silica to silanol; yet, the second reaction in 8.8 would appear to increase the silica bonds. The reactions in Eq. 8.8 may be considered first order reactions since there is an excess of water [10]. Let the methylene bond, Si-CH2-Si, have a reaction rate of k_1 with water and the silica bonds, Si-O-Si, have a reaction rate of k_2, where k_2 is greater than k_1. The time dependence of the Si-O-Si concentration can be written [10].

$$[Si-O-Si]=\left([Si-O-Si]_0+[Si-CH_2-Si]_0\cdot\left(\frac{k_1}{k_1+k_2}\right)\cdot(\exp((k_2-k_1)\cdot t)-1)\right)\cdot\exp(-k_2\cdot t) \qquad (8.9)$$

A graph of Eq. 8.9 is shown in Fig.8.16. The reaction rate k_2 is equal to $1.5*k_1$.

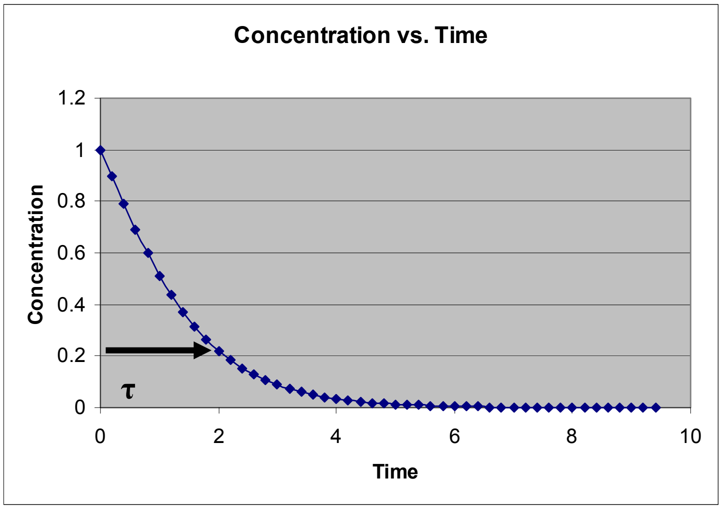

Figure 8.16 Concentration of Si-O-Si as a function of time (arbitrary units).

A natural time scale, τ, arises in the problem. The time scale, τ, will be revisited after a discussion of void nucleation and coalescence.

Bonamy et al [1] have recently, experimentally demonstrated that sub-critical fracture of silica occurs through void nucleation and coalescence with the main crack tip. An in-situ measurement was made with an atomic force microscope during sub-critical fracture. A picture of the AFM image is given in Fig. 8.17. In front of the crack tip, the stresses are sufficient to cause stress-corrosion reactions with water that has diffused ahead of the main crack. The reactions create a void that grows into a micro-crack. Eventually, the micro-crack is sufficiently large that it coalesces with the main crack. The process zone for void nucleation and coalescence shrinks with crack tip velocity. For instance, the process zone is found to be ~300 nm for a velocity of 10^{-9} m/s, while the process zone shrank to 10-25 nm for a velocity of 4 m/s. As the process zone shrinks, the fracture toughness becomes a function of density; whereas, during sub-critical fracture the density of activated sites that lead to voiding are more influential. The results for silica can be translated to silica based low-k films. According to molecular dynamics simulations, the requirement for void nucleation is a non-uniform density in the film [11].

Assume that the micro-crack has a length, d, and the sub-critical crack has velocity, v. The requirement that the methylene content does not affect crack velocity is that $\tau \leq \frac{d}{v}$.

The model of reaction rate kinetics and void nucleation is a plausible argument. The actual mechanism is unknown. The plausibility argument loses ground in light of the bond density in Fig. 8.13. The bond density is essentially constant for all UV exposures. If this is true, there is no need for a plausibility argument. The same number of bonds is broken for all UV exposures and the sub-critical reaction rate should be constant.

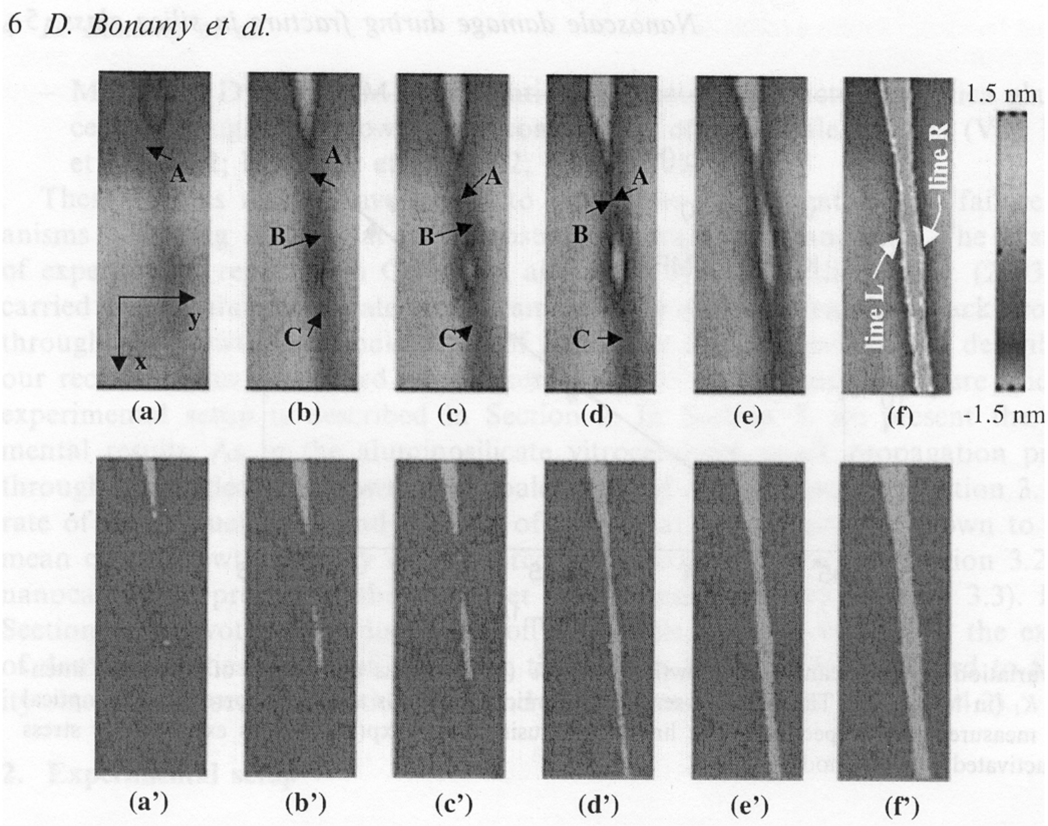

Figure 8.17 In-situ AFM measurement of sub-critical crack growth in silicon dioxide [1].

Although UV cure has no effect on sub-critical fracture, it still provides a benefit to the low-k stack structure. The benefit can be understood by using a simple fracture model. Consider a large sheet of material, remotely loaded in one direction, with a center crack of length *2a*, Fig. 8.18. The elastic solution for this problem is:

$$G = \frac{\pi\left(1-\nu^2\right)P_0^2 a}{E} \tag{8.10}$$

where E is the modulus, ν is Poisson's Ratio, P_0 is the remote load per unit area, and a is half the crack length. The relationship between the critical strain-energy release rate and the critical crack length is linear. Suppose that a crack in the ILD stack has insufficient length to critically rupture, but it may grow sub-critically. The critical length increases with UV exposure (Fig. 8.3). Thus, the time to failure increases proportionately with UV exposure.

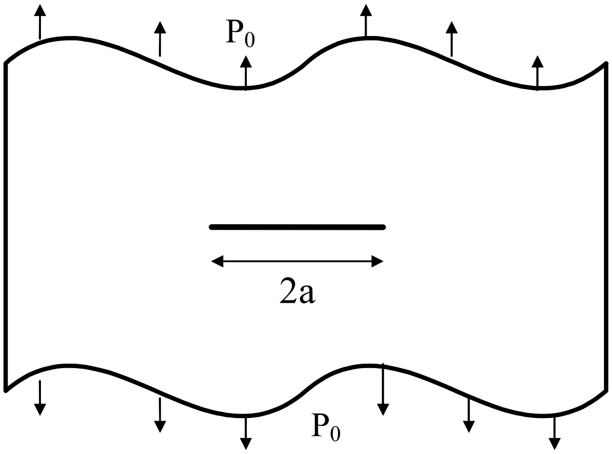

Figure 8.18 Center crack in a large sheet of material with modulus, E, and Poisson's ration, ν, and crack length 2a.

8.5 Summary

UV curing of an organosilicate glass significantly changes the molecular structure of the thin film, in a beneficial manner. The decrease of methyl and variability of sub-oxide content led to a change in k-value and density of the material. The critical fracture toughness increased with density and consequently UV exposure. The critical fracture toughness was independent of the mode-mix below 2 J/m^2 and increased monotonically with mode-mix above 2 J/m^2. The increase in fracture toughness with mode-mix was attributed to asperity. Interestingly, the sub-critical fracture toughness was insensitive to UV. A simple reaction kinetics model was proposed to account for the insensitivity.

However, the net effect of UV curing is an increase in the time to failure of cracks in the inter-layer dielectric.

Chapter 9 Summary and future work

9.1 Summary

The objectives of this dissertation were to investigate the effects of UV curing on the molecular structure and fracture properties of an ultra low-k dielectric, k~2.5. The results of this research were presented in two parts—the effect on molecular structure and material properties and the effect on fracture toughness. The effect on molecular structure was investigated with FTIR and XPS. Changes in mass, density, and k-value were correlated with changes in the molecular structure and a list of possible condensation reactions was given. The effect on fracture properties was an increase in critical fracture toughness with UV exposure; while, sub-critical fracture toughness was insensitive to UV cure.

In Chapter 7, the effect of UV curing on the material properties and molecular structure of a p-OSG film were discussed. The material properties were film shrinkage, densification, and the increase in dielectric constant. After 20 minutes of UV exposure, the film shrank by 17%; the film density increased by 10%; and the dielectric constant increased by 4%. These changes in film properties were attributed to changes in the molecular structure of the p-OSG film. From an XPS study of the fracture surfaces, it was found that the material lost carbon during the UV cure step. The total loss of carbon after a nine minute UV exposure was 38% or a loss in mass of 7%. Further changes in the molecular structure were measured by FTIR.

The change in dielectric constant was also discussed in Chapter 7. The contributions to the total dielectric constant from the electronic and ionic polarizabilities were measured separately. The electronic contribution was measured with an ellipsometer at a wavelength of 633 nm and was found to be roughly constant for all UV exposures. The ionic polarizability was measured by application of the Kramers-Kronig relations to the infrared absorption spectrum. The ionic content increased by 29% after 36 minutes of UV exposure. The sum of electronic and ionic components agreed well with the measured total dielectric constant at 1 MHz.

FTIR measurements were made in transmission mode. Changes in the cage, sub-oxide, network, hydrogen, and methyl units were measured by the spectral subtractive method. It was found that the methyl and cage structures decreased with all UV exposures. The methyl decrease agrees with XPS measurements. Also, the position of the methyl peak indicated that the connectivity of the p-OSG film was T or $SiO_{3/2}(CH_3)$. The network structures initially increased with UV curing, but decreased on long exposure. After an initial loss, the sub-oxide content increased with UV exposure. The sub-oxide formation includes Si-Si, Si-H, and Si-C bonds.

The measured changes in molecular structure and dielectric constant led to the proposal of four condensation reactions of the material with UV light. These reactions

$$\begin{aligned}
&\boldsymbol{i)} -Si-CH_3 + H-Si- + \gamma \rightarrow -Si-CH_2-Si- + H_2 \\
&\boldsymbol{ii)} -Si-CH_3 + CH_3-Si- + \gamma \rightarrow -Si-CH_2-Si- + CH_4 \\
&\boldsymbol{iii)} -Si-CH_3 + OH-Si- + \gamma \rightarrow -Si-O-Si- + CH_4 \\
&\boldsymbol{iv)} -Si-CH_3 + H-Si- + \gamma \rightarrow -Si-Si- + CH_4
\end{aligned} \tag{9.1}$$

produce methane and hydrogen and increase the number of ionic bonds. The reactions in Eq. 9.1 also increase the density and the number of bridging bonds in the film. The increase in bridging bonds should toughen the material against fracture.

Chapter 8 discussed the critical and sub-critical fracture toughness of UV cured p-OSG films. Critical fracture studies were performed for multiple mode-mixes—zero, 15°, 32°, and 42°. The Mode I fracture toughness increased linearly with UV exposure time. The mixed mode fracture toughness also increased linearly, below 2 J/m^2. Above 2 J/m^2, the fracture toughness increased monotonically with mode-mix, indicating an inelastic effect. The inelastic effect was attributed to asperity after determining that plastic contributions were negligible. All critical fractures were cohesive.

Sub-critical fracture was measured in Mode I for multiple relative humidities. A benchmark test was made at a constant relative humidity of 46%; while, sub-critical fracture studies were also made at average humidities of 15% and 87%. In all cases, sub-critical fracture was insensitive to UV exposure. The sub-critical velocity curves showed that the slope and threshold values for each UV exposure were roughly constant. For the benchmark test at 46% RH, the velocity slopes and threshold values are almost identical. The surface bond density was calculated from the slope of the velocity-strain-energy release rate curves. The surface bond density was constant and the threshold toughness was found to be linearly related to the relative humidity.

A mechanism for sub-critical fracture was proposed in Chapter 8. The mechanism was described in terms of reaction kinetics and void nucleation and coalescence. It was assumed that the bridging bonds of the UV cured material were Si-O-Si and Si-CH$_2$-Si. The reaction paths with water are given in Eq. 9.2. Each reaction

$$\begin{aligned} &-\boldsymbol{Si-O-Si-}+\boldsymbol{H_2O}\rightarrow\boldsymbol{-Si-OH}\ +\ \boldsymbol{HO-Si-}\\ &-\boldsymbol{Si-CH_2-Si-}+\boldsymbol{H_2O}\rightarrow\boldsymbol{-Si-O-Si-}+\ \boldsymbol{CH_4}\end{aligned} \tag{9.2}$$

path was considered a first order reaction and given a different reaction rate. It was further assumed that the reaction rate of Si-O-Si to silanol was faster than the transition of Si-CH_2-Si to Si-O-Si. An arbitrary time τ was chosen to characterize the depletion of Si-O-Si bonds. Bonamy et al have shown that sub-critical fracture in silica grows by void nucleation and coalescence. The stresses ahead of the sub-critical crack are sufficient to cause strain induced reactions between silica and water. These micro-voids then grow sufficiently that they coalesce with the main crack. If this process can occur in silica, it may also occur in an OSG film. A simple relation was proposed between the depletion time, τ; the micro-void length *d*, and the crack velocity *v*.

$$\tau \leq \frac{d}{v} \tag{9.3}$$

As long as Eq. 9.3 holds, the effect of UV curing is not noticeable.

The difference in the results of this dissertation and those of Gage, et al [1] were outlined in the introductory chapter. Gage found that, in Mode I, the critical and sub-critical fracture was insensitive to UV; yet, four-point bend measurements increased with UV exposure. The simplest reason for the difference between the results of Gage et al and this dissertation may be the uniformity of cure. Gage et al reported a non-uniform cure, where as the results of the films used for this study had a uniform cure profile. Two techniques were used to measure the film uniformity. XPS depth profiling indicated a constant intensity for carbon and oxygen with sputtering time. Also, an ellipsometer measured the depth profile of the refractive index. A Cauchy model fit the data best, indicating that the refractive index was uniform throughout the film.

9.2 Future work

The single largest advancement of this work would be a sub-critical fracture theory of a heterogeneously bonded material. The sub-critical fracture theory presented in this dissertation was that of Cook and Liniger. And that theory was based on previous theories and data of Wiederhorn. It was particularly developed for homogeneously bonded silica glass. Quantum Chemistry (QC) calculations would be a positive step in that development. By using QC, the reaction rates of different bonds with water could be calculated. Michalske et al have predicted that stress-corrosion of silica with water is a three step process with a single water molecule and a single Si-O-Si bond [2]. With QC calculations, the stress-corrosion process could be investigated and Si-C bonds could be added to the study. It would be interesting to know if the reaction path for Si-CH_2-Si with water is correct.

A simple and probably naïve model of UV curing was presented in Chapter 3. A better comprehension of the UV cure mechanism may lead to a better bulb. It would be interesting to know how many steps occur in the UV cure process. The influence of temperature could be more precisely defined.

It would appear that, even with UV curing, the low-k in question would not be able to survive CMP. However, this is misleading. The author is unaware of any literature on the driving force's phase angle during CMP. Cracks parallel to the CMP plane are most likely close to Mode II; however, the phase angle of normal cracks is presently unknown. Finite Element Analysis could be applied to this problem and the phase angles obtained. With this information, the MMDCB could be used to measure the fracture toughness for the given phase angles.

The increase in Si-Si and Si-C bonds was inferred from the rise in the FTIR sub-oxide peak. A direct measurement was not possible; but, could be obtained by either nuclear magnetic resonance (NMR) or electron spin resonance (ESR). NMR is generally requires about one gram of material and is cost prohibitive. However, ESR may be more promising.

Recently, Lin *et al*. [3] have calculated the absorbance cross-sections for the components of an organosilicate glass. The OSG was prepared from octamethylcyclotetrasiloxane (OMCTS). It would be interesting to see if the absorption cross-sections are applicable to the DEMS films used in this dissertation.

The elephant in the room is an air-bridge structure. Air bridges replace the low-k material with air. It will require some support structure, but, if successful, detailed studies of low-k materials may be obsolete.

References

Chapter One

1.1 Havemann, R.H.; Hutchby, J.A. *In* Proceedings of the IEEE, May 2001, vol.89, no.5, pp. 586-601 : IEEE, Journal Paper.

1.2 www.itrs.net

1.3 Scherban, T.; Sun, B.; Blaine, J.; Block, C.; Jin, B.; and Andideh, E. *International Interconnect Technology Conference*, 2001. pg. 257.

1.4 Leduc, P.; Farjot, T.; Savoye, M.; Demas, A.; Maitrejean, S.; Passemard, G. *Microelectronic Engineering.* **83**. 2006. pg. 2072-2076.

1.5 Iacopi, F.; Degryse, D.; Vos, I.; Patz, M.; and Maex, K. *Materials Research Society Symposium Proceedings.* **795**. 2004.

1.6 Maitrejean, S.; Fusalba, F.; Patz, M.; Jousseaume, V.; Mourier, T. *International Interconnect Technology Conference,* 2002. pg. 206.

1.7 Mercado, L.; Goldberg, C.; Kuo, S.; Lee, T.; and Pozder, S. *Electronic Components and Technology Conference.* 2003. pg. 1784.

1.8 Wang, G.; Merrill, C.; Zhao, J.; Groothius, S.; and Ho, P. *IEEE Transactions on Device and Materials Reliability*, Dec. 2003, vol.3, no.4, pp. 119-28 : IEEE, Journal Paper.

1.9 Grill, A.; Patel, V.; Rodbell, K.P.; Huang, E.; Christiansen, S.; and Baklanov, M.R. *Materials Research Society Symposium-Proceedings.* **716**. 2002. pp. 569-574.

1.10 Dauskardt, R. *SRC Topical Research Conference.* 2002

1.11 Mehta, S; Dimitrakopoulos, C.; Augur, R.; Gambino, J.; Chou, A.; Hook, T.; Linder, B.; Tseng, W.; Bolam, R.; Harmon, D.; Massey, D.; and Gates, S. *Advanced Metallization Conference.* 2005. pg. 60.

1.12 Matsuura, M.; Goto, K.; Miura, N.; Hashii, S.; and Asai, K. *Materials Research Society Symposium.* **914**. 2006.

1.13 Goto, K.; Hashii, S.; Matsumoto, M.; Miura, N.; Furusawa, T.; Matsuura, M.; Ohsaki, A.; Ohara, N.; Tsuji, N.; and Mtsushita, K. *Advanced Metallization Conference.* 2005. pg. 30.

1.14 Nakao, S.; Ushio, J.; Ohno, T.; Hamada, T.; Kamigaki, Y.; Kato, M.; Yoneda, K.; Kondo, S.; and Kobayashi, N. *Proceedings of the IEEE 2006 International Interconnect Technology Conference*. 2006. pg. 66.

1.15 Jacques, J.; Tsui, T.; McKerrow, A.; and Kraft, R. *Materials Research Society Symposium Proceedings*. **914**. 2006

1.16 Jacques, J.; Tsui, T.; McKerrow, A.; and Kraft, R. *Materials Research Society Symposium Proceedings*. **863**. 2005

1.17 Iacopi, F.; Waldfried, C.; Abell, T.; Travaly, Y.; Guyer, E.P.; Gage, D.M.; Eyckens, B.; Sajavaara, T.; Houthoofd, K.; Grobet, P.; Jacobs, P.; Maex, K.; and Dauskardt, R.H. *Journal of Applied Physics*. **99**: iss. 5. 2006. pg. 053511.

1.18 Gage, D.M.; Guyer, E.P.; Stebbins, J.F.; Cui, Z.; Al-Bayati, A.; Demos, A.; MacWilliams, K.; and Dauskardt, R.H. *Proceedings of the IEEE 2006 International Interconnect Technology Conference*. 2006. pg. 149,

Chapter 2

2.1 Halliday, D. and Resnick, R. **Physics.** John Wiley and Sons. 1978.

2.2 Kittel, C. **Introduction to Solid State Physics.** John Wiley and Sons. 1968.

2.3 Maex, K.; Baklanov, M.R.; Shamiryan, D., Iacopi, F.; Brongersma, S.H.; and Yanovitskaya, Z.S. *Journal of Applied Physics*. **93**, no. 11. 2003. pp: 8793-8841.

2.4 **Handbook of Chemistry and Physics.** 74th Ed. Lide, D.R. Ed. CRC Press. 1993

2.5 Pauling, L. **General Chemistry.** Dover Publications. 1970.

2.6 Kim, Y.; Hwang, M.S.; and Kim, H.J. *Journal of Applied Physics*. **90**, no. 7. 2001. pp: 3367-3370.

2.7 Grill, A. *Journal of Applied Physics*. **93**, no. 3. 2003. pg. 1785.

2.8 Guyer, E.P. and Dauskardt, R.H. *Proceedings of the IEEE 2005 International Interconnect Technology Conference*. 2005. pg. 223

2.9 Grill, A. and Neumayer, D.A. *Journal of Applied Physics*. **94**, no. 10. 2003. pg. 6697.

2.10 Liu, W.; Yang, C.; Chen, W.; Dai, B.; and Tsai, M. *Journal of Non-Crystalline Solids.* **311**. 2002. pp:233-240.

2.11 Jain, S.; Zubkov, V.; Nowak, T.; Demos, A.; and Rocha, J. *Solid State Technology.* Sept. 2005. pg 43.

Chapter 3

3.1 Jackson, J.D. **Classical Electrodynamics.** John Wiley and Sons. 1975

3.2 Baym, G. **Lectures on Quantum Mechanics.** W. J. Benjamin, Inc. 1974.

3.3 Craig, D.P. and Thirunamachandran, T. **Molecular Quantum Electrodynamics.** Dover Publications, Inc. 1984

3.4 Landau, L.D. and Lifshitz, E.M. **Quantum Mechanics (Non-relativistic Theory).** Pergamon Press. 1977.

3.5 Gottfried, K. **Quantum Mechanics.** Vol. 1. Addison-Wesley Publishing. 1989.

3.6 Harrison, W.A. **Elementary Electronic Structure.** World Scientific Publishing. 2004.

3.7 Berry, I.L.; Waldfried, C.; and Durr, K. *Materials Research Society Symposium.* **990**. 2007.

3.8 Iacopi, F.; Waldfried, C.; Abell, T.; Travaly, Y.; Guyer, E.P.; Gage, D.M.; Eyckens, B.; Sajavaara, T.; Houthoofd, K.; Grobet, P.; Jacobs, P.; Maex, K.; and Dauskardt, R.H. *Journal of Applied Physics.* **99**: iss. 5. 2006. pg. 053511.

Chapter 4

4.1 Dundurs, J. *Journal of Applied Mechanics*. **36**. 1969. pg. 650-652.

4.2 Griffith, A. A. *Philosophical Transactions of the Royal Society.* **A221**. 1921. pg 163-198.

4.3 Kanninen, M. and Popelar, C. **Advanced Fracture Mechanics**. Oxford University Press. 1985.

4.4 Hutchinson, J. W. and Suo, Z. *Advances in Applied Mechanics*. **29**. 1992. pg. 63-191.

4.5 Lane, M. *Annual Review of Materials Research.* **33**. 2003. pg. 29-54.

4.6 Rice, J.R. *Journal of Applied Mechanics.* **35**. 1968. pp: 379-386.

4.7 Rice, J.R. *Journal of Applied Mechanics.* **55**. 1988. pg. 98.

4.8 Smelser, R.E. and Gurtin, M.E. *International Journal of Fracture.* **13**. 1977. pg. 382.

4.9 Fleck, N.A.; Hutchinson, J.W.; and Suo, Z. *International Journal of Solids and Structures.* **27,** no. 13. 1991. pg 1683.

4.10 Hutchinson, J.W.; Mear M.E.; and Rice, J.R. *Journal of Applied Mechanics.* **54**, n 4. 1987. pp: 828-832.

4.11 Venkatraman, B.and Patel, S.A.. **Structural mechanics with introductions to elasticity and plasticity**. New York, McGraw-Hill 1970.

4.12 Evans, A.G. and Hutchinson, J.W. *Acta Metallurgica*. **37**, n 3. 1989, pp: 909-916.

4.13 Cook, R.E. and Liniger, E.G. *Journal of the American Ceramic Society.* **76**, no. 5. 1993. pp:1096-1105.

4.14 Broek D. **Elementary Engineering Fracture Mechanics.** Kluwer Academic Publishers. 1986.

4.15 Gould, P. **Introduction to Linear Elasticity.** Springer-Verlag New York, Inc. 1994.

4.16 Timoshenko, S.P. and Goodier, J.N. **Theory of Elasticity.** McGraw-Hill International Editions. 1970.

4.17 Williams, M. L. *Journal of Applied Mechanics.* **19.** 1952. pg. 526.

Chapter 5

5.1 Goh, T.K. and Wong, T.K.S. *Microelectronic Engineering.* **75**. 2004. pp: 330-343.

5.2 Parratt, L.G. *Physical Review.* **95**, no. 2. 1954. pg. 359.

5.3 www.chem.qmul.ac.uk/surfaces/scc/scat5_3.htm

5.4 Marder, M.P. **Condensed Matter Physics.** John Wiley and Sons. 2000.

5.5 www.nist.gov

5.6 Gunzler, H. and Gremlich, H. **IR Spectroscopy: An Introduction.** Wiley-VCH. 2002.

5.7 Grill, A. and Patel, V. *Journal of the Electrochemical Society.* **153**, no 8. 2006. pp:F169-F175.

5.8 Grill, A. and Neumayer, D.A. *Journal of Applied Physics.* **94**, no. 10. 2003. pg. 6697.

5.9 Kim, Y.; Hwang, M.S.; and Kim, H.J. *Journal of Applied Physics.* **90**, no. 7. 2001. pp: 3367-3370.

5.10 Ross, A. and Gleason, K. *Journal of Applied Physics.* **97**. 2005. pg. 113707.

5.11 Lim, S.W.; Shimogaki, Y.; Nakano, Y.; Tada, K.; Komiyama, H. *Journal of the Electrochemical Society.* **144**, no. 7. 1997. pp: 2531-2537.

5.12 Han, S.M. and Aydil, E.S. *Journal of Applied Physics.* **83**, no. 4. 1998. pp: 2172-2178.

5.13 Jackson, J.D. **Classical Electrodynamics.** John Wiley and Sons. 1975

5.14 Socrates, G. **Infrared Characteristic Group Frequencies.** John Wiley and Sons Publishing. 1998.

Chapter 6

6.1 Charalambides, P.G.; Cao, H.C.; Lund, J; and Evans, A.G. *Mechanics of Materials*. **8**. 1990. pp:269-283.

6.2 Fernlund, G. and Spelt, J.K. *Composites Science and Technology.* **50.** 1994. pp:441-449.

Chapter 7

7.1 Kim, H.J.; Shao, Q.; and Kim, Y. *Surface and Coatings Technology.* **171** 2003. pp:39-45.

7.2 Maex, K.; Baklanov, M.R.; Shamiryan, D., Iacopi, F.; Brongersma, S.H.; and Yanovitskaya, Z.S. *Journal of Applied Physics*. **93**, no. 11. 2003. pp: 8793-8841.

7.3 Jain, S.; Zubkov, V.; Nowak, T.; Demos, A.; and Rocha, J. *Solid State Technology.* Sept. 2005. pg 43.

7.4 Grill, A. and Neumayer, D.A. *Journal of Applied Physics.* **94**, no. 10. 2003. pg. 6697.

7.5 **Handbook of Chemistry and Physics.** 74th Ed. Lide, D.R. Ed. CRC Press. 1993

7.6 Matsuura, M.; Goto, K.; Miura, N.; Hashii, S.; and Asai, K. *Materials Research Society Symposium.* **914**. 2006.

7.7 Iacopi, F.; Waldfried, C.; Abell, T.; Travaly, Y.; Guyer, E.P.; Gage, D.M.; Eyckens, B.; Sajavaara, T.; Houthoofd, K.; Grobet, P.; Jacobs, P.; Maex, K.; and Dauskardt, R.H. *Journal of Applied Physics.* **99**: iss. 5. 2006. pg. 053511.

7.8 Berry, I.L.; Waldfried, C.; and Durr, K. *Materials Research Society Symposium.* **990**. 2007.

Chapter 8

8.1 Bonamy, D.; Prades, S.; Rountree, C.L.; Ponson, L.; Dalmas, D.; Bouchaud, E.; Ravi-Chandar, K.; and Guillot, C. *International Journal of Fracture.* **140.** 2006. pp:3-14.

8.2 Evans A.G., Hutchinson J.W., *Acta Metallurgica*. **37.** 1989. pp**:** 909-916.

8.3 Cook R.F., Liniger E.G., *J. Am. Ceram. Soc.* **76**. 1993. pp**:** 1096-2105.

8.4 Michalske T.A., Bunker B.C. *J. Appl. Phys.* 1984. **56:** 2686-2693.

8.5 Vlassak J.J., Lin Y., Tsui T.Y., *Mater. Sci. Eng. A.* 2004. **391:** 159-174.

8.6 Lane M. *Annu. Rev. Mater. Res.* **33.** 2003. pp**:** 29-54.

8.7 Lane M., Dauskardt R., Ma Q., Fujimoto H., Krishna N. *Mater. Res. Soc. Symp.* 1999. **563:** 251-256.

8.8 McHenry, K.D. and Tressler, R.E. *Journal of Materials Scence.* **12**. 1977. pp: 1272-1278.

8.9 Singhal, S.C. in “*Ceramics for High Performance Applications*”**.** Ed. Burke, J.J.; Gorum, A.E.; and Katz, R.N. *Proceedings of the 2nd Army Materials Technology Conference.* 1973. pg. 533.

8.10 Laidler, K.J. **Chemical Kinetics**. McGraw-Hill Book Company, Inc. 1950.

8.11 Rountree, C.L.; Kalia, R.K.; Lidorikis, E.; Nakano, A.; Van Brutzel, L; and Vashishta, P. *Annual Review of Materials Research.* **32**. 2002. pp:377-400.

8.12 Hutchinson, J.W.; Mear M.E.; and Rice, J.R. *Journal of Applied Mechanics.* **54**, n 4. 1987. pp: 828-832.

Chapter 9

9.1 Gage, D.M.; Guyer, E.P.; Stebbins, J.F.; Cui, Z.; Al-Bayati, A.; Demos, A.; MacWilliams, K.; and Dauskardt, R.H. *Proceedings of the IEEE 2006 International Interconnect Technology Conference*. 2006. pg. 149.

9.2 Michalske, T.A. and Bunker, C. *Journal of Applied Physics.* **56**, no. 10. 1984. pg. 2686.

9.3 Lin, Y.; Tsui, T; and Vlassak, J.J. *Journal of the Electrochemical Society.* **153**, no. 7. 2006. pp:F144-F152.

Vita

Ryan Scott Smith was adopted in Febuary, 1970 by Robert and Pamela Smith. He lived in Burleson, Texas, until his graduation from high school. In 1988, he enrolled at The University of North Texas, earning a bachelors of arts in physics. He moved from Texas in 1993 to attend graduate studies in physics at Cornell University. He left Cornell after 4 years with a Masters in Science. For his Masters Thesis, he measured the "coherent beam-beam effect" in the Cornell Electron Storage Ring (CESR). After leaving Cornell, he returned to Texas and began an internship with DSPS Packaging at Texas Instruments that lasted one year. At Texas Instruments, he was introduced to Prof. Paul Ho at The University of Texas at Austin. Shortly afterwards, he joined Prof. Ho's group at UT and started his Ph.D. He graduated from UT in August of 2007.

Permanent Address: P.O. Box 353, Millsap, TX 76066

This dissertation was typed by the author.